

Faculty of Physics
LUDWIG-MAXIMILIANS-UNIVERSITÄT MÜNCHEN

MASTER'S THESIS

Optoelectronic Studies of Molybdenum Disulfide Field-Effect Devices

Manuel Nutz

November 17, 2014



Chair of Solid State Physics
Prof. Jörg P. Kotthaus

Nano-Photonics Group
Prof. Alexander Högele

Fakultät für Physik
LUDWIG-MAXIMILIANS-UNIVERSITÄT MÜNCHEN

MASTERARBEIT

Optoelektronische Untersuchung von Molybdändisulfid-Feldeffektstrukturen

Manuel Nutz

17. November 2014



Lehrstuhl für Festkörperphysik
Prof. Jörg P. Kotthaus

Gruppe Nanophotonik
Prof. Alexander Högele

Contents

1. Introduction	7
2. Physical properties of monolayer molybdenum disulfide	9
2.1. Atomic structure	9
2.2. Band structure	10
2.3. Coupled spin and valley physics	12
3. Experimental methods and results	15
3.1. Cryogenic confocal microscopy	15
3.1.1. Principles of cryogenic confocal microscopy	15
3.1.2. Photoluminescence measurements with monolayer molybdenum disulfide	18
3.2. Field effect nanostructures with monolayer molybdenum disulfide	21
3.2.1. Charge carrier density tuning with an electric field	21
3.2.2. Device fabrication by laser lithography	22
3.2.3. Electric contacting of the sample	31
3.2.4. Sample characterization by electrical transport measurements	34
3.3. Experimental results	40
4. Summary and outlook	43
A. Suggested modifications for future samples	47
A.1. Photoresist and lift-off resist	47
A.2. Thermal annealing	49
A.3. Sample mounting	49
B. Theoretical description of solid immersion lenses	51
B.1. Dipole fields at planar phase boundaries	51
B.1.1. Expansion of the dipole field in plane waves	52
B.1.2. Orthogonal decomposition of plane wave components	54
B.1.3. Reflection and transmission of plane waves	55
B.1.4. Approximation for a distant observation point	58
B.1.5. Method of steepest descents	61
B.2. Numerical calculation of transmission and reflection coefficients	66
B.3. Dipole radiating with a fixed power	68
B.4. Application to a three-phase system	70

List of Abbreviations	75
------------------------------	-----------

References	77
-------------------	-----------

Chapter 1.

Introduction

Since the first successful isolation of graphene by micromechanical cleavage in 2004 [46] a vast and vivid research area has developed around atomically thin two-dimensional materials. While in early years the physical properties of graphene were explored, the focus of research has gradually shifted toward possible applications of this unique material [45].

Graphene features several remarkable properties which make it an interesting material for various technical applications, e.g. its large Young's modulus, its extraordinary surface-to-volume ratio [73] and in particular its exceptionally high carrier mobility of more than $10^6 \text{ cm}^2/(\text{Vs})$ [12]. This latter property has for example been exploited to build high-frequency transistors with cutoff frequencies of several hundred gigahertz [33, 68, 69].

Yet, from the perspective of microelectronics, graphene suffers from one major drawback, namely the lack of a band gap. This causes poor on/off switching ratios for graphene based field-effect transistor (FET) structures [66, 73], making their practical use challenging. Nonetheless, current silicon-based metal-oxide-semiconductor field-effect transistor (MOS-FET) electronics will soon reach physical limits preventing further miniaturization and thereby reduction of both switching time and energy consumption [66].

In the light of the above, novel layered materials have recently attained increasing attention. Although material properties have to meet several requirements for an atomic monolayer to be isolated and to not degenerate rapidly, more than a dozen two-dimensional crystals are currently known to be stable at ambient conditions [14]. In particular, several semiconducting monolayer materials open the perspective of combining potential benefits of graphene while bypassing some of the aforementioned obstacles.

One widely studied group of semiconducting monolayers are the transition metal dichalcogenides (TMDCs). The most common representatives MoS_2 , WS_2 , MoSe_2 and WSe_2 have been used as dry lubricants for a long time, what already indicates to the durability of these materials without which the isolation of single atomic sheets would be impossible [14]. Especially, monolayers of molybdenum disulfide (MoS_2) have received lots of attention, since they show a variety of interesting physical properties.

To begin with, the direct band gap of 1.85 eV [66, 78] make this material interesting for both electronic and optoelectronic devices. Furthermore, the response of MoS₂ to illumination strongly depends on the polarization of the incident light [8, 38, 55, 77]. In addition, both width and type of the band gap have been shown to change when applying tensile strain [11, 20, 78] giving rise to potential sensoring applications. Recently, even a superconducting phase has been reported to exist in MoS₂ [63, 75].

Another promising perspective for future applications are monolayer heterostructures. Since layered materials all share the common feature that the individual atomic sheets are held together by van der Waals forces, the possibility arises to stack monolayers of *different* materials on top of each other. Hence, tailored heterostructures of two-dimensional crystals can be created in an arbitrary sequence [14].

Using this technique not only transistor-like structures using monolayer MoS₂ [49], but also heterostructures aiming to combine the advantages of the highly conductive graphene and the semiconducting TMDCs in the form of field-effect tunneling transistors (FETTs) [7, 15] have been reported. Compared to similar transistors made from graphene only [70], these devices show by three orders of magnitude better on/off switching ratios.

The great variety of possible applications sketched so far explains the huge interest in TMDCs and in MoS₂ in particular. In order to investigate the electronic properties of MoS₂ and its band structure in more detail, a combination of electrical and optical methods has been applied within this work. Sample preparation techniques were developed, which enable the manipulation of the Fermi level in a MoS₂ monolayer using a FET like structure while spectrally analyzing the photoluminescence (PL) response at cryogenic temperatures.

This thesis begins with a revision of the physical properties of monolayer MoS₂ in chapter 2. Afterward experimental methods and results are explained in detail in chapter 3. In particular the optical setup and the sample preparation procedure are presented in sections 3.1 and 3.2 and complemented by experimental results in section 3.3. A summary of the obtained results and an outlook to future experiments is given in chapter 4. The appendix begins with a brief collection of suggested modifications for future samples in appendix A. Finally, appendix B presents an overview over possible applications of solid immersion lenses (SILs) for optical experiments presented in this work and beyond, including a theoretical description and simulated radiation profiles.

Chapter 2.

Physical properties of monolayer molybdenum disulfide

2.1. Atomic structure

The physical properties of bulk MoS₂ and graphite are alike in several ways, for example regarding their optical appearance or their use as dry lubricants. Several of these similarities can be explained by their common microscopic structure: Both materials consist of sheets of atomic monolayers, which are stacked on top of each other. While the covalent atomic bonds within each layer are comparatively stable, the individual layers are held together by much weaker van der Waals forces and can be separated relatively easily.

While each atomic monolayer of graphite – better known as *graphene* [46] – is a simple hexagonal grid of carbon atoms, the atomic structure of MoS₂ and other TMDCs is slightly

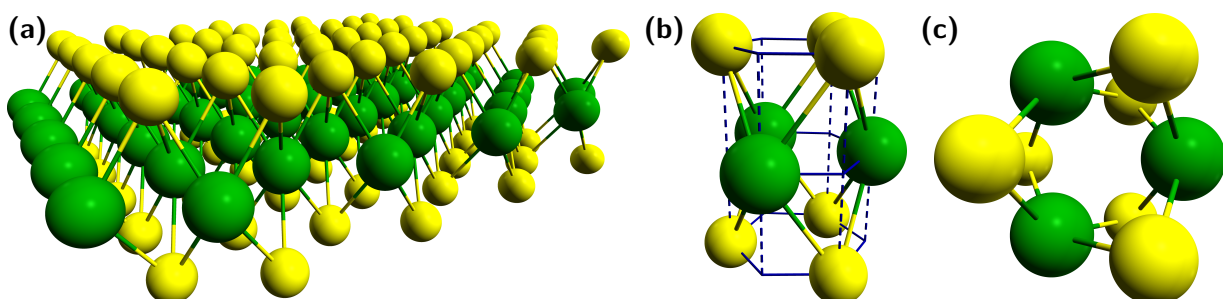


Figure 2.1.: Schematic drawing of the atomic structure of monolayer MoS₂ created with Avogadro [18]. **(a)** Single MoS₂ sheet consisting of one layer of molybdenum atoms (green) between two layers of sulfur atoms (yellow), each featuring a hexagonal structure. **(b)** Unit cell with three molybdenum and six sulfur atoms. Both the molybdenum and the sulfur atoms occupy every other site in three respective honeycomb lattices, which are stacked on top of each other in a hcp structure. **(c)** Top view of the same structure with three molybdenum and six sulfur atoms.

more complex. Fig. 2.1 (a) shows a schematic drawing of a single MoS₂ sheet, which consists of one layer of molybdenum atoms (green) between two layers of sulfur atoms (yellow) [14].

A detailed view of the unit cell with only three molybdenum and six sulfur atoms in fig. 2.1 (b) reveals this structure in more detail. Both the molybdenum and the sulfur atoms occupy each other site in three respective honeycomb lattices, which are stacked on top of each other in a hexagonal close-packed (hcp) structure. The same detail as viewed from top is shown in fig. 2.1 (c).

In particular, figs. 2.1 (b) and 2.1 (c) demonstrate that monolayer MoS₂ crystals show rotational but no inversion symmetry: When the unit cell of a MoS₂ monolayer is point reflected at its center, both molybdenum and sulfur atoms are mapped to empty lattice sites, i. e. the atom positions do not remain unchanged upon spatial inversion. This has important consequences for the spin-valley physics discussed in section 2.3.

The MoS₂ flakes used throughout this work were grown by chemical vapor deposition (CVD) [42] and provided by Hisato Yamaguchi from LANL. Sample images can be found in chapter 3. While fig. 3.6 shows the appearance under a light microscope, atomic force microscope (AFM) measurements are presented in fig. 3.12.

2.2. Band structure

The electronic properties of MoS₂ have been thoroughly investigated [66]. Although its atomic structure is similar to that of graphene, several major differences exist in terms of the band structure that are of particular importance for any optical experiments.

The most prominent features of the well-known graphene band structure are the K-points in its hexagonal Brillouin zone, usually named *Dirac points* [9]. At these points valence band and conduction band touch each other, so that graphene shows no band gap. The exceptional linear dispersion relation in the vicinity of these points causes the charge carriers to behave like massless Dirac fermions [9, 39].

By contrast, MoS₂ is a semiconducting material, possessing a typical band gap with quadratic dispersion relation. For the optical experiments discussed in this work, the nature of this band gap is of particular importance. Fig. 2.2 reproduces theoretical simulations of the MoS₂ band structure reported in [76] using the full-potential linearized augmented plane wave (FLAPW) method.

While the band gap of bulk MoS₂ is indirect (cf. fig. 2.2 (a)) with a calculated (measured) width of 0.9 eV [76] (1.2 eV [66]), it becomes a direct band gap at the K-point with a calculated (measured) width of 1.7 eV [76] (1.85 eV [66, 78]), when a MoS₂ crystal is thinned down to a monolayer (cf. fig. 2.2 (c)). Interestingly, fig. 2.2 (b) shows that the band gap is still indirect for bilayers. This effect explains the counter-intuitive observation that PL from MoS₂ monolayers is brighter than for any other number of layers [60].

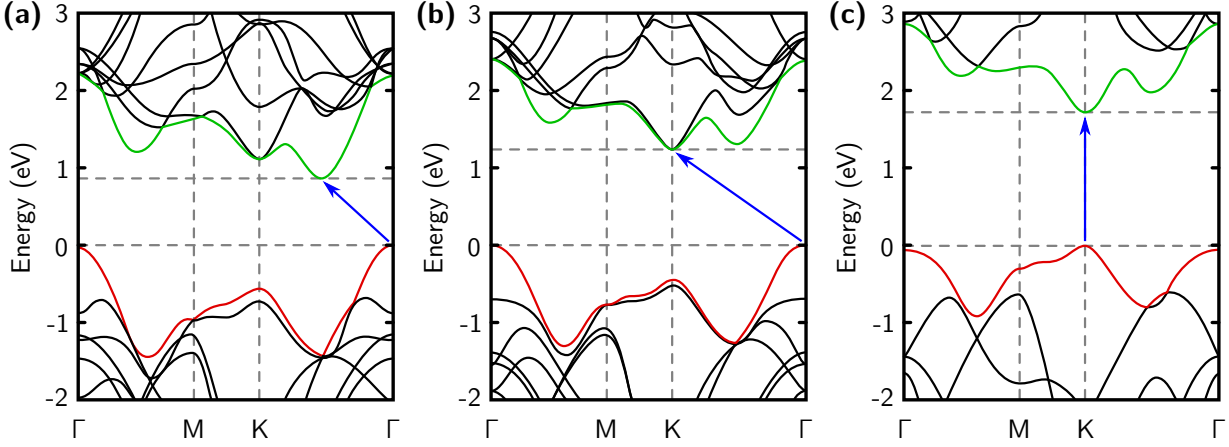


Figure 2.2.: Reproduced theoretical simulations of the MoS₂ band structure using the full-potential linearized augmented plane wave (FLAPW) method [76]. The highest energy state in the valence band is indicated in red, while the lowest energy state in the conduction band is marked green. The blue arrow indicates the transition from the valence band to the conduction band which requires the least energy. **(a)** Bulk MoS₂ with an indirect band gap and calculated (measured) width of 0.9 eV [76] (1.2 eV [66]). **(b)** MoS₂ bilayer with an indirect band gap and calculated (measured) width of 1.3 eV [76] (1.83 eV [78]). **(c)** MoS₂ monolayer with a direct band gap and calculated (measured) width of 1.7 eV [76] (1.85 eV [66, 78]).

The experimental band gap energies given here are valid for room temperature. To obtain the band gap of monolayer MoS₂ at cryogenic temperatures, the phenomenological temperature dependence

$$E_g(T) = E_g(0\text{ K}) - \frac{\alpha T^2}{T + \beta}$$

given by the Varshni equation [65] with the experimental values $\alpha = 5.9 \times 10^{-4} \text{ eV/K}$ and $\beta = 430 \text{ K}$ [31] can be used. The resulting band gap $E_g(4 \text{ K}) = 1.92 \text{ eV}$ differs by 70 meV from the room-temperature value.

The change in the band structure for different layer number can be explained by the properties of the atomic orbitals constituting valence and conduction band [66]. Using density functional theory (DFT) calculations it has been shown that in bulk MoS₂ the conduction-band states at the K-point are derived from localized d-orbitals of the Mo atoms, while the states at the Γ -point and the point of the indirect band gap originate from a linear combination of d-orbitals of the Mo atoms and antibonding p_z-orbitals of the S atoms [60].

The K-point orbitals are located in the middle of a single S-Mo-S sheet and are thus hardly affected by a reduction of the layer number. This implies that the width of the band gap at the K-point is almost independent of the number of layers [60, 66], which is qualitatively verified by inspection of fig. 2.2. By contrast, the Γ -point orbitals show a strong interlayer coupling causing a pronounced shift of the band gap at the Γ -point and the point of the

indirect band gap when the layer number is reduced. Both effects combined are responsible for the transition from an indirect to a direct band gap upon thinning down a MoS₂ crystal to a monolayer [60, 66].

2.3. Coupled spin and valley physics

In order to understand the MoS₂ band structure in the vicinity of the band gap at the K-point in full detail, a more thorough analysis is necessary. Due to the sixfold crystal symmetry of MoS₂ the corresponding Brillouin zone is hexagonal and has in total six K-points that are energetically degenerate. However, in a reduced zone scheme only two of them are inequivalent. These two K-points labeled as +K and -K turn out to show different physical properties and are frequently also termed as *valleys*.

Although these K-points are also present in the band structure of graphene [9, 39], their physical properties are identical. This indistinguishability is lifted in the case of monolayer MoS₂, where a pronounced phenomenological difference exists for two main reasons. First, unlike for graphene, spatial inversion symmetry is explicitly broken in monolayer MoS₂ (cf. section 2.1). Second, a strong spin-orbit coupling (SOC) originating from the d-orbitals of Mo is present in MoS₂ [71].

A schematic drawing of the band structure in the vicinity of the K-points based on [71] is shown in fig. 2.3. The combination of broken inversion symmetry and SOC leads to a splitting of the highest energy state in the valence band by about 160 meV [38]. Time reversal symmetry dictates that this splitting is opposite for the two K-points [71]: The spin-up and the spin-down state have higher energy at the +K and the -K-point, respectively.

Since the energy separation in the valence band of 160 meV is larger than thermal energy at room temperature ($k_B T = 26$ meV for $T = 300$ K), it can be assumed that a transition between the two valence subbands is suppressed if no coupling to the environment e. g. by emission or absorption of a photon is present. This implies that for a hole in either of the two valleys, spin is conserved, which is further supported by the observation that the spin quantum number s_z is a good quantum number of the corresponding Hamiltonian [71]. Spin and valley physics are therefore inherently coupled in monolayer MoS₂ [38] and the different physical properties of the two K-points give rise to what is usually called *valleytronics* [53, 72, 74], i. e. manipulation of the valley degree of freedom.

In particular, for a transition from one of the valleys to the other within the same subband, a spin flip is required, e. g. by coupling to a magnetic defect. Since the two valleys are separated by a wave vector comparable to the size of the Brillouin zone, scattering with a phonon of large momentum is necessary at the same time. This restriction suggests a relatively long spin-valley lifetime [71], which was verified experimentally in [38], where a valley lifetime above 1 ns was reported for monolayer MoS₂ at 14 K. In bilayer MoS₂, by contrast, inversion symmetry is restored, so that spin and valley physics are decoupled. Accordingly, a much shorter valley lifetime of only few hundred femtoseconds was observed.

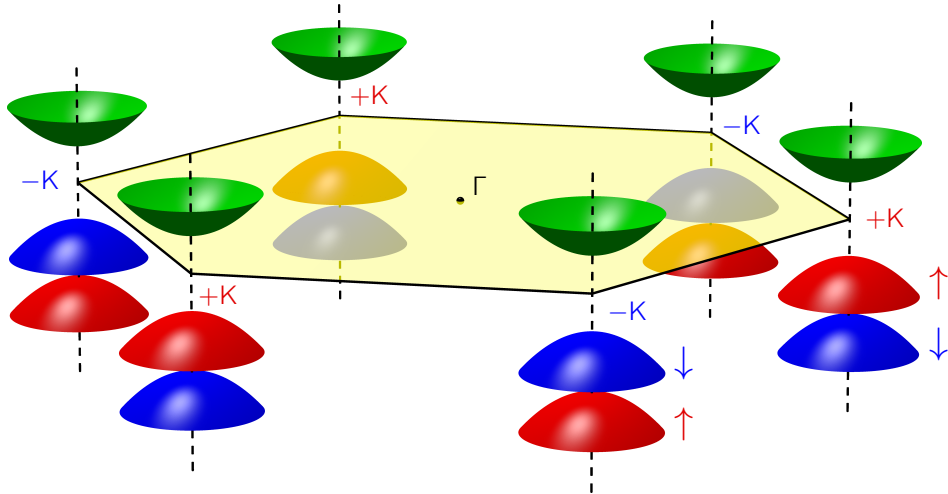


Figure 2.3.: Schematic drawing of the Brillouin zone of monolayer MoS₂ based on [71]. In the vicinity of the band edges located at the K-points both valence and conduction band show a quadratic dispersion relation. The combination of broken inversion symmetry in monolayer MoS₂ and SOC leads to a splitting of the highest energy state in the valence band by about 160 meV: The spin-up and the spin-down state have higher energy at the +K and the -K-point, respectively.

A very convenient way of exploiting both spin-valley coupling and the relatively long spin-valley lifetime in monolayer MoS₂ for the purpose of valleytronics is by means of polarization-resolved photonics. This method makes use of the valley-selective circular dichroism, which is addressed in the following.

At the K-points the conduction band is twofold spin degenerate with total angular momenta m_j of +3/2 and +1/2 at the +K-point as well as -3/2 and -1/2 at the -K-point [38]. Similarly, in the two valence subbands only the total angular momenta m_j of +1/2 and -1/2 are possible, but their order depends on the valley as illustrated in fig. 2.4.

Since for optical dipole transitions the total angular momentum can only change by ± 1 , at the +K-point no other transitions but between the higher-energy valence subband with $m_j = +1/2$ and the conduction band state with $m_j = +3/2$ as well as between the lower-energy valence subband with $m_j = -1/2$ and the conduction band state with $m_j = +1/2$ are possible. In either case the change in total angular momentum is equal to +1. To the -K-point according rules with reversed sign apply. Hence, the only dipole-allowed transitions are absorption/emission of a σ^+ (σ^-) polarized photon for the +K-point (-K-point) as shown in fig. 2.4.

Calculations from [8] show that these selection rules are robust against slight deviations from the K-points. This implies that optical excitation of monolayer MoS₂ with circularly polarized light with photon energy at or slightly above the band gap will selectively populate one of the two valleys with electron-hole pairs. This holds true both for the A exciton (corresponding to the transition from the higher energy valence subband to the conduction band) and the B exciton (corresponding to the transition from the lower energy valence

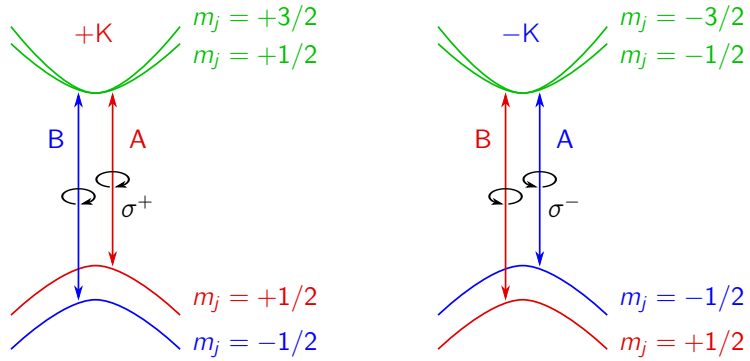


Figure 2.4.: Dipole selection rules for monolayer MoS₂. At both K-points the possible total angular momentum quantum numbers are determined by a combination of broken inversion symmetry and SOC. The only dipole-allowed transitions are absorption/emission of a σ^+ (σ^-) polarized photon for the +K-point (-K-point).

subband to the conduction band). In general, the different response to left and right handed circularly polarized light is called *circular dichroism*. For the special case discussed here, the term *valley-selective circular dichroism* is commonly used in literature.

Since exciton lifetimes are much shorter than valley lifetimes in monolayer MoS₂ [38], electron-hole pairs can be assumed to remain in the vicinity of the same K-point until they recombine. Hence, photons emitted due to radiative recombination of excitonic states preserve the circular polarization state of the excitation. For off-resonant excitation or MoS₂ bilayers, however, no such PL polarization is expected. These predictions have been verified experimentally in [8, 38, 55, 77].

When linearly polarized light is used for excitation instead of circularly polarized light, it is further possible, to create coherent superpositions of excitons at the +K and the -K-point. These superpositions are then able to evolve in time coherently until they recombine and to emit PL with the same linear polarization state. This effect called *valley coherence* was shown for the TMDC WSe₂ [29] but to our best knowledge has not been reported for MoS₂ as of the time of writing.

Several of the literature results presented above have also been confirmed in the experiments conducted for this thesis. Our measurements are presented in the following chapter after a discussion of the experimental setup.

Chapter 3.

Experimental methods and results

For the experiments reported here, a combination of optical and electronic methods was employed. A detailed description of these two complementary approaches can be found in the following sections.

3.1. Cryogenic confocal microscopy

3.1.1. Principles of cryogenic confocal microscopy

According to the Abbe theory of microscopes [44, pp. 408–416] lateral and longitudinal resolution of conventional microscopy are limited by diffraction and capturing of light from out-of-focus planes by the objective [47, pp. 1–4]. While sub-diffraction microscopy is an involved technique [4, 22, 30, 41], the latter limitation can be overcome by the use of confocal microscopy.

Unlike for conventional microscopy where larger parts of the sample are illuminated, in confocal microscopy the illumination source passes a pinhole that is imaged by the condenser to a single spot on the sample. Also the back scattered light collected by the objective is focused through a pinhole before detection. This configuration makes sure that only light passing through the focal point can pass from the light source to the detector, thereby excluding any light from out-of-focus planes [47, pp. 4–5].

This approach has the advantage that the resolution of a confocal microscope is only diffraction limited by the image size of the pinhole on the sample. However, the only information obtained that way is the intensity of the light scattered from this illuminated spot. A microscope image thus has to be created indirectly by scanning this spot over the sample and combining the different intensity measurements.

When applying confocal microscopy to cryogenic experiments [25], it is convenient to operate in *epi-illuminating* mode [47, p. 5], in which the objective also serves as condenser,

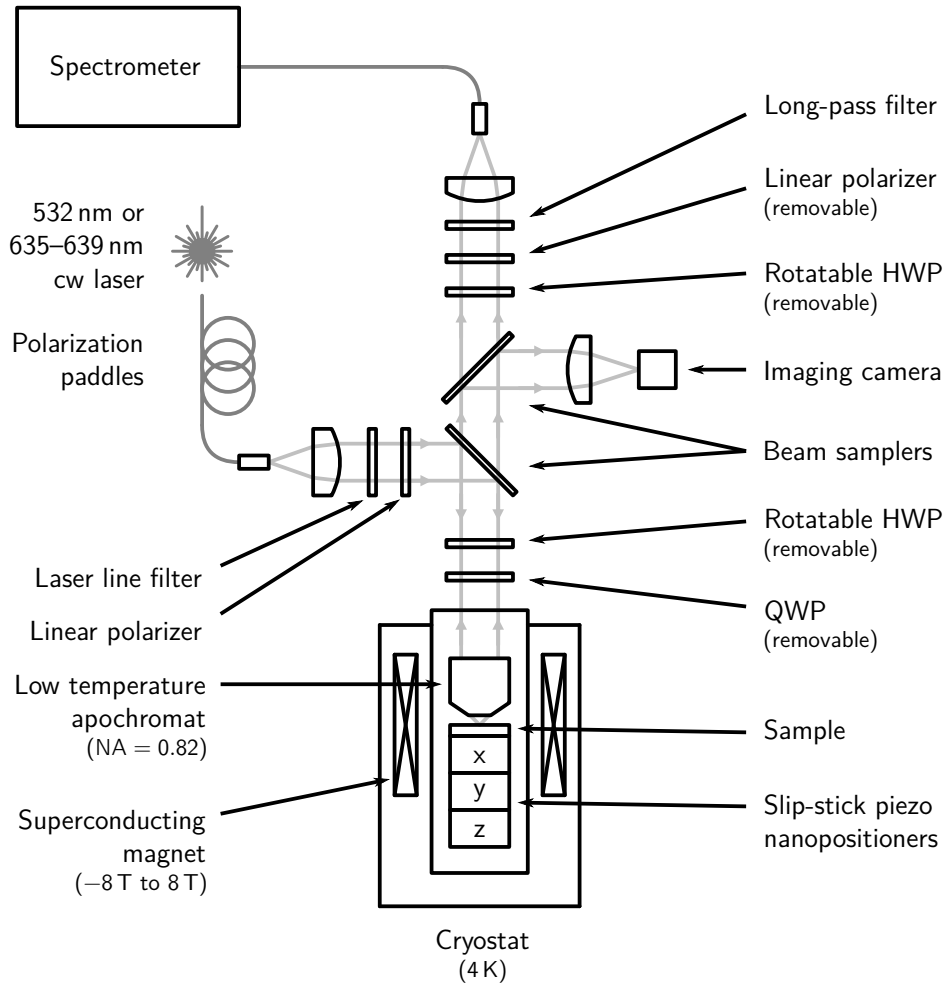


Figure 3.1.: Schematic drawing of the cryogenic confocal microscope. A 532 nm or a 635 nm to 639 nm tunable cw laser is coupled into the microscope through a single-mode fiber. After collimation it passes a laser line filter and a linear polarizer. The laser beam is deflected by a beam sampler and passes a HWP on a piezo rotator and a QWP on the way toward the objective. A home-built low temperature apochromat with a NA of 0.82 and a measured diffraction limited spot-size of 550 nm focuses the laser on the sample mounted on a stack of three slip-stick piezo nanopositioners. Sample and objective are cooled to 4 K by a liquid helium bath cryostat featuring a superconducting magnet, which provides fields of -8 T to 8 T . PL light is collected by the same objective and passes again through the QWP and the HWP as well as the lower beam sampler. The top beam sampler guides a small fraction of PL and reflected light to an imaging camera used for orientation on the sample. PL passing the top beam sampler goes through another HWP on a piezo rotator and a linear polarizer, which together can be used as a polarization analyzing unit. After blocking residual laser light by a long-pass filter a second collimator couples the PL signal into a single-mode fiber leading to a spectrometer with liquid-nitrogen cooled CCD.

so that optical path of illumination and detection are identical. This way only one optical access to the cryostat is needed. A schematic drawing of the home-built confocal microscope used for the experiments reported here is shown in fig. 3.1.

A 532 nm or a 635 nm to 639 nm tunable continuous wave (cw) laser for illumination is coupled into the microscope from the side arm through a single-mode fiber using polarization paddles for rough control over the input polarization. The core of the fiber serves as pinhole in the optical path of the illuminating light. Since the beam leaving the fiber is divergent, it is guided through a home-built apochromatic collimator with two lenses. Afterward it passes a suitable laser line filter to block fiber luminescence and a linear polarizer for more precise control of the polarization.

A polarization-dependent fraction of the beam is mirrored towards the objective by a broadband beam sampler, i. e. a slightly wedged fused silica plate with an anti-reflection coating on one side. The incident beam is Fresnel reflected off the uncoated side of the beam sampler – usually the surface, the beam passes first –, while the anti-reflection coated back surface suppresses ghosting, i. e. appearance of a second reflected beam. The Fresnel equations predict different reflection intensities for S and P-polarized light [79, pp. 33-42]. For an angle of incidence of $45^\circ \pm 3^\circ$ a fraction of $8.62^{+0.90}_{-0.85}\%$ is reflected for S-polarized light, while the corresponding value for P-polarized light is $0.80^{+0.37}_{-0.27}\%$ [43].

After reflection at the beam sampler the beam going towards the objective passes a removable half-wave plate (HWP) mounted on a piezo step rotator that allows for precise orientation and a removable quarter-wave plate (QWP), which can be used to transform the linear input polarization into an arbitrary polarization going to the sample. Through a vacuum window the beam enters the microscope tube, which is filled with helium exchange gas at 25 mbar pressure and resides in a cryostat cooled by liquid helium to about 4 K. A built-in superconducting magnet allows for application of magnetic fields of -8 T to 8 T .

The beam is focused to the sample by a home-built low temperature apochromat with a numerical aperture (NA) of 0.82 and a measured diffraction limited spot-size of 550 nm for visible light. To allow for sub-micrometer positioning in x -, y - and z -direction the sample is mounted onto a stack of three slip-stick piezo nanopositioners. Some of the measurements presented in this work were recorded using a very similar setup with a closed-cycle cryostat operating at 3 K and a low-temperature apochromat with NA 0.65.

PL light coming from the sample as well as reflected input laser light pass objective, QWP, HWP and the lower beam sampler in opposite direction. The second beam sampler guides a small fraction of this light to an imaging camera to simplify sample positioning. In order to facilitate polarization-resolved measurements, the two beam samplers were mounted in an arrangement which preserves the polarization state of the PL signal.

A second HWP mounted on a piezo step rotator and a linear polarizer in the top arm, which are both removable, can be used to analyze the PL polarization. Reflections of the illumination laser are blocked by an appropriate longpass filter, before the PL is coupled to a single-mode fiber through another collimator. The fiber core serves as the second pinhole in the confocal configuration and leads to a spectrometer with 0.5 m focal length and a

liquid nitrogen cooled charge-coupled device (CCD) detector for spectral analysis of the PL signal.

3.1.2. Photoluminescence measurements with monolayer molybdenum disulfide

With the setup sketched in section 3.1.1 several PL measurements with monolayer MoS₂ have been conducted. Fig. 3.2(a) presents the data of a typical PL spectrum recorded at 3 K with a 532 nm excitation laser of 2 mW input power in grey. The spectrum can be reproduced to great accuracy by fitting the sum of three Lorentz curves as shown in red.

The two main features of this spectrum are given by the maxima with center wavelengths (667.09 ± 0.03) nm ((1.8586 ± 0.0001) eV) and (610.2 ± 0.3) nm ((2.032 ± 0.001) eV) as determined by the Lorentz fits, which correspond to the A and B exciton, respectively. In addition, a shoulder on the long-wavelength side of the A exciton peak can be observed, for which the fit yields a center wavelength of (687.3 ± 0.2) nm ((1.804 ± 0.001) eV).

The occurrence of this third feature is in good accordance with recent optical experiments with TMDCs, which have proven the presence of optically active *trions* alongside neutral excitons (X^0) [29, 37]. This term describes *charged* excitons, i. e. a bound three-particle system of either two electrons and one hole (negative trion X^-) or one electron and two holes (positive trion X^+).

When comparing the PL wavelength of the A exciton with the band gap of monolayer MoS₂ at cryogenic temperatures (cf. section 2.2), an energy difference of 60 meV can be observed, by which the exciton energy lies below the band gap. Taking into account the splitting energy of 160 meV of the two valence subbands, a similar difference of 50 meV is found for the B exciton.

This deviation from the expected value is due to the exciton binding energy. While the band gap by definition is the minimum energy required for the generation of a quasi-free electron and a quasi-free hole, these two (quasi-)particles usually form a bound state with a hydrogen-like energy spectrum [3, 10]. First principle calculations predict even larger binding energies between 0.5 eV and 1 eV, which are, however, strongly dependent on the dielectric constant of the surrounding medium. The observed difference can thus most likely be attributed to the silicon substrate.

The ground state energy of trions is generally *lower* than that of neutral excitons [61, 64]. Hence, the trion binding energy is usually defined as the *difference* between exciton and trion ground state energy. A comparison of the Lorentz fits for the A exciton and the A⁻ trion results in a trion binding energy of 55 meV, which is about twice as large as previously reported theoretical and experimental results [3, 37]. Again, this difference is most likely to be attributed to the dielectric environment.

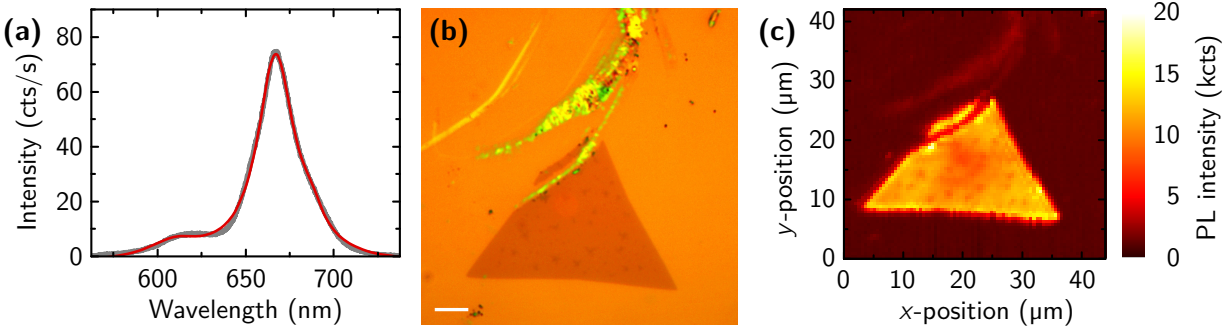


Figure 3.2.: PL measurements with monolayer MoS₂ flakes. **(a)** PL spectrum of a MoS₂ flake recorded at 3 K with a 532 nm excitation laser (grey) with a fit by a sum of three Lorentz curves (red). The two maxima at 667 nm and 610 nm correspond to the A and B excitons, respectively. **(b)** Light microscope image of a MoS₂ flake that was illuminated under the confocal microscope. Scale bar is 5 μm. **(c)** Confocal PL map of the MoS₂ flake. The imaged area was scanned in discrete steps at 3 K with a 532 nm excitation laser.

The full width at half maximum (FWHM) for the fitted Lorentz curves is (12.65 ± 0.05) nm ((35.24 ± 0.14) meV) for the A exciton, (20.2 ± 0.6) nm ((67 ± 2) meV) for the B exciton and (8.7 ± 0.3) nm ((22.8 ± 0.8) meV) for the A⁻ trion. These values are in good agreement with the inhomogeneous broadening from electron-defect scattering of about 66 meV, which has been reported to be the only notable contribution to the linewidth at cryogenic temperatures [54].

Figs. 3.2(b) and 3.2(c) compare a microscope image of a MoS₂ flake with a PL map, which was obtained by scanning over the sample with the confocal microscope in discrete steps and plotting the total PL intensity at each of these points. It is evident that the highest PL intensity comes from the monolayer flake, while the silicon substrate as well as other residues, which appear green on the microscope image, are dark. The PL map shown here was measured at 3 K with a 532 nm laser of 0.35 mW input power and an integration time of 3 s for each measurement point. The PL intensity was obtained by integrating the corresponding spectra from 613 nm to 786 nm.

In addition, polarization resolved measurements were recorded. Figs. 3.3(a) and 3.3(b) show both σ^+ and σ^- circular polarized PL signal for σ^- polarized excitation. In the latter case the input laser of wavelength 639 nm is near-resonant to the A exciton, while in the former case the used 532 nm laser is off-resonant to both the A and the B exciton. Due to the near-resonant excitation in fig. 3.3(b) several laser Raman modes are present in the spectrum in addition to the PL peak of the A exciton [60]. All spectra are cut off at 653 nm by the longpass filter blocking residual laser light.

In both cases a predominantly σ^- polarized PL signal can be observed as is predicted by the valley-selective circular dichroism theory for monolayer MoS₂ (cf. section 2.3). The difference between σ^+ and σ^- polarized PL can be quantified by the *helicity* defined as

$$\rho = \frac{I(\sigma^-) - I(\sigma^+)}{I(\sigma^-) + I(\sigma^+)},$$

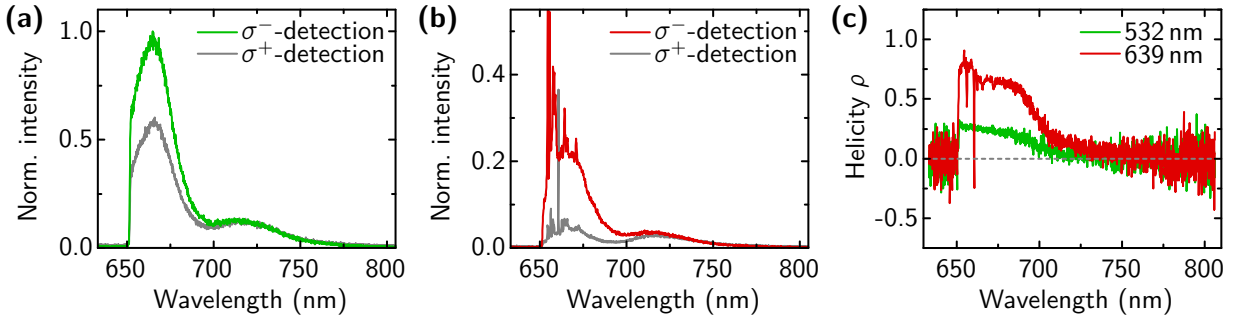


Figure 3.3.: PL of monolayer MoS₂ for σ^- circularly polarized excitation. Spectra are cut off below 653 nm by a longpass filter. **(a)** Circular polarization resolved PL for off-resonant excitation at 532 nm. **(b)** Circular polarization resolved PL for 639 nm excitation near-resonant to the A exciton. Several laser Raman modes are present in addition to the PL peak of the A exciton [60]. **(c)** Degree of polarization given by the helicity of the PL for both 532 nm and 639 nm excitation wavelengths.

where $I(\sigma^-)$ and $I(\sigma^+)$ are the intensities of σ^- and σ^+ polarized PL, respectively. This quantity is shown in fig. 3.3 (c) for both 532 nm and 639 nm excitation wavelengths.

The degree of polarization is higher for excitation with 639 nm near-resonant to the A exciton. In this case polarization is almost perfect close to the A exciton wavelength of 667 nm and helicity is consistently greater than 50 % between 650 nm and 700 nm. By contrast, helicity does not exceed 40 % for off-resonant excitation at 532 nm.

This observation is in good agreement with previous experimental results [38, 77] and can be explained as follows. For near-resonant excitation the PL signal is strongly polarized due to an exciton lifetime (50 ps), which is much shorter than the valley lifetime (1 ns) [38]. For off-resonant excitation, however, non-radiative inter-valley scattering relaxation processes precede the recombination and thereby partially destroy the valley polarization. Hence, a less polarized PL signal is expected.

Very similarly, valley coherence (cf. section 2.3) can be observed by using a linearly polarized excitation laser. Fig. 3.4 (a) shows that valley coherence is vanishing for linearly polarized off-resonant excitation at 532 nm, since the co- and cross-polarized PL signal are similar. For resonant excitation at 635 nm presented in fig. 3.4 (b), however, PL shows a predominant linear polarization which follows the laser excitation angle of 0°. This observation can be explained by the same reasoning as for circularly polarized excitation.

In fig. 3.4 (c) the detected PL intensity depending of the orientation of the linear polarizer serving as analyzer is plotted both for excitation with linear polarization at an angle of 0° (blue circles) and of 90° (red squares). For each data point the corresponding spectrum was integrated around the A exciton from 652 nm to 690 nm and corrected according to the Fresnel coefficients to take into account unequal transmission of different polarizations.

By fitting the characteristics of partially polarized light (solid lines) the degree of polarization was determined to be 61 % for excitation at an angle of 0° and 62 % for excitation at

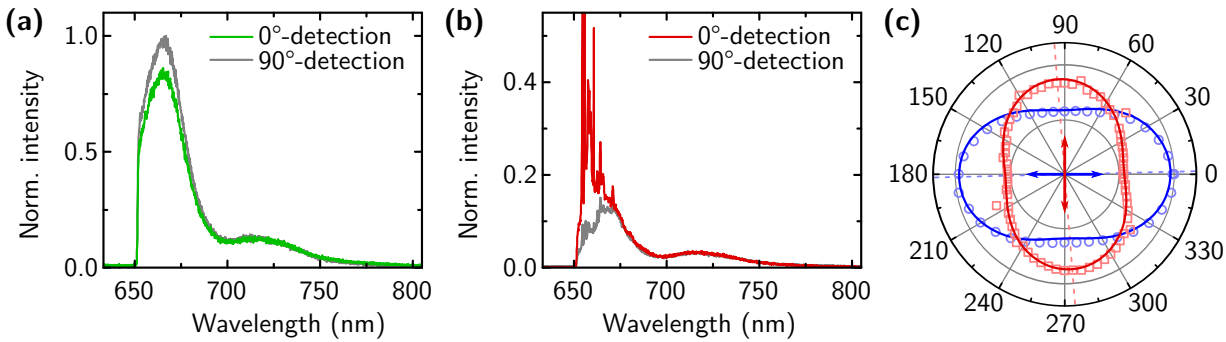


Figure 3.4.: PL of monolayer MoS_2 for linearly polarized excitation. Spectra are cut off below 653 nm by a longpass filter. **(a)** Linear polarization resolved PL for off-resonant excitation at 532 nm polarized at an angle of 0°. **(b)** Linear polarization resolved PL for 639 nm excitation near-resonant to the A exciton and polarized at an angle of 0°. **(c)** PL intensity as a function of the orientation of the analyzing linear polarizer for near-resonant (653 nm) excitation at 0° (blue circles) and 90° (red squares) as indicated by the blue and red arrow. For each data point the corresponding spectrum was integrated around the A exciton from 652 nm to 690 nm and corrected according to the Fresnel coefficients to take into account unequal transmission of different polarizations. Solid lines are fits of characteristics for partially polarized light to the data with a principal axis given by the dashed lines.

an angle of 90°. The same fit also reveals a very small angular deviation of the maximum PL signal from the input polarization of 1.4° and 4.6° for 0° and 90° excitation, respectively, which most likely stems from measurement imperfections.

These measurements clearly show the presence of valley coherence in monolayer MoS_2 for near-resonant excitation, which previously has only been reported for the TMDC WSe_2 [29]. For off-resonant excitation this coherence vanishes again due to non-radiative inter-valley scattering relaxation processes.

3.2. Field effect nanostructures with monolayer molybdenum disulfide

3.2.1. Charge carrier density tuning with an electric field

To investigate the physical properties of both neutral excitons and charged trions (cf. section 3.1.2), it is desirable to tune the charge carrier density in the studied TMDC sample. An excess of electrons and holes is able to favor the formation of negative and positive trions, respectively, and consequently to increase the corresponding optical signal [26, 37].

This goal can most easily be achieved using the well known electric field effect [6, 21]. When a TMDC monolayer is located on a highly doped silicon substrate with a thin layer of

silicon oxide in between, the silicon resistivity is usually low enough ($1.5 \times 10^{-5} \Omega \text{ m}$ for the experiments reported here) to describe this interface as a metal-insulator-semiconductor (MIS) junction [6, pp. 567–571].

Applying a voltage to the silicon substrate serving as gate in the MIS junction, no current is able to flow to the semiconductor owing to the insulator in between. Hence, an electric field builds up in a capacitor-like structure. Unlike metals, which shield electric fields completely, semiconductors allow the electric field to enter tens of nanometers due to a reduced charge carrier mobility [21, p. 78]. The presence of this field shifts the Fermi level inside the semiconductor [6, pp. 597–606].

When the applied voltage and hence the electric field is large enough, the conduction band edge bends below (for a positive voltage) or the valence band edge bends above (for a negative voltage) the Fermi level at the MIS interface. For bulk semiconductors this means that charge carriers accumulate at the junction, thereby shielding the interior of the semiconductor from the external field. For a positive voltage a two-dimensional electron gas (2DEG) and for a negative voltage a two-dimensional hole gas (2DHG) forms with some ten nanometers in width [21, pp. 78–79].

Since monolayer TMDCs flakes have a thickness of only about 1 nm, applied electric fields typically fully penetrate the crystal. Unlike for bulk semiconductors, the field effect causes an equal shift of the charge carrier density in all of the flake. In particular, when electric contacts to a TMDC flake are added, a FET like structure is obtained [21, pp. 78–81]. This FET has the additional advantage that its resistance can be used to monitor the shift of the charge carrier density in the TMDC by a simple current-voltage measurement.

In summary, a field effect configuration is a promising setup for a selective optical activity enhancement of the neutral exciton X^0 and both of the trions X^+ and X^- . For this involved sample preparation procedures are necessary, which are discussed in the following section.

3.2.2. Device fabrication by laser lithography

Photolithography is a widely used method for creating microelectronic circuits on samples like silicon wafers with an insulating layer of silicon oxide on top. Several variants of the working scheme have developed, which, however, all share the same general workflow. Five main steps can be distinguished [36, 50].

Photoresist application. A *photoresist*, usually a polymer that changes its physical properties when exposed to ultraviolet radiation, is applied to the sample. This can be done by *spin coating*, i. e. by rotating the sample with a high angular velocity and dropping some photoresist on the sample center. Due to centrifugal force a thin and homogeneous layer of photoresist forms.

Illumination. Parts of the sample are selectively illuminated by ultraviolet light, causing chemical changes of the photoresist in those parts exposed to the radiation. Several approaches are used for defining the exposed and unexposed areas, respectively. Frequently, a *photomask*, which is optically transparent in the appropriate parts, is brought between the sample and the light source for this purpose.

Development. By application of a chemical *developer*, normally some kind of lye, either the chemically altered or the chemically unaltered parts of the photoresist are removed, depending on whether a *positive* or *negative* photoresist has been used. Frequently, a *lift-off resist* is applied to the sample before the photoresist as additional layer. It is also solvable by the developer (or a different chemical to which the photoresist is inert) and simplifies the lift-off step by ensuring steeper photoresist edges [17].

Deposition. Onto the sample with partially removed photoresist (and lift-off resist, if present) a thin layer of metal is deposited, typically some ten nanometers of gold. This can be achieved e. g. using an ultra high vacuum (UHV) e-beam evaporator that vaporizes metal by heating with a focused electron beam.

Lift-off. The remaining photoresist (and lift-off resist, if present) is removed usually by some organic solvent. This step also carries away any metal deposited on top of the remaining photoresist, so that metal only remains at points that have already been cleared of the photoresist in the development step. That way arbitrary wire layouts can be defined for microelectronic purposes.

Monolayer TMDCs offer various properties that make them ideal candidates for building lithographically structured devices. First, wires can be led right over them without expecting damage, since monolayer TMDCs with a typical height of 1 nm are much flatter than the deposited wires with about 50 nm thickness. Second, TMDC flakes can span several micrometers in lateral dimension such that reasonably large structures can be used even when creating sophisticated lithographic designs. Third and most importantly, monolayer TMDCs on a silicon sample with silicon oxide layer show sufficient contrast under the optical microscope due to interference effects [5]. This property makes them easy to be visualized for aligning structures with respect to TMDCs present on a given sample.

To exploit these advantages, the method of laser lithography was employed throughout this work for gate patterning processes. For prototype samples with unique circuit designs this procedure benefits from outstanding simplicity compared to other approaches. Whereas photolithography usually relies on the availability of appropriate photomasks, laser lithography is a maskless method, thus rendering time-consuming creation of single-use photomasks unnecessary. Instead, desired shapes are created by an illuminating laser with diffraction limited spot size scanning over the sample in discrete steps.

To this end, the necessary lithographic tasks were performed using the ProtoLaser LDI (laser direct imaging) system provided by LPKF Laser & Electronics AG. This laser lithographic device is easily set up inside a cleanroom due to its small size (cf. fig. 3.5 (a))

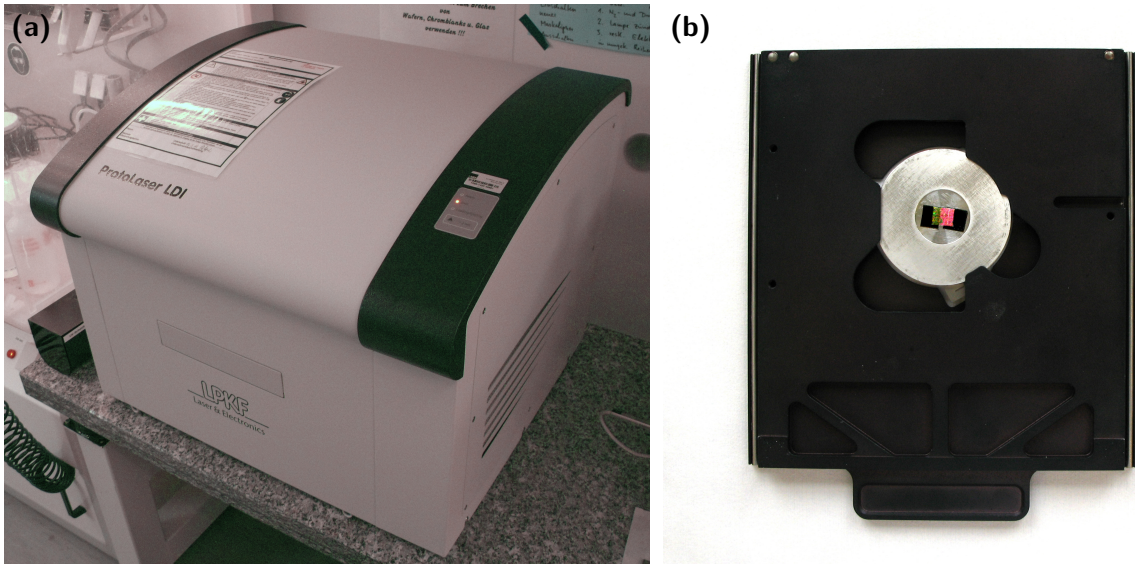


Figure 3.5.: (a) Image of the ProtoLaser LDI system. (b) Silicon sample fixed to an aluminum adapter plate by carbon tape inside 2 inch tray of the ProtoLaser LDI system.

and offers two major advantages for building field effect nanostructures with monolayer MoS₂ compared to other approaches.

1. The device is shipped together with a computer-aided design (CAD) software that allows for on-the-fly design of structures as well as for import of predefined layouts using wide-spread data formats like the Drawing Interchange Format (.dxf) or the Gerber format (.gb1) [28, p. 18].
2. A built-in microscope camera permits alignment of the previously defined structures on the sample with sub-micrometer accuracy. This feature allows for electrically contacting individual MoS₂ flakes in a controlled and reproducible manner.

Despite the aforementioned advantages of the ProtoLaser LDI system laser lithography remains an involved task facing difficulties of several kinds. The most important steps of the typical workflow are discussed in the following.

Sample imaging. High resolution images of the to be processed sample are indispensable both for designing a suitable wire layout and for proper alignment using the built-in microscope camera of the ProtoLaser LDI system. Obtaining such images with a camera equipped microscope is a nontrivial task for millimeter-sized samples with micrometer-sized structures.

The simplest way to circumvent this obstacle is to use an objective with high magnification and to capture several images of different regions that in total cover the whole sample. These images can afterward be combined using a stitching software like Hugin [1] or the

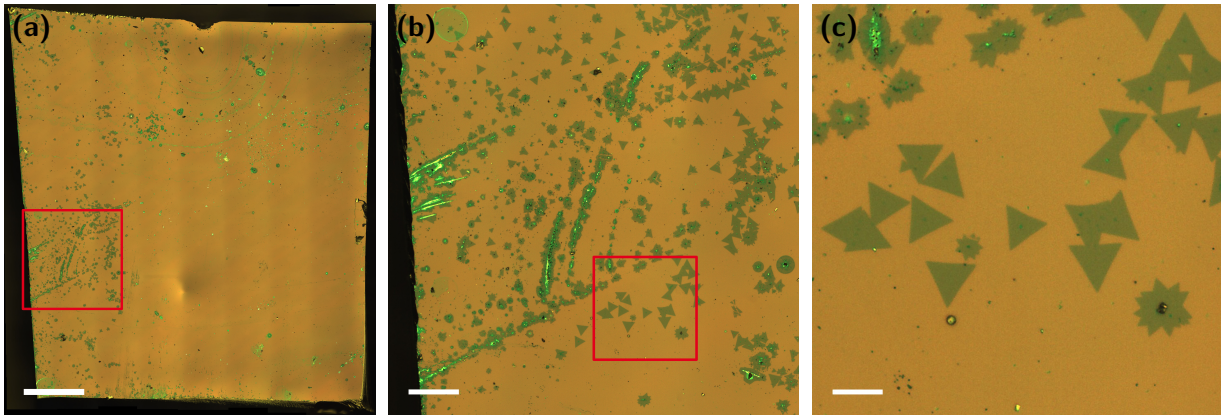


Figure 3.6.: High resolution images of monolayer MoS₂ flakes on a silicon sample with a 100 nm silicon oxide layer. **(a)** Full sample. Scale bar is 500 μm . **(b)** Sample region populated by various MoS₂ flakes. Scale bar is 100 μm . **(c)** Individual MoS₂ flakes. Scale bar is 25 μm .

ImageJ distribution Fiji [48, 56]. The outcome of this procedure is an image with sufficient resolution to view the sample as a whole (cf. fig. 3.6 (a)), in specific regions with high density of MoS₂ flakes (cf. fig. 3.6 (b)) or at the level of individual flakes (cf. fig. 3.6 (c)).

Wire layout design. The layout of the lithographically defined wires providing electric contact to individual MoS₂ flakes is predominantly influenced by the surface features of the specific sample in use. Usually one has to satisfy the competing demands to leave as many interesting flakes intact as possible and to lead the circuitry around residues and other surface impurities that are likely to complicate the further process.

Therefore, it is desirable to use the previously created high resolution image of the sample as a background image for reference during the design of the wire layout. However, while the CAD software provided for the ProtoLaser LDI system offers sophisticated tools for defining individual structures in an easy manner, like several other comparable programs it lacks the possibility to use background images.

An alternative was found in the vector graphics editor Inkscape [19]. This program not only offers tools to manipulate schematic drawings similar to that of CAD software but comes with an extensive bitmap image control. This way the high resolution image of the sample can be scaled to match the actual size of the sample with micrometer accuracy.

Fig. 3.7 (a) shows the general wire layout design of the studied MoS₂ sample. It was chosen such that in total four MoS₂ flakes are addressed (cf. fig. 3.7 (b)) and that each of the five electric contacts (color coded red, orange, yellow, green and blue) provides two gold pads for attaching bond wires [24, pp. 265-266]. The use of two connections instead of only one gives rise to the possibility to check the functionality of each wire by a simple resistance measurement even after mounting the sample and cooling it to cryogenic temperatures.

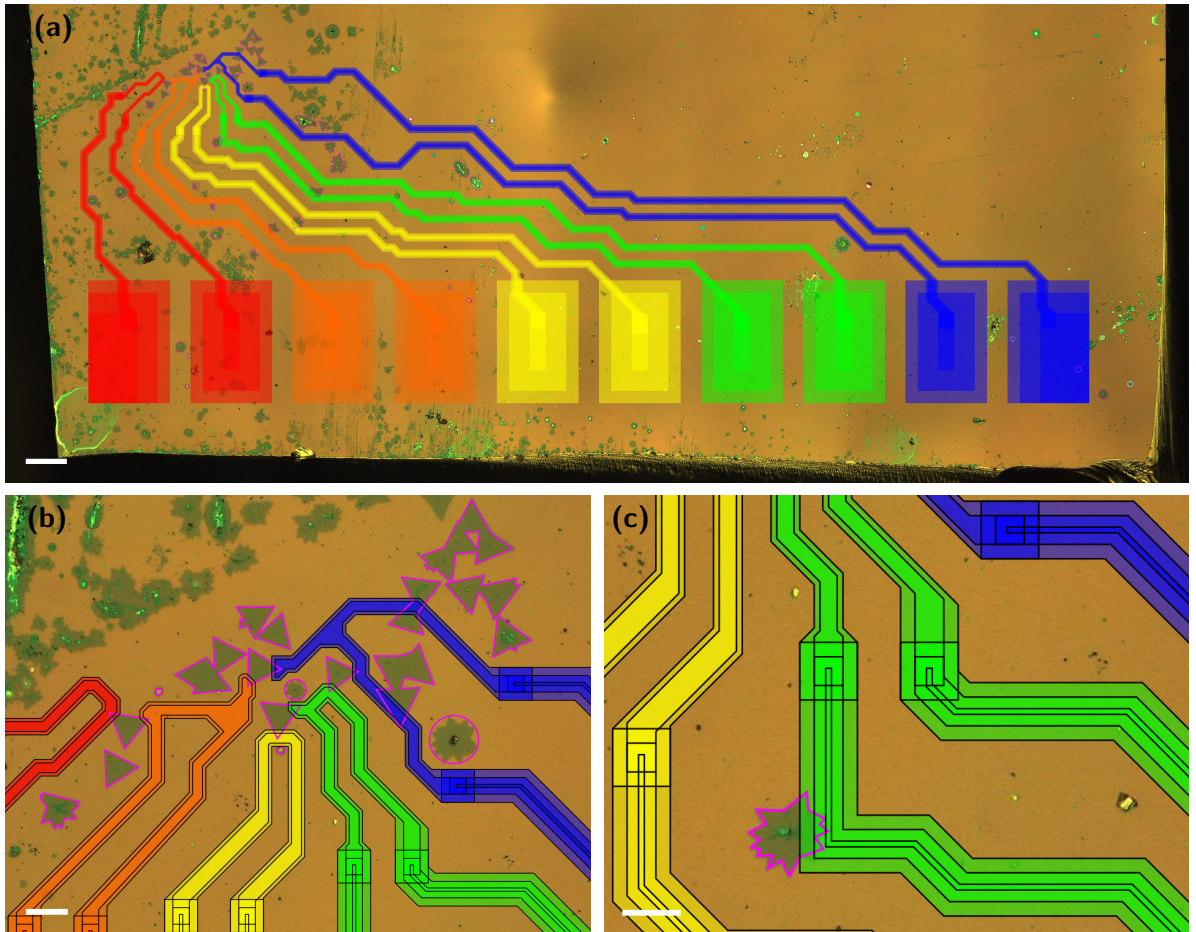


Figure 3.7.: (a) Wire layout overview created with Inkscape using the high resolution image of fig. 3.6 as reference. Scale bar is 100 μm . **(b)** Tips of the lithographic wires provide contact to four MoS_2 flakes. Several flakes and other prominent structures are marked as reference points. Scale bar is 25 μm . **(c)** The graded wire structure varies in different parts of the layout and consists of two or three regions that differ in their respective illumination dose. Scale bar is 20 μm .

Hence, potential sample malfunctioning caused by damaged electrical contacts or detached bond wires can be ruled out at any time without the need for an optical inspection.

When designing lithographic structures on samples with millimeter dimensions rather than on larger wafers, further care has to be taken. Spin coating photoresist onto a substrate usually results in beads at the sample edges due to centrifugal forces and the resist viscosity. For small samples this leads to an uneven photoresist thickness over large parts of the surface area. In particular, the wire layout has to make sure that parts of the sample with a thicker photoresist layer – thus requiring longer exposure times – receive a sufficient illumination dose for satisfactory development results, while the rest of the sample does not get overexposed. Therefore, the wires were designed in a graded structure (cf. fig. 3.7(c)) and the illumination dose was chosen to increase in up to three steps toward their centers.

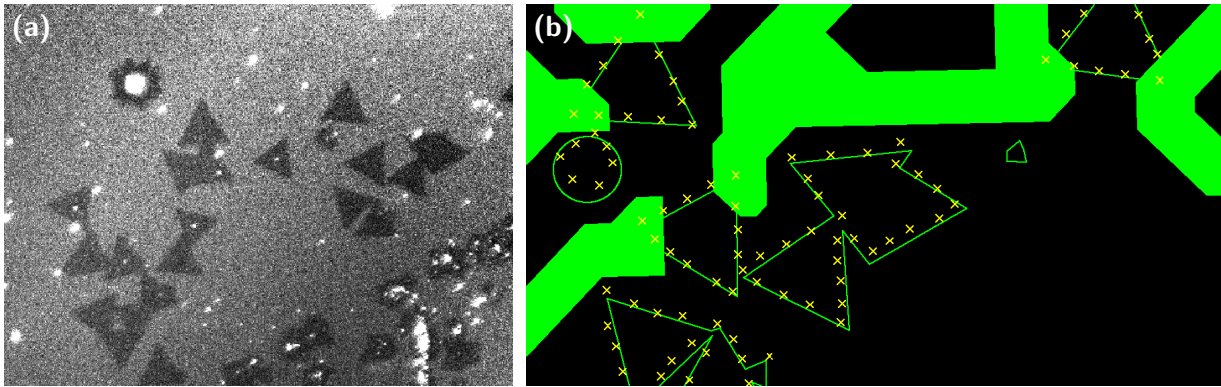


Figure 3.8.: (a) An image of the silicon sample with 100 nm silicon oxide layer captured by the microscope camera of the ProtoLaser LDI system showing several MoS₂ flakes. **(b)** Anchor points (yellow) in the ProtoLaser LDI CAD software aligned to previously defined contours (green) of MoS₂ flakes, which have been identified using the high resolution image of fig. 3.6.

This choice satisfies both of the given demands: The highly exposed centers of the wires will receive a sufficiently large illumination dose to be properly developed even for a rather thick layer of photoresist while the wire edges are less exposed to avoid overexposure. The latter prevents structures designed to be distinct from accidentally becoming connected due to illumination of the photoresist in between by stray light. Hence, depending on the thickness of the photoresist layer the width of the wires may vary (cf. fig. 3.9 (a)) but the resulting structures offer full control over the electronic properties of the device.

Photoresist application. Before starting lithography, the sample has to be covered with a suitable photoresist. For best results a combination of MicroChem (Dow) Microposit® S1813® photoresist together with MicroChem LOR 3B lift-off resist was used. The purpose of the additional lift-off resist is to achieve an undercut (cf. figs. 3.9 (b) and 3.9 (c)) in order to simplify the later lift-off procedure and to minimize the probability of damaged lithographic structures [17]. The following working scheme was applied:

1. Spin coating of LOR 3B for 35 s at 8000 rpm with an acceleration of 4000 rpm/s. Slightly eccentric positioning of the sample on the spin coater can help to reduce the edge beads.
2. Soft bake at 150 °C for 90 s.
3. Spin coating of S1813 for 35 s at 8000 rpm with an acceleration of 4000 rpm/s. Again, slightly eccentric positioning of the sample on the spin coater can help to reduce the edge beads.
4. Soft bake at 115 °C for 90 s.

Tips			Wires				
Tool	Dose [mJ/cm ²]	Spacing [μm]	Tool	Dose [mJ/cm ²]	Spacing [μm]		
1	Fine	20	0.1	1	Fine	1000	0.1
2	–	–	–	2	Coarse	100	0.3
3	Fine	5	0.1	3	Coarse	10	0.3

Pads			
Tool	Dose [mJ/cm ²]	Spacing [μm]	
1	Coarse	1500	0.3
2	Coarse	250	0.3
3	Coarse	20	0.3

The diagram shows a cross-section of a pad. It consists of three distinct horizontal layers. The top layer is red and labeled 'Region 1'. The middle layer is blue and labeled 'Region 2'. The bottom layer is green and labeled 'Region 3'. This visualizes the graded structure of the illumination doses defined in the table.

Table 3.1.: Tool type, illumination dose and spot spacing options defined using the ProtoLaser LDI CAD software for the respective regions in tips, wires and pads. The definition of the three regions can be seen from the illustration.

Alignment and illumination. The ProtoLaser LDI system provides three trays for 2 inch, 3 inch or 4 inch silicon wafers. For mounting smaller samples as used in our experiments, a home-built 2 inch aluminum adapter plate was used, as shown in fig. 3.5 (b). The samples can then easily be fixed to the adapter plate by carbon tape irrespective of their actual size. For this step, however, special care has to be taken to level the sample on the tape as evenly as possible, since the ProtoLaser LDI system can only correct sample inclinations of 27 mrad [28, p. 39].

After loading the sample into the device and performing sample niveling [28, pp. 27–31] the built-in microscope camera of the ProtoLaser LDI system can be used to set reference points for alignment of the previously defined wire layout. Fig. 3.8 (a) shows a recorded image of several MoS₂ flakes, which are easily identified by their optical contrast. Added anchor points [28, p. 35] at the edges of MoS₂ flakes or other distinct structures are automatically transferred to the CAD window (cf. fig. 3.8 (b)) and can then be used for alignment.

The illumination dose for the wire layout is defined using the CAD software provided for the ProtoLaser LDI system. Most promising results were obtained with three different illumination doses for the tips contacting the MoS₂ flakes, the pads later used for bonding and the wires connecting tips and pads. Each of these three parts is further divided into a graded structure of two (tips) or three (wires and pads) regions to account for varying thickness of the spin coated photoresist. Table 3.1 shows the following parameters that differ for the various components in order to obtain optimal results [28, p. 26]:

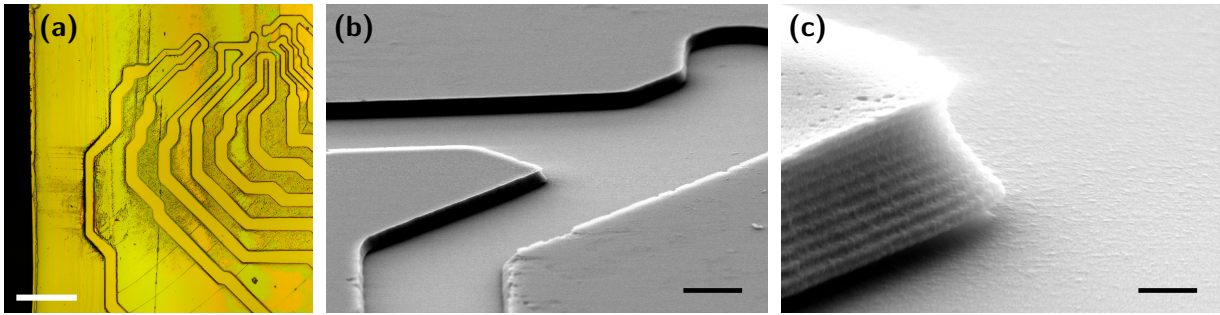


Figure 3.9.: Lithographic results after illumination and development. **(a)** Photoresist on a clean silicon sample after illumination and development. The width of leftmost wire varies due to photoresist edge beads and graded illumination profile but is not interrupted. Scale bar is 100 µm. **(b)** SEM image of a larger sample area showing both illuminated and unexposed regions. Scale bar is 500 nm. **(c)** SEM image of border of illuminated area shows undercut due to use of LOR 3B and a steplike photoresist edge owed to interference of incoming and back-reflected laser beams. The height of the undercut was measured to be around 160 nm while its depth varies largely over the sample. Scale bar is 500 nm.

Tool. The ProtoLaser LDI system offers two different illumination tools, namely a laser with spot size 1 µm (fine tool) and a laser with spot size 3 µm (coarse tool). While the fine tool allows for structures with smaller features and more detailed results, the coarse tool offers a shorter operation time due to a higher working speed.

Dose. The deposited energy dose per area is the most important parameter, as it directly determines how well and how quickly the photoresist will be developed.

Spacing. This parameter governs the distance between two laser spots when the laser of the ProtoLaser LDI system scans over the defined wire layout to expose the sample. Smaller spot spacing allows for finer details but increases operation time.

The actual illumination is then simply started using the software of the ProtoLaser LDI system [28, p. 33] and does not involve any further manual interaction or alignment. For the structures used on this sample the operation time was only in the order of few minutes.

Development. After illumination the sample was removed from the sample holder and developed in a 1 : 3 mixture of MicroChem (Dow) Microposit® 351 developer and water for 90 s. Typical results of this procedure are shown in fig. 3.9 by means of different microscopic images of exposed photoresist after development.

Fig. 3.9 (a) shows the effect of a changing wire width due to a varying photoresist thickness in the vicinity of the sample edge. However, the wire is not interrupted as would be the case without the use of regions with different illumination doses.

To learn more about the quality of the lithographic result a scanning electron microscope (SEM) was used to image the sample (cf. fig. 3.9 (b)). Fig. 3.9 (c) shows a detail of the

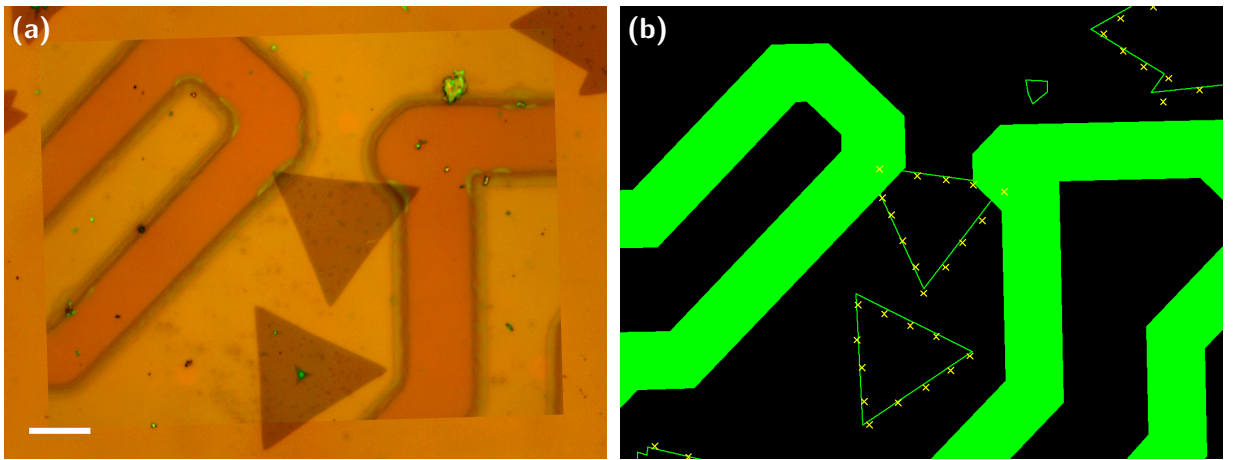


Figure 3.10.: Alignment of developed photoresist as compared to anchor points in the ProtoLaser LDI CAD software. **(a)** Superposition of microscopic images before and after spin coating, illumination and development of photoresist. Scale bar is $10\text{ }\mu\text{m}$. **(b)** Comparison to previously defined anchor points in the ProtoLaser LDI CAD software reveals a displacement of about $2\text{ }\mu\text{m}$.

processed photoresist edge including two prominent features. First, the undercut due to the use of LOR 3B can be clearly identified. Its height was measured to be around 160 nm while its depth varies largely over different parts of the sample.

Second, the photoresist edge shows a steplike structure. This effect originates from interference of the incoming laser and its reflection at the sample surface [50, pp. 42–56]. In the case of the ProtoLaser LDI system this effect appears to be the main obstacle for obtaining sharp photoresist edges with a desired angle of 90° or more with respect to the sample surface. A possible solution of this issue is discussed in appendix A.

In addition the positioning accuracy of the lithographic wires was inspected. Fig. 3.10 (a) shows a superposition of two microscope images of the MoS_2 flake between the wires color coded as red and orange captured before and after performing lithography. The images have been aligned using the position of the clearly visible MoS_2 flake that can safely be assumed to remain unaltered.

Comparison with the saved anchor points in the ProtoLaser CAD software in fig. 3.10 (b) reveals a spacial displacement of the wires of about $2\text{ }\mu\text{m}$. For the use of the workflow sketched so far it is of course of high importance to know about such offsets in order to respect them in advance. To date, however, it is not clear whether distance and direction of this displacement are reproducible between different runs or whether they depend for example on the accuracy of the sample niveling, so that further investigation of this issue appears necessary.

3.2.3. Electric contacting of the sample

After defining the lithographic structures using the ProtoLaser LDI system the actual electric contacting of the sample was performed. The sample was brought to a UHV e-beam evaporator and the wires were deposited. A typical two layered structure was used consisting of 50 nm gold on top of 3 nm titanium serving as adhesive agent to the silicon substrate.

The remaining photoresist was then removed together with all unwanted metal on top of the resist in a usual lift-off step for which the sample was left in dimethyl sulfoxide (DMSO) at 80 °C for about two hours and afterward cleaned in isopropyl alcohol. Due to suboptimal photoresist edges (cf. appendix A), usually some gold residues stick to the sample and have to be removed manually.

The simplest and safest way to do so is fixing the sample in a beaker with isopropyl alcohol (e. g. using tweezers) and creating a liquid flow near the sample surface by pressing the ball of a pipette repeatedly. In case this method does not yield sufficient results, an ultrasonic bath at the lowest power for a short time is recommended. Here a Sonorex Digital DK 102 P ultrasonicator was employed at 10 % of the possible 2 × 240 W ultrasound power at 35 kHz for one minute. Since ultrasonication at elevated power is more likely to damage the lithographic structures, a repetition of the ultrasonic cycle at lowest power should always be preferred if necessary. The resulting wires after the lift-off procedure can be seen in fig. 3.11.

Since SEM imaging is likely to damage the MoS₂ layers on the sample, most information on the quality of the deposited gold wires can be obtained from AFM images of the contacted flakes and their surroundings. Such images are shown in fig. 3.12, in which flakes and substrate are color-coded in orange while wires are color-coded in green in order to increase contrast for both parts. The MoS₂ flakes are still well distinguishable even under a layer of 50 nm of gold as shown in fig. 3.12 (b). In particular, fig. 3.12 (a) reveals that the left

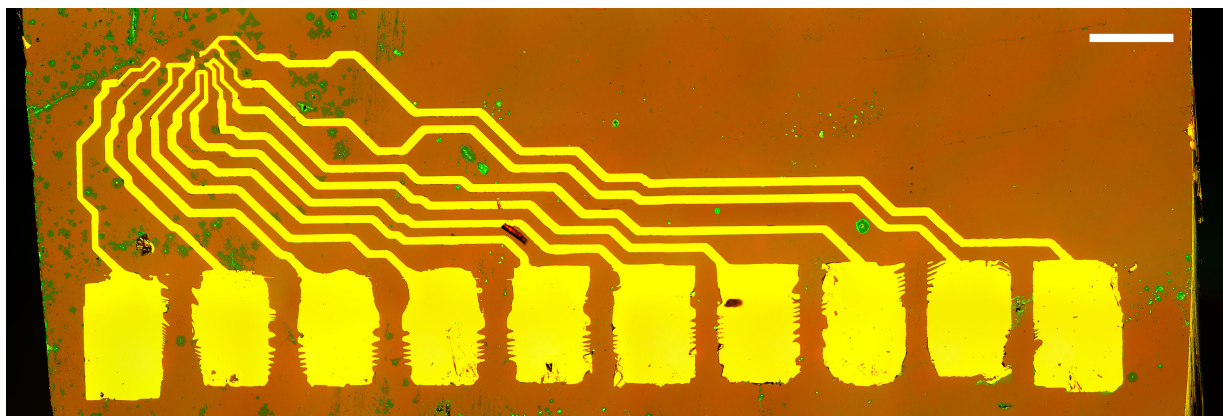


Figure 3.11.: Microscope image of lithographically defined wires after lift-off. Scale bar is 100 µm.

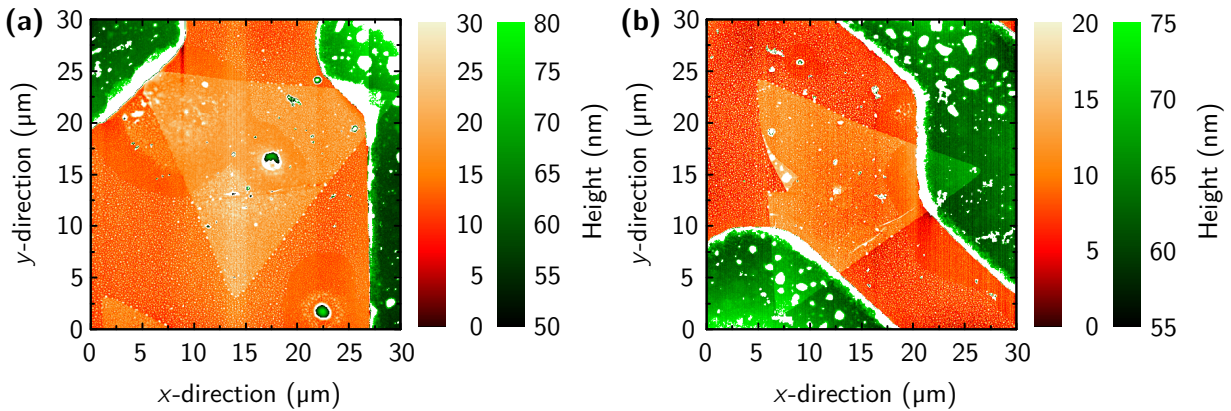


Figure 3.12.: AFM images of two contacted MoS₂ flakes. For increased contrast two different color scales representing the height measured by the AFM have been used, so that silicon substrate and MoS₂ flake are depicted in orange while the lithographic gold wires and some impurities appear in green. Interestingly, the flakes are still clearly visible below a 50 nm gold layer. **(a)** MoS₂ flake between red (left) and orange (right) color-coded wire (cf. fig. 3.7). The left top tip of the flake is visible under the gold layer of the red wire suggesting electric contact at this point despite a different indication in fig. 3.10 (a). **(b)** MoS₂ flake between green (bottom left) and blue (top right) color-coded wire.

(red) electrode actually covers parts of the flake although fig. 3.10 (a) is most likely to be interpreted otherwise.

It is evident that the wires are highest at their borders, again indicating photoresist edges that are less steep than desired. For nonvertical edges, there is no clear separation between metal deposited directly on the sample and metal deposited on top of the photoresist. Instead, the metal film follows the rising slope of the photoresist without leaving any gap, thus leading to elevated boundaries and a more difficult lift-off procedure (cf. appendix A)

In order to make use of the lithographic wires, a connection to cables has to be established. This is done in two steps: First, twisted pair cables are soldered to soldering pads made from galvanically deposited copper on a thin polyimide foil. Both these soldering pads and the sample are then glued using UHU® plus endfest 2-K-Epoxidharzkleber to home-built titanium sample holders.

Second, a connection between the copper pads and the lithographically defined pads on the sample is established by attaching gold wires with the method of ultrasonic bonding. In this process, a gold wire is pressed on a metallic surface and welded to it by application of an ultrasonic pulse [24, pp. 265–266]. The wire can then be pulled to another metallic surface and the welding process is repeated, thus establishing an electric contact between both parts. While bonding a gold wire onto gold pads is straightforward, bonding gold onto copper requires more care. Especially the used copper pads supported by a polyimide foil are challenging to contact, as the elastic foil absorbs much energy of the ultrasonic pulse, leaving back a weak bond connection.

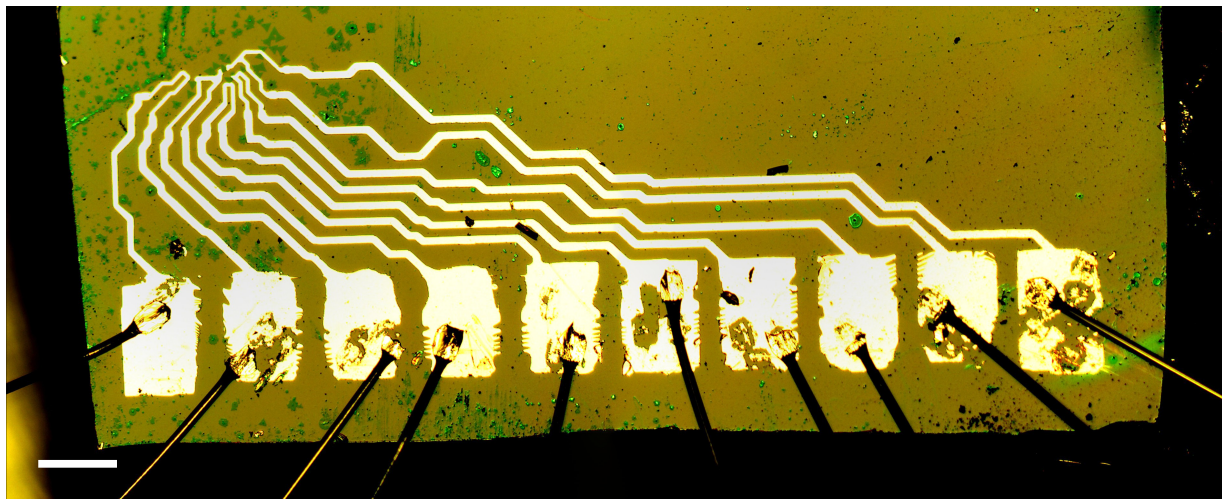


Figure 3.13.: Microscope image of bond wires attached to lithographically defined bond pads. Scale bar is 100 µm.

In order to obtain the most reproducible results, the following points should be taken into account: To make the bonds on copper as stable as possible it has proven useful to use ultrasonic pulses of maximum energy and length. Also the heating temperature of the wire can influence the bond quality. The best results were obtained using an elevated temperature making the wire more flexible, which however must not be too high either, since otherwise the bond wires are more likely to break.

For the used combination of a Marpet Enterprises Inc. 1204W hybrid wedge bonder together with a Uthe Technology Inc. 10G ultrasonic controller a power level of 10 and a time level of 10 for bonding gold onto copper as well as a power level of 6 and a time level of 6 for bonding gold onto gold with temperature kept at level 7 to 8 were found to be most promising. In any case, a spare bond needle should be used, since operation with high-energy pulses quickly oblates the groove that is needed for bond connections finer than the ones used here.

Fig. 3.13 shows the resulting bond connections. It can be seen that some of the bond pads have suffered damage as compared to fig. 3.11. This is inevitable, since the quality of a bond needle worsens with each bond, so that some of the bonds on the gold pads can detach and leave the gold layer damaged.

In order to obtain a FET like structure to tune the charge carrier density in the chosen MoS₂ flakes, also the underlying silicon substrate has to be electrically contacted to serve as a back gate. Despite the use of highly boron doped silicon with resistivity below $1.5 \times 10^{-5} \Omega \text{ m}$ it is not sufficient just to attach a wire e.g. using conducting silver. This would result in a Schottky barrier between the semiconducting silicon substrate and the metallic wire [57, 58], causing unwanted insulating behavior in particular at cryogenic temperatures.

As an alternative approach a method of local doping was used. For this two boron doped gold wires were brought close to the roughened edge of the silicon substrate and a charged 1000 µF

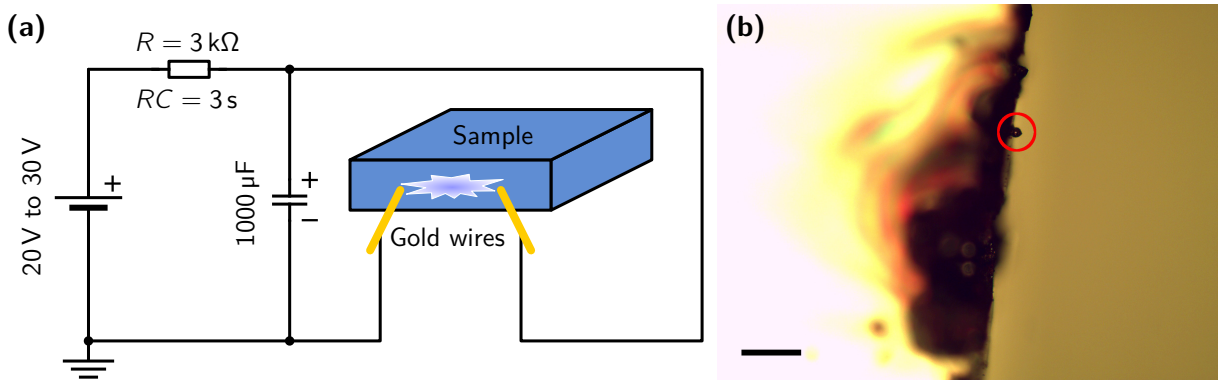


Figure 3.14.: Electrical contacting of a highly boron doped silicon substrate by the method of local doping. **(a)** Schematic drawing of electrical circuit. Voltage applied between boron doped gold wires using the 1000 μF capacitor leads to an arc discharge through the silicon sample causing local doping and deposition of gold beads. **(b)** Microscope image of gold beads at the edge of silicon sample with one prominent bead highlighted by a red circle. Scale bar is 100 μm .

capacitor was used to apply a voltage of 20 V to 30 V between them. On decreasing the distance between the wires eventually an arc discharge occurred, as depicted schematically in fig. 3.14 (a).

When located close enough to the silicon sample the arc will preferably choose its way *through* the highly doped silicon as this path offers lower electric resistance than air. Due to heating of the wire tips, some boron doped gold evaporates and penetrates the silicon leading both to local doping with gold and deposition of small gold beads on the sample edge (cf. fig. 3.14 (b)). The gradual nature of this doping effect then prevents any Schottky barriers and thus offers ohmic behavior of the established contact (cf. section 3.2.4).

The actual electrical contact to the silicon substrate is then performed by bending a thin wire to touch the sample edge at the position of the local doping. The application of a small droplet of conducting silver is sufficient to establish an electrical connection to the previously deposited gold beads and thus to the silicon substrate.

3.2.4. Sample characterization by electrical transport measurements

In order to understand the electrical properties of the sample, several transport measurements have been performed. The main results are discussed in this section.

Quality of the electrical contacts. To start with, the bond connections and the contacts to the back gate have been tested. Since each of the five color-coded lithographic wires and the back gate are contacted twice, all connections can be evaluated by a simple resistance measurement.

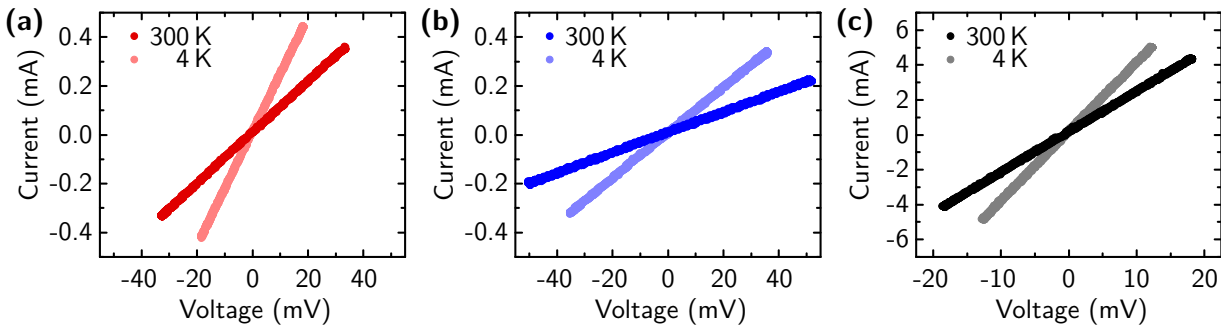


Figure 3.15.: Resistance measurements for different sample contacts (cf. fig. 3.7).

(a) Current-voltage characteristics for the red color-coded wire at 300 K (dark red) and 4 K (light red). The resistance is found to be 100Ω at 300 K and 45Ω at 4 K. **(b)** Current-voltage characteristics for the blue color-coded wire at 300 K (dark blue) and 4 K (light blue). The resistance is found to be 240Ω at 300 K and 110Ω at 4 K. **(c)** Current-voltage characteristics for the back gate at 300 K (black) and 4 K (grey). The resistance is found to be 4.5Ω at 300 K and 2.5Ω at 4 K.

Current-voltage characteristics at room temperature as well as at 4 K for the red and blue color-coded wire are shown in figs. 3.15(a) and 3.15(b), respectively. The dependence is clearly linear indicating well conducting ohmic contacts. To support this observation, the measured resistances can be compared to the expected values taking into account the resistivity of gold.

The lengths of the two wires measure roughly $1330\mu\text{m}$ for the red and $4300\mu\text{m}$ for the blue wire. For simplification a uniform width of $20\mu\text{m}$ and a height of 50nm is assumed over the whole length. Using the resistivity $2.271 \times 10^{-8}\Omega\text{ m}$ of gold [32, p. 12-45] at 300 K one obtains:

$$R_{\text{red}}(300\text{ K}) = 2.271 \times 10^{-8} \Omega\text{ m} \times \frac{1330 \times 10^{-6} \text{ m}}{20 \times 10^{-6} \text{ m} \times 50 \times 10^{-9} \text{ m}} = 30.2\Omega$$

$$R_{\text{blue}}(300\text{ K}) = 2.271 \times 10^{-8} \Omega\text{ m} \times \frac{4300 \times 10^{-6} \text{ m}}{20 \times 10^{-6} \text{ m} \times 50 \times 10^{-9} \text{ m}} = 97.7\Omega$$

These values differ by similar factors of 3.3 and 2.5 from the measured values of 100Ω and 240Ω , respectively. This difference in resistance can be accounted for by surface effects, which are negligible in bulk conductors but of high importance for lithographically created gold wires of only 50 nm height. Using the resistivity $2.22 \times 10^{-10}\Omega\text{ m}$ for gold [32, p. 12-45] at 4 K, a qualitatively similar result is obtained:

$$R_{\text{red}}(4\text{ K}) = 2.22 \times 10^{-10} \Omega\text{ m} \times \frac{1330 \times 10^{-6} \text{ m}}{20 \times 10^{-6} \text{ m} \times 50 \times 10^{-9} \text{ m}} = 295\text{ m}\Omega$$

$$R_{\text{blue}}(4\text{ K}) = 2.22 \times 10^{-10} \Omega\text{ m} \times \frac{4300 \times 10^{-6} \text{ m}}{20 \times 10^{-6} \text{ m} \times 50 \times 10^{-9} \text{ m}} = 955\text{ m}\Omega$$

Again the measured values of 45Ω and 110Ω differ by similar factors of 153 and 115, respectively. The larger deviation at 4 K is owed to a by two orders of magnitude smaller

resistivity of gold than at room temperature, such that the relative contribution of surface imperfections is larger.

The similar ratios between measured and calculated resistances at both temperatures indicate that the major contribution to the resistances is given by the resistivity of gold and surface effects and not by the contacts or the cables leading to the sample. In particular, all bond connections can be assumed ohmic and to show virtually no resistance.

An analogous measurement was performed with the back gate by running current through the two contacts attached to it. It was found to show an ohmic behavior as well with a resistance of 4.5Ω at 300 K and of 2.5Ω at 4 K (cf. fig. 3.15 (c)). Hence, also this contact can be assumed to behave ideally.

Leakage currents. Between any unconnected wires perfect insulating behavior is desired, which in reality is difficult to achieve. This is due to leakage currents between different connections, which have to be investigated further and borne in mind for all future measurements.

The largest leakage currents occur between the back gate and the used titanium sample holder corresponding to a resistance of only few kilohms. This contact is probably due to a damage of the thermal silicon oxide at the bottom of the sample caused by the method of local doping described in section 3.2.3. In addition some of the created gold beads may by chance contribute to this electric contact.

Knowing about this leakage current is highly important, since the sample holder is usually mounted onto a piezo stack with a titanium housing (cf. section 3.1.1), which is grounded. In order to apply arbitrary potentials to the back gate whilst keeping other metallic parts of the setup at ground potential, it is thus recommended to electrically insulate the titanium sample holder. This can most easily be achieved by adding a plate of plastic as insulating layer and fixing the sample using plastic screws instead of metallic ones.

Moreover, there also exist leakage currents between the back gate of the sample and the gold wires used to contact the MoS₂ flakes, i. e. currents running through the 100 nm layer of silicon oxide on top of the sample. The circuit used for measuring these leakage currents is shown in fig. 3.16.

In order to obtain a current-voltage characteristic, varying voltages were applied to the back gate with a Yokogawa 7651 voltage source. Since high currents through the oxide layer are likely to damage the sample, an additional current limiting resistor was used together with a Keithley 2002 multimeter to measure the actual voltage at the back gate. Unlike most other multimeters it offers an input resist of $100\text{ G}\Omega$ and is therefore suitable for circuits featuring gigaohm resistances. The actual leakage current was measured using an Ithaco 1211 current-voltage converter together with an Agilent 34411A multimeter.

All unused bond pads were unplugged to exclude the occurrence of any additional leakage currents, leaving their potentials floating, i. e. undefined. In addition, the whole setup

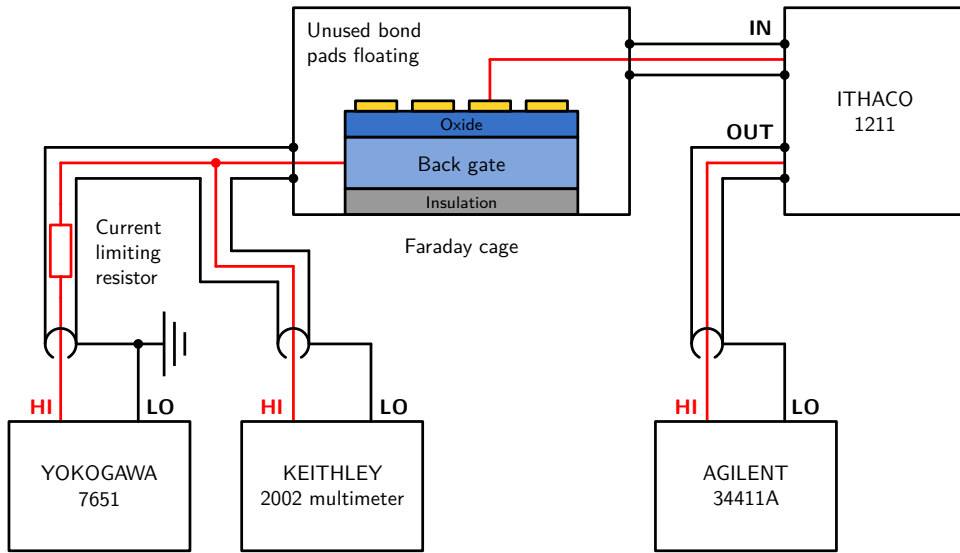


Figure 3.16.: Circuit used for measurement of leakage currents. Varying voltages were applied to the back gate with a Yokogawa 7651 voltage source using a current limiting resistor of $1\text{ G}\Omega$ to avoid sample damage. A Keithley 2002 multimeter was employed to measure the back gate voltage, since unlike other multimeters it offers an input resist of $100\text{ G}\Omega$ and is therefore suitable for use in circuits featuring gigaohm resistances. The leakage current through the 100 nm layer of silicon oxide on top of the silicon sample to the different lithographic gold wires was measured using an Ithaco 1211 current-voltage converter together with an Agilent 34411A multimeter. Unused bond pads were unplugged leaving their corresponding electric potentials floating, i. e. undefined in order to avoid additional leakage currents involving these pads. The whole setup was shielded to prevent inductive currents. For this purpose coaxial cables have been used exclusively, while the sample itself was stored in a Faraday cage, i. e. a metallic box.

was shielded to avoid inductive currents. For this purpose coaxial cables have been used exclusively, while the sample itself was stored in a Faraday cage, i. e. a metallic box.

The resulting current-voltage characteristics at 4 K are shown in fig. 3.18 (a) for the green and blue color-coded wires, respectively. The specific curve shape strongly depends on the processes which are responsible for the flowing current and can show both ohmic and diode-like contributions. At 4 K the leakage currents have values of no more than 150 pA for back gate voltages of up to 20 V , while at room temperature they are one to two orders of magnitude larger.

Transport measurements through MoS₂ flakes. Electrical transport measurements through the contacted MoS₂ flakes were performed using a similar circuit that is depicted in fig. 3.17. It functions in a way analogous to the previously discussed setup in fig. 3.16 apart from the additional Yokogawa 7651 voltage source used to apply source-drain voltages. However, for gate voltages exceeding 20 V the Keithley 2002 multimeter changes its

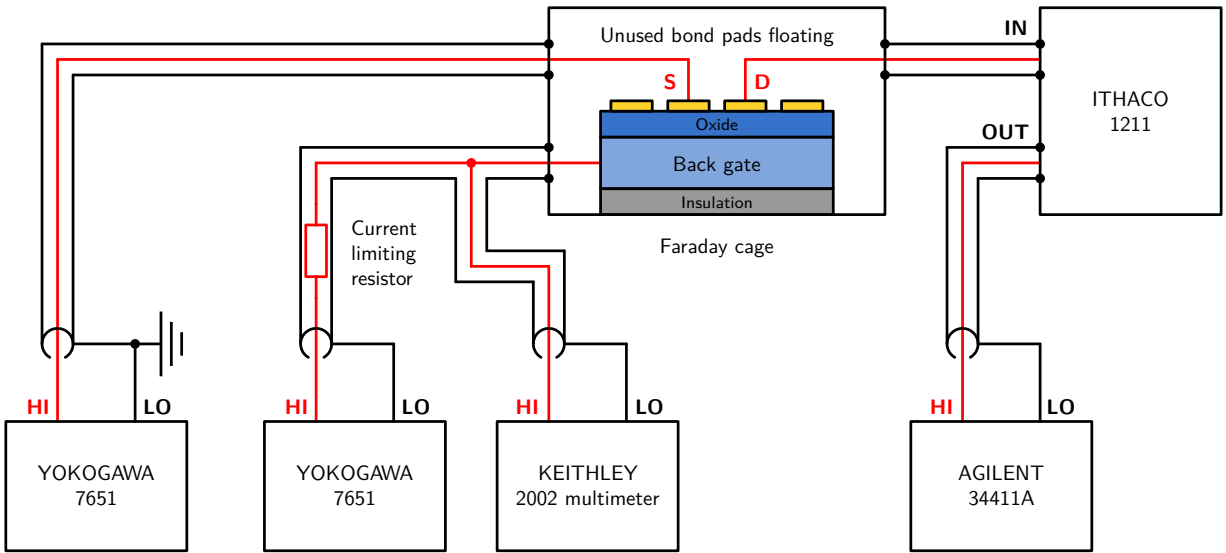


Figure 3.17.: Circuit used for electrical transport measurements through MoS_2 flakes. Varying voltages were applied to the back gate and the source electrode with two Yokogawa 7651 voltage sources using a current limiting resistor of $1\text{ G}\Omega$ at the back gate to avoid sample damage. A Keithley 2002 multimeter was employed to measure the back gate voltage, since unlike other multimeters it offers an input resist of $100\text{ G}\Omega$ and is therefore suitable for use in circuits featuring gigaohm resistances. For back gate voltages exceeding 20 V , however, the Keithley 2002 multimeter can only be used with reduced input resistor such that the current limiting resistor needs to be dispensed with. The transport current from source to drain was measured using an Ithaco 1211 current-voltage converter together with an Agilent 34411A multimeter. Unused bond pads were unplugged leaving their corresponding electric potentials floating, i. e. undefined in order to avoid leakage currents involving these pads. The whole setup was shielded to prevent inductive currents. For this purpose coaxial cables have been used exclusively, while the sample itself was stored in a Faraday cage, i. e. a metallic box.

measurement range and thereby the input resistor, so that the current limiting resistor of $1\text{ G}\Omega$ can no longer be used.

Since from previous measurements it was already known that the leakage currents at 4 K are clearly below 1 nA , the current limiting resistor and the Keithley 2002 multimeter were omitted in order to use the full available voltage range from -32 V to $+32\text{ V}$ of the Yokogawa 7651 voltage source connected to the back gate. At room temperature, however, this would most likely damage the sample.

The measured source-drain current I_{SD} using the blue and green color-coded wires as source and drain, respectively, is shown in fig. 3.18 (b) as function of the gate voltage U_G and the source-drain voltage U_{SD} . In order to suppress the measurement background caused by leakage currents, for each fixed value of the back gate voltage the current averaged over all values of the source-drain voltage was subtracted from the signal.

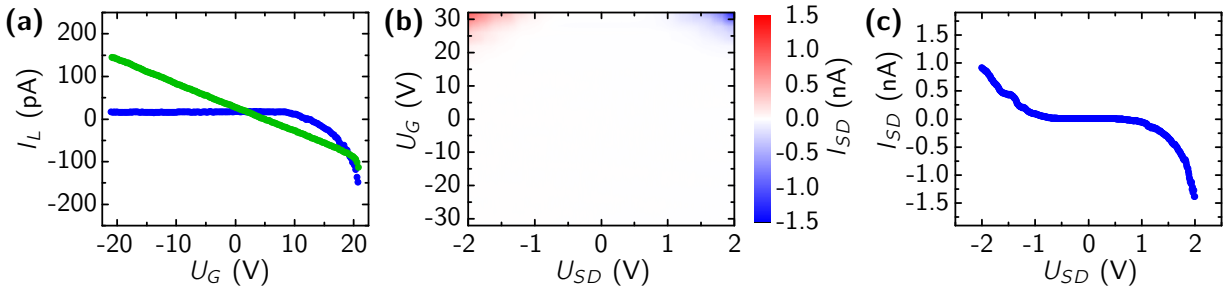


Figure 3.18.: Results of electrical transport measurements at 4 K. **(a)** Leakage current I_L from the back gate through 100 nm of silicon oxide to the green and blue color-coded wires, respectively, as a function of the back gate voltage U_G . Measured using the circuit shown in fig. 3.16. **(b)** Source-drain current I_{SD} as function of the back gate voltage U_G and the source-drain voltage U_{SD} using the blue and green color-coded wires as source and drain, respectively. Measured using the circuit from fig. 3.17. The background caused by leakage currents was removed by subtracting the current averaged over all source-drain voltages for each fixed value of the back gate voltage. **(c)** Source-drain current I_{SD} as function of source-drain voltage U_{SD} for a fixed back gate voltage of $U_G = 32$ V using the blue and green color-coded wires as source and drain, respectively. Measured using the circuit from fig. 3.17. The background caused by the leakage currents was removed by subtracting the current averaged over all source-drain voltages.

While for most values of the gate voltage virtually no source-drain current is measured, at larger positive gate voltages transport through the MoS₂ flake can clearly be observed with an onset at roughly $U_G = 20$ V and growing current for higher gate voltage. The presence of source-drain current only for positive gate voltage above a certain threshold is in good agreement with previously reported experiments [49].

Fig. 3.18 (c) shows the recorded source-drain current I_{SD} at a back gate voltage of $U_G = 32$ V as a function of the source-drain voltage U_{SD} in detail. Again the current averaged over all values of the source-drain voltage U_{SD} was subtracted to suppress measurement background. The observed values of up to 1.5 nA are by one order of magnitude larger than all leakage currents, which is a clear indication that the measured current actually flows *through* the MoS₂ flake and does not take any other path.

The current-voltage characteristic is diode-like, which is plausible, since the contact of the gold wires to the MoS₂ flake is a metal-semiconductor junction with an expected Schottky barrier [57, 58]. It has been reported that this contact can be turned into an ohmic one by performing thermal annealing with the sample [49]. For the purpose of tuning the charge carrier density in the MoS₂ flake by the application of an external voltage, however, the specific type of the current-voltage characteristics is insignificant, as long as it is guaranteed that charge carriers can flow to or from the flake.

The measurements presented here show that the chosen approach to contact selected MoS₂ flakes using the method of laser lithography is indeed suitable for the purpose of tuning the charge carrier density. Some caution has to be taken with regard to leakage currents,

which, however, can be corrected for by characterization measurements and an appropriate insulation of the sample. Bearing this in mind, further experiments on monolayer MoS₂ crystals with well-defined Fermi potential are within reach.

3.3. Experimental results

First promising results of experiments combining optical and electronic methods are presented in this section. To this end PL measurements with the MoS₂ flake contacted by the red and orange color-coded wires (cf. fig. 3.7) were performed for different back gate voltages in order to observe a change in the PL spectra due to a changed excess of neutral excitons and charged trions (cf. section 3.2.1).

Fig. 3.19(a) shows a waterfall plot of three PL spectra for the A exciton recorded at -30 V , 0 V and $+30\text{ V}$ in light color. The spectra for 0 V and $+30\text{ V}$ are shifted by 250 cts and 500 cts, respectively, with respect to the spectrum for -30 V for clarity. In order to determine the relative contribution of the neutral A exciton and the negative A⁻ trion the sum of two Lorentzians (dark solid lines) is fitted to the measurement data [37]. Dashed lines indicate the wave lengths with maximum intensity.

Owing to this fitting procedure the two overlapping emission peaks of the A exciton and the A⁻ trion can be separated as demonstrated in fig. 3.19(b) for the spectrum obtained at $+30\text{ V}$ back gate voltage. The two gray Lorentz curves representing the A and A⁻ peak,

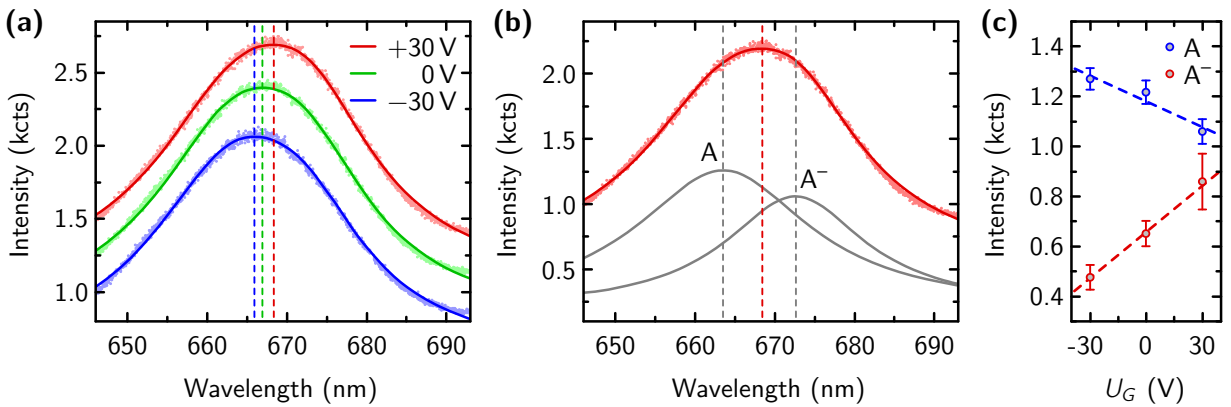


Figure 3.19.: PL measurements for different back gate voltages at 15 min integration time. **(a)** Waterfall plot of PL spectra of the A exciton at -30 V , 0 V and $+30\text{ V}$ (light colors) with double Lorentzian fits (dark solid lines). The spectra for 0 V and $+30\text{ V}$ are shifted by 250 cts and 500 cts, respectively, with respect to the spectrum for -30 V for clarity. **(b)** PL spectrum for $+30\text{ V}$ (light red) with two Lorentz curves (gray) representing the emission peaks of the A exciton and the A⁻ trion. The sum of the two Lorentz curves (dark red) agrees excellently with the data. **(c)** Peak intensities of the Lorentz curves representing the emission of the A exciton and the A⁻ trion, respectively. The dashed lines show the best linear fit as guide to the eye.

respectively, in sum yield the dark red double Lorentzian curve, which is in excellent agreement with the measured data (light red points).

In order to increase the accuracy of the fitting procedure, the same center wavelengths for the two peaks are used for all three back gate voltages. These center wavelengths are found to be (663.5 ± 0.3) nm ((1.869 ± 0.001) eV) for the A exciton and (672.6 ± 0.2) nm ((1.843 ± 0.001) eV) for the A⁻ trion. These values correspond to an exciton binding energy of 51 meV and a trion binding energy of 26 meV. The binding energies are slightly different from those obtained in section 3.1.2, clearly showing the influence of the dielectric environment, which is changed for this measurement by the presence of the gold wires.

The maximum intensities of the fits to the A and A⁻ emission as a function of the back gate voltage are presented in fig. 3.19(c) and a clear dependence of the relative peak height on the back gate voltage can be observed. As expected, the signal of the A⁻ trions is highest for positive gate voltages (cf. section 3.2.1). The linear fit from fig. 3.19(c) reveals a peak amplitude shift with the back gate voltage relative to the peak amplitude at back gate voltage 0 V of $-0.28\%/\text{V}$ for the neutral A exciton and of $+0.95\%/\text{V}$ for the A⁻ trion. Interestingly, the emission intensity of the neutral A exciton does not decrease by the same amount as the A⁻ emission increases, so that the total PL intensity is highest for a back gate voltage of +30 V. Such shifts in the total emission intensity have also been observed in previous experiments [37].

The obtained value for the energy separation between A exciton and A⁻ trion as well as the relative PL intensity shift are comparable to results found in literature [37], even though minor differences can be observed. These differences, however, are readily to be explained by the dielectric environment of the illuminated MoS₂ flake, which causes a shift in exciton and trion binding energies and thereby in the PL spectra. Hence, the presented experimental results show clear evidence for the functionality of the desired charge carrier density tuning by application of a back gate voltage.

Chapter 4.

Summary and outlook

The aim of this work was the fabrication and characterization of a sample, which allows for control of both optical and electronic properties of monolayer MoS₂ flakes. To achieve this goal a combination of cryogenic confocal microscopy and laser lithographic gate patterning was employed.

Regarding cryogenic confocal microscopy, a strong expertise was already present in the research group from a long history of experiments going back to first fiber-based approaches [25]. Hence, setting up an experimental environment for optical excitation of monolayer MoS₂ and spectral as well as polarization resolved analysis of resulting PL at cryogenic temperatures was a routine task. In particular, large parts of existing systems could be reused.

PL measurements with this setup demonstrated a variety of theoretically described optical properties of monolayer MoS₂. The spectral behavior shows two pronounced resonances that correspond to the A and B excitons, which are due to optically active transitions from the conduction band to the respective valence subband. Both valley circular dichroism and valley coherence have been observed.

More effort was required for all steps related to electronics. In particular the ProtoLaser LDI system had not been used before due to its novelty. Consequently, a long list of preparations was necessary for finding a stable working point, which allowed to exploit the benefits of laser lithography. Specifically, a suitable combination of photoresist, lift-off resist, illumination and development parameters as well as a wire layout design had to be found.

Special care was taken to avoid negative effects of photoresist edge beads, which are inevitable on spin-coated millimeter-sized samples. For this purpose a graded wire layout design was employed, which both ensured sufficient illumination in regions with a thick photoresist layer and avoided unwanted overexposure. Having found an appropriate set of parameters a high reproducibility could be achieved.

The built-in microscope camera of the ProtoLaser LDI system allowed precise alignment of the wire layout, which had previously been defined with the help of a high resolution optical image of the sample, with respect to the MoS₂ flakes of interest. Consequently, a highly adapted design was possible without the need for photo mask generation or time-consuming e-beam lithography.

After deposition of gold wires in a UHV e-beam evaporator the sample was electrically contacted in two steps. First, a method of local doping was employed to obtain connections to the highly boron doped silicon substrate, which showed ohmic current-voltage characteristics. Second, connections between bond pads on the sample and copper soldering pads on the sample holder were established for contacting the MoS₂ flakes of interest.

After completion of the sample preparation the quality of all these contacts was tested both in ambient conditions and at cryogenic temperatures. Leakage currents were characterized and considered for future experiments. In particular, successful transport measurements through selected MoS₂ flakes verified the functionality of the desired electrical contacts.

The outlined preparation procedure resulted in FET like structures that allowed tuning of the Fermi level in the MoS₂ flakes. Hence, depending on the applied voltage an excess of electrons or holes could be achieved, which in turn favored the formation of neutral excitons or trions as verified by PL experiments.

First experimental results showed a shift of PL resonances depending on the applied back gate voltage. By fitting a double Lorentzian curve to the emission profile two different resonances corresponding to the A exciton and the A⁻ trion could be separated. The relative change in intensity of these peaks is in accordance with the expected excess of charge carriers for different back gate voltages.

Ultimately, the sample showed the desired properties that offer control over both electronic and optical parameters. Against this background the methods discussed here make accessible a whole plethora of further experiments. By the use of cryogenic confocal microscopy, tuning of the Fermi level together with optical excitation can easily be combined with the variation of further quantities, e. g. by application of a magnetic field or a change in temperature. Hence, a huge parameter space opens up that is accessible for a large range of the charge carrier density in monolayer MoS₂, which can be used to tailor its material properties in order to emphasize whichever effect is to be studied. Taking into account the rich physics of MoS₂ further exciting experimental results are to be expected.

Also, as discussed in the appendix, improvements to the methods presented in this work are possible. The choice of a different photoresist and a different lift-off resist promises simplifications for all lithography-related steps, while thermal annealing has been reported to enhance the quality of the electric contacts between gold wires and MoS₂ flakes. Moreover, a different strategy in mounting the sample by using chip carriers could result in a simplified bond process and better electric insulation. Finally, the use of a SIL can improve the light collection efficiency of the confocal microscope and thereby improve the quality of the optical signal.

With all these results and prospects in mind, the electrical properties of monolayer MoS₂ flakes can easily be controlled as routinely as the optics of a cryogenic confocal microscope. The main purpose of this work can thus be seen as to serve as a starting point to reach more advanced experiments without much effort. The experimental results from section 3.3 stress that this goal has been reached.

Appendix A.

Suggested modifications for future samples

While working on the sample preparation sketched in section 3.2 several difficulties arose that required particular attention. In all cases satisfying solutions have been found and the obtained sample fulfills the desired requirements. Still, minor modifications in the preparation procedure are worth considering when preparing future samples. The possible advantages and drawbacks of these alternatives are briefly summarized in this chapter.

A.1. Photoresist and lift-off resist

The combination of the photoresist S1813 and the lift-off resist LOR 3B is a powerful tool for obtaining lithographic structures of high quality and reproducibility. However, several process parameters most likely have to be reevaluated when preparing a new sample, since LOR 3B degrades chemically rather quickly.

Within a matter of few months the development time needed for a photoresist undercut of optimum depth can change notably. In addition, the viscosity of LOR 3B changes due to slowly evaporating solvents, thereby causing a change in the thickness of the spin coated layer on the sample. Due to interference effects of the illuminating laser of the ProtoLaser LDI system with its back reflection, however, this requires the illumination dose for the S1813 photoresist to be adapted.

The only purpose of the large illumination doses reported in section 3.2 of up to 1500 mJ/cm^2 in regions 1 and 2 as defined in table 3.1 is to ensure sufficient illumination also in the presence of photoresist edge beads. Since the width of the structures distant from the sample edge coincides well with the designed width, however, it can be concluded that the much lower doses in region 3 are sufficient for proper illumination of S1813.

Hence, for a layer of S1813 on top of a layer of LOR 3B doses ranging between 5 mJ/cm^2 and 20 mJ/cm^2 can be considered suitable. Previous tests using only S1813 and no LOR 3B,

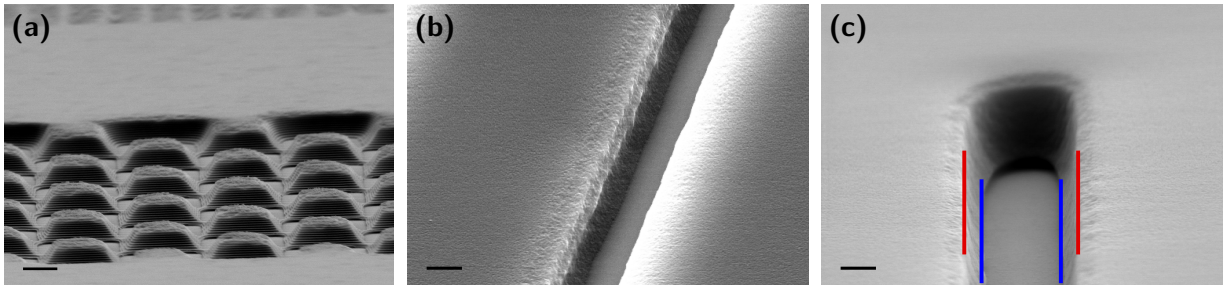


Figure A.1.: SEM images of photoresist edges for different lithographic structures created with the ProtoLaser LDI system. **(a)** Chessboard-like structure written into S1813 with the fine tool using an illumination dose of 200 mJ/cm^2 and a spot spacing of $0.1 \mu\text{m}$. Nonvertical photoresist edges featuring interference patterns are clearly visible. Scale bar is $2 \mu\text{m}$. **(b)** Narrow line written into AZ MiR 701 with the fine tool using an illumination dose of 225 mJ/cm^2 and a spot spacing of $0.1 \mu\text{m}$. Photoresist edges are much steeper than for S1813. Scale bar is 500 nm . **(c)** Narrowest possible single-pixel line written into AZ MiR 701 with the fine tool using an illumination dose of 1800 mJ/cm^2 and a spot spacing of $0.1 \mu\text{m}$. Distance between red lines at top of photoresist layer is $1.08 \mu\text{m}$, while distance between blue lines at bottom of photoresist layer is 753 nm . Scale bar is 250 nm .

however, have proven higher doses of about 250 mJ/cm^2 to 350 mJ/cm^2 to be necessary. Judging from this difference by almost two orders of magnitude, a strong dependence on the layer thickness of LOR 3B has to be expected.

These two effects, of course, conflict with the desire to determine operational parameters once and to reproduce previous results without the need to revise the whole process. However, the use of LOR 3B is indispensable when working with S1813 despite these difficulties. As fig. A.1 (a) shows, the photoresist edges are not vertical and show interference patterns, which makes the use of a lift-off resist necessary to obtain good results after lift-off.

An alternative approach is the application of a different photoresist that makes the use of a lift-off resist unnecessary. Promising results have been obtained using AZ MiR 701 photoresist, which shows much steeper edges without any interference patterns (cf. fig. A.1 (b)). A comparison of the width at the top and at the bottom of a test structure written into AZ MiR 701 can be found in fig. A.1 (c).

An additional advantage of AZ MiR 701 photoresist is the smaller viscosity compared to S1813 photoresist [40, 59], which leads to a thinner layer when spin coating it onto a sample. Hence, also the edge beads are expected to be smaller than for S1813, which reduces difficulties arising from inhomogeneous photoresist thickness.

A.2. Thermal annealing

As discussed in section 3.2.4 a Schottky barrier forms at the electric contacts between MoS₂ flakes and lithographically created gold wires. For similar devices a contact resistance reduction by a factor of 10 by thermal annealing in a vacuum tube furnace at a temperature of 200 °C with an Ar flow of 100 sccm and a H₂ flow of 10 sccm for two hours has been reported [49].

According to [27] the process of annealing in a argon/hydrogen atmosphere is furthermore able to remove a thin film of photoresist residue, which has been found on similar samples even after lift-off. Such a film might indeed be present on the sample used for this work and responsible for small bumps observed both on MoS₂ flakes and the silicon substrate (cf. fig. 3.12 (a)).

As a result, thermal annealing is very likely to improve the contact quality between MoS₂ flakes and gold wires. In addition it is expected to increase both surface and optical quality of the sample by removing photoresist residues.

A.3. Sample mounting

The contacted sample is recommended not to be mounted directly onto metallic sample holders, since leakage currents from the back gate are to be expected otherwise (cf. section 3.2.4). A very simple way to avoid this problem is to fix the sample to the sample holder by applying glue to the whole surface underneath the back gate and to make sure that no gold beads (cf. section 3.2.3) protrude below this surface. The insulating glue is expected to be sufficient to rule out any leakage currents between back gate and sample holder.

Alternatively, the sample holder itself could be replaced by a ceramic chip carrier that is insulating by itself. An additional advantage of this step would be the simultaneous simplification of the bond process for contacting the sample. Chip carriers usually come with gold bond pads connected to soldering lugs via a suitable socket.

The use of these bond pads and soldering lugs would remove the need for the currently used soldering pads made from galvanically deposited copper on a thin polyimide foil. Since establishing stable bond connections to these copper pads is quite challenging, this step would mean a major simplification of the bond process. At the same time, however, it would require a substantial redesign of the way the sample is mounted inside the cryostat.

Appendix B.

Theoretical description of solid immersion lenses

According to the Rayleigh criterion [51] the optical resolution of a microscope is limited by $0.61\lambda/\text{NA}$, where λ is the wavelength and NA is the numerical aperture of the objective. A standard approach to obtain better resolution therefore is to increase the numerical aperture of the objective in use.

When dealing with cryogenic confocal microscopy the successful use of SILs has been reported for this purpose [34], i. e. of a lens with one strongly curved spherical surface and one flat surface, usually made from a material with high refractive index. Due to operation beyond paraxial approximation a SIL acts as numerical aperture increasing lens (NAIL) and is thus able to increase optical resolution.

To avoid chromatic aberrations a hemispherical SIL is often preferred over the Weierstrauss configuration, although the latter offers a higher resolution increase [16]. For a hemispherical SIL the focal point lies at the center of the sphere and all light rays are perpendicular to the spherical surface. Hence, no diffraction occurs and chromatic aberrations are excluded by principle.

For the detection of PL, however, another property of SILs with high refractive indices is remarkable, namely the observation that a dipole in the vicinity of a phase boundary emits most power into the medium with higher refractive index [35]. Hence, a SIL can also serve the purpose to collect more PL photons. In order to understand this effect in more detail, a theoretical description is presented here, which is in good accordance with comparable experimental results from [35].

B.1. Dipole fields at planar phase boundaries

When a dipole emitter is placed near a phase boundary with a distance comparable to the wavelength of the emitted light, the radiation profile can take an unexpected form due

to near-field effects. To quantify such effects a solution of the Maxwell equations in an appropriate geometry (cf. fig. B.1) is presented, closely following calculations from [13, 23] but extending them to more generality.

B.1.1. Expansion of the dipole field in plane waves

Consider a dipole located at the origin (in particular at $z = 0$) with an orientation given by the polar angle θ and the azimuthal angle φ corresponding to the dipole moment $\boldsymbol{\mu}$. In order to calculate the interaction of the dipole field with a number of plane phase boundaries orthogonal to the z -axis, it is Fourier expanded into plane waves. In [13] a solution of the Maxwell equations using the current density of a point dipole results in the following Fourier representation of an electric dipole field:

$$\begin{aligned}\mathbf{E}(\mathbf{r}_0) &= -\frac{1}{\pi\epsilon_m} \int d^2k_r \exp(i\mathbf{k}_r \cdot \boldsymbol{\rho}_0) \left[\delta(z_0) \cdot (\boldsymbol{\mu} \cdot \hat{\mathbf{z}}) \cdot \hat{\mathbf{z}} + \frac{i}{2q_m} \exp(iq_m|z_0|) \cdot \mathbf{k}_m^\pm \times (\mathbf{k}_m^\pm \times \boldsymbol{\mu}) \right] \\ &=: \frac{i}{2\pi\epsilon_m} \int d^2k_r \boldsymbol{\xi}_{\text{inc}}^\pm(\mathbf{k}_r)\end{aligned}$$

Here, $\mathbf{r}_0 = \boldsymbol{\rho}_0 + z_0\hat{\mathbf{z}}$ and $\mathbf{k} = \mathbf{k}_r + k_z\hat{\mathbf{z}}$ are observation point and wave vector in cylindrical coordinates, $\epsilon_m = n_m^2$ is the dielectric constant of the medium in which the dipole resides, $q_m = \sqrt{k_m^2 - k_r^2}$ with $k_m = \omega n_m / c$ such that $\text{Im } q_m \geq 0$ and finally

$$\mathbf{k}_m^\pm = \mathbf{k}_r \pm q_m\hat{\mathbf{z}} = \mathbf{k}_r + \text{sign } z_0 \cdot q_m\hat{\mathbf{z}}.$$

Hence, $\boldsymbol{\xi}_{\text{inc}}^+(\mathbf{k}_r)$ and $\boldsymbol{\xi}_{\text{inc}}^-(\mathbf{k}_r)$ are the plane wave Fourier components of the dipole field emitted into the half-space $z > 0$ and the half-space $z < 0$, respectively.

Using this representation, the effect of plane phase boundaries in the vicinity of the dipole can be investigated. The geometry is sketched in fig. B.1: $M - 1$ planes at positions $z_1 > z_2 > \dots > z_{M-1}$ orthogonal to the z -axis separate the environment in M regions with refractive indices n_1, \dots, n_M . The dipole resides at position $z = 0$ in region m with refractive index n_m .

The planar field components $\boldsymbol{\xi}_{\text{inc}}^+(\mathbf{k}_r)$ and $\boldsymbol{\xi}_{\text{inc}}^-(\mathbf{k}_r)$ emitted in positive and negative z -direction, respectively, propagate in the different regions according to the refraction formulas given by Snell's law. In region $i \neq m$ four field components are distinguished. The two components $\boldsymbol{\xi}_{\uparrow,i}^\pm(\mathbf{k}_r)$ propagate in positive z -direction, while the two components $\boldsymbol{\xi}_{\downarrow,i}^\pm(\mathbf{k}_r)$ propagate in negative z -direction. The superscript \pm indicates whether the corresponding field component originates from $\boldsymbol{\xi}_{\text{inc}}^+(\mathbf{k}_r)$ or $\boldsymbol{\xi}_{\text{inc}}^-(\mathbf{k}_r)$ by (repeated) reflection or transmission.

The electric field in region $i \neq m$ can again be written in terms of the Fourier transform of the plane wave components $\boldsymbol{\xi}_{\uparrow\downarrow,i}^\pm(\mathbf{k}_r)$. Splitting the integration variable in an angular and a radial part by writing $d^2k_r = d\gamma dk_r k_r$, the following expression is obtained:

$$\mathbf{E}_i(\mathbf{r}) = \frac{i}{2\pi\epsilon_m} \int_0^{2\pi} d\gamma \int_0^\infty dk_r k_r [\boldsymbol{\xi}_{\uparrow,i}^+(\mathbf{k}_r) + \boldsymbol{\xi}_{\uparrow,i}^-(\mathbf{k}_r) + \boldsymbol{\xi}_{\downarrow,i}^+(\mathbf{k}_r) + \boldsymbol{\xi}_{\downarrow,i}^-(\mathbf{k}_r)] \quad (*)$$

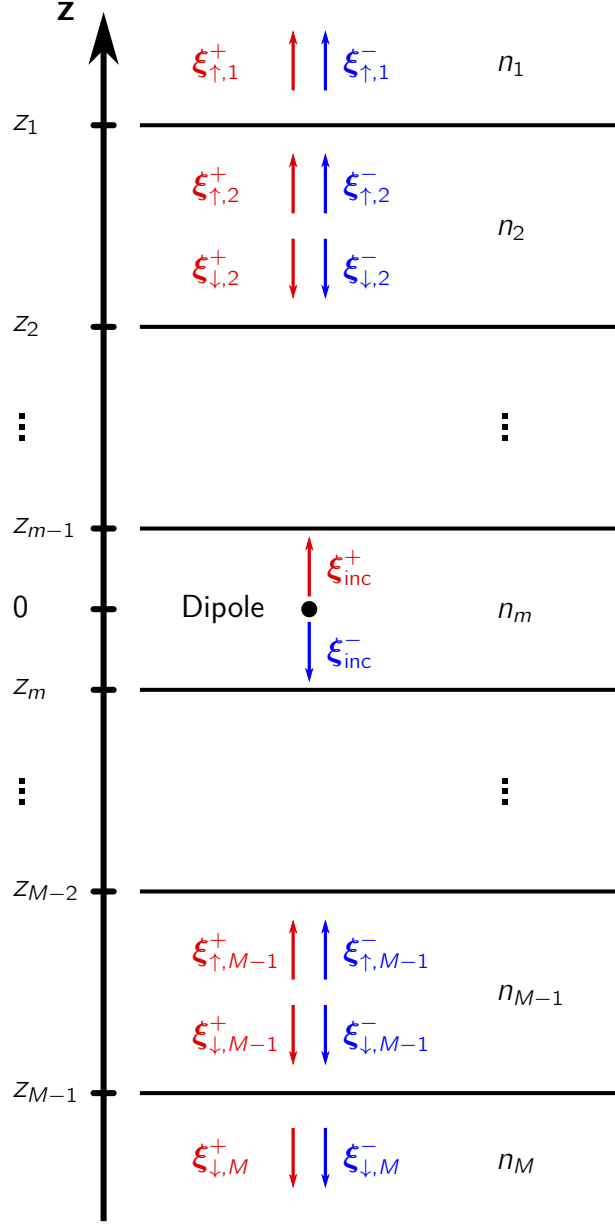


Figure B.1.: Sketch of the geometry used to describe a radiating dipole near a number of planar phase boundaries. $M - 1$ planes at positions $z_1 > z_2 > \dots > z_{M-1}$ orthogonal to the z -axis separate the environment in M regions with refractive indices n_1, \dots, n_M . The dipole resides at position $z = 0$ in region m with refractive index n_m . The dipole emits plane wave field components $\xi_{\text{inc}}^+(\mathbf{k}_r)$ in positive and $\xi_{\text{inc}}^-(\mathbf{k}_r)$ in negative z -direction, which propagate in the different regions according to the refraction formulas given by Snell's law. In region $i \neq m$ four field components are distinguished. The two components $\xi_{\pm,i}^+(\mathbf{k}_r)$ propagate in positive z -direction, while the two components $\xi_{\pm,i}^-(\mathbf{k}_r)$ propagate in negative z -direction. The superscript \pm indicates whether the corresponding field component originates from $\xi_{\text{inc}}^+(\mathbf{k}_r)$ or $\xi_{\text{inc}}^-(\mathbf{k}_r)$.

In region m an additional integrand $\xi_{\text{inc}}^{\pm}(\mathbf{k}_r)$ for the field directly emitted from the dipole has to be included. In order to proceed, different projections of the vector quantities $\xi_{\uparrow\downarrow,i}^{\pm}(\mathbf{k}_r)$ are considered separately.

B.1.2. Orthogonal decomposition of plane wave components

In order to understand transmission and reflection at the individual phase boundaries of the plane wave components $\xi_{\uparrow\downarrow,i}^{\pm}(\mathbf{k}_r)$, these vector quantities are decomposed in an appropriate orthonormal basis. To this end, the three vectors $\hat{\mathbf{z}}$, $\hat{\mathbf{k}}_r$ and $\hat{\mathbf{z}} \times \hat{\mathbf{k}}_r$ are considered, which are orthogonal and normal as desired. Using

$$\boldsymbol{\mu} = [\boldsymbol{\mu} \cdot \hat{\mathbf{z}}] \hat{\mathbf{z}} + [\boldsymbol{\mu} \cdot \hat{\mathbf{k}}_r] \hat{\mathbf{k}}_r + [\boldsymbol{\mu} \cdot (\hat{\mathbf{z}} \times \hat{\mathbf{k}}_r)] (\hat{\mathbf{z}} \times \hat{\mathbf{k}}_r)$$

and

$$\mathbf{a} \times (\mathbf{b} \times \mathbf{c}) = \mathbf{b}[\mathbf{a} \cdot \mathbf{c}] - \mathbf{c}[\mathbf{a} \cdot \mathbf{b}]$$

one obtains

$$-\mathbf{k}_m^{\pm} \times (\mathbf{k}_m^{\pm} \times \boldsymbol{\mu}) = [(k_r \hat{\mathbf{z}} \mp q_m \hat{\mathbf{k}}_r) \cdot \boldsymbol{\mu}] (k_r \hat{\mathbf{z}} \mp q_m \hat{\mathbf{k}}_r) + k_m^2 [(\hat{\mathbf{z}} \times \hat{\mathbf{k}}_r) \cdot \boldsymbol{\mu}] (\hat{\mathbf{z}} \times \hat{\mathbf{k}}_r),$$

where the result for \mathbf{k}_m^- has already been given in [23]. It is also helpful to consider single components of $\boldsymbol{\mu}$, for which a second orthonormal basis is introduced.

Each observation point given by $\mathbf{r}_0 = \boldsymbol{\rho}_0 + z_0 \hat{\mathbf{z}}$ defines a *plane of observation* together with the z -axis [23]. The unit vector $\hat{\mathbf{p}}$ is defined to lie in the plane of observation but perpendicular to the z -axis (i.e. parallel to the phase boundaries), while the unit vector $\hat{\mathbf{s}}$ is defined to be perpendicular to the plane of observation (i.e. perpendicular to the z -axis and parallel to the phase boundaries). Together with $\hat{\mathbf{z}}$ the two unit vectors $\hat{\mathbf{p}}$ and $\hat{\mathbf{s}}$ form an orthonormal basis.

In the following, only the three special cases $\boldsymbol{\mu} = \mu \hat{\mathbf{p}}$, $\boldsymbol{\mu} = \mu \hat{\mathbf{s}}$ and $\boldsymbol{\mu} = \mu \hat{\mathbf{z}}$ are considered. The general situation for arbitrary $\boldsymbol{\mu}$ can be obtained by superposition of the solutions for these special cases. The expressions for ξ_{inc}^{\pm} can be simplified for the three cases separately.

Case 1: $\boldsymbol{\mu} = \mu \hat{\mathbf{p}}$

$$\begin{aligned} \boldsymbol{\mu} \cdot \hat{\mathbf{z}} &= 0 \\ \boldsymbol{\mu} \cdot \hat{\mathbf{k}}_r &= \mu \cos \gamma \\ \boldsymbol{\mu} \cdot (\hat{\mathbf{z}} \times \hat{\mathbf{k}}_r) &= -\mu \sin \gamma \end{aligned}$$

$$\Rightarrow \quad \xi_{\text{inc}}^{+} = A \left[-\cos \gamma (k_r \hat{\mathbf{z}} - q_m \hat{\mathbf{k}}_r) - \sin \gamma \frac{k_m^2}{q_m} (\hat{\mathbf{z}} \times \hat{\mathbf{k}}_r) \right] \exp(i q_m z_0)$$

$$\xi_{\text{inc}}^{-} = A \left[\cos \gamma (k_r \hat{\mathbf{z}} + q_m \hat{\mathbf{k}}_r) - \sin \gamma \frac{k_m^2}{q_m} (\hat{\mathbf{z}} \times \hat{\mathbf{k}}_r) \right] \exp(-i q_m z_0)$$

Case 2: $\mu = \mu \hat{\mathbf{s}}$

$$\begin{aligned} \boldsymbol{\mu} \cdot \hat{\mathbf{z}} &= 0 \\ \boldsymbol{\mu} \cdot \hat{\mathbf{k}}_r &= \mu \sin \gamma \\ \boldsymbol{\mu} \cdot (\hat{\mathbf{z}} \times \hat{\mathbf{k}}_r) &= \mu \cos \gamma \\ \Rightarrow \quad \boldsymbol{\xi}_{\text{inc}}^+ &= A \left[-\sin \gamma (k_r \hat{\mathbf{z}} - q_m \hat{\mathbf{k}}_r) + \cos \gamma \frac{k_m^2}{q_m} (\hat{\mathbf{z}} \times \hat{\mathbf{k}}_r) \right] \exp(i q_m z_0) \\ \boldsymbol{\xi}_{\text{inc}}^- &= A \left[\sin \gamma (k_r \hat{\mathbf{z}} + q_m \hat{\mathbf{k}}_r) + \cos \gamma \frac{k_m^2}{q_m} (\hat{\mathbf{z}} \times \hat{\mathbf{k}}_r) \right] \exp(-i q_m z_0) \end{aligned}$$

Case 3: $\mu = \mu \hat{\mathbf{z}}$

$$\begin{aligned} \boldsymbol{\mu} \cdot \hat{\mathbf{z}} &= \mu \\ \boldsymbol{\mu} \cdot \hat{\mathbf{k}}_r &= 0 \\ \boldsymbol{\mu} \cdot (\hat{\mathbf{z}} \times \hat{\mathbf{k}}_r) &= 0 \\ \Rightarrow \quad \boldsymbol{\xi}_{\text{inc}}^+ &= A \frac{k_r}{q_m} (k_r \hat{\mathbf{z}} - q_m \hat{\mathbf{k}}_r) \exp(i q_m z_0) \\ \boldsymbol{\xi}_{\text{inc}}^- &= A \frac{k_r}{q_m} (k_r \hat{\mathbf{z}} + q_m \hat{\mathbf{k}}_r) \exp(-i q_m z_0) \end{aligned}$$

As above the variable $q_m = \sqrt{k_m^2 - k_r^2}$ with $k_m = \omega n_m / c$ such that $\text{Im } q_m \geq 0$ has been used. The factors $A = \mu \exp(i \mathbf{k}_r \cdot \boldsymbol{\rho}_0)$ and $\exp(\pm i q_m z_0)$ account for the phase shift of the wave traveling from the dipole at the origin to the observation point $\mathbf{r}_0 = \boldsymbol{\rho}_0 + z_0 \hat{\mathbf{z}}$.

B.1.3. Reflection and transmission of plane waves

Consider a generic electric plane wave field component $\boldsymbol{\xi}_{\text{inc}}$ that is split in components with respect to the previously defined orthonormal basis given by $\hat{\mathbf{z}}, \hat{\mathbf{k}}_r$ and $\hat{\mathbf{z}} \times \hat{\mathbf{k}}_r$:

$$\boldsymbol{\xi}_{\text{inc}} = \xi_z \hat{\mathbf{z}} + \xi_r \hat{\mathbf{k}}_r + \xi_{\times} (\hat{\mathbf{z}} \times \hat{\mathbf{k}}_r)$$

When describing reflection of this plane wave off a surface orthogonal to the z -axis in terms of the Fresnel reflection coefficients r^p and r^s for parallel and perpendicular polarization [79, pp. 33–42], respectively, special care has to be taken to account for the simultaneous change of polarization. Throughout this calculation the following sign convention is used:

$$\boldsymbol{\xi}_{\text{ref}} = r^p \xi_z \hat{\mathbf{z}} - r^p \xi_r \hat{\mathbf{k}}_r + r^s \xi_{\times} (\hat{\mathbf{z}} \times \hat{\mathbf{k}}_r)$$

For the transmitted wave no such change in sign is necessary, so that it is formally possible to write

$$\boldsymbol{\xi}_{\text{trans}} = t^p \xi_z \hat{\mathbf{z}} + t^p \xi_r \hat{\mathbf{k}}_r + t^s \xi_{\times} (\hat{\mathbf{z}} \times \hat{\mathbf{k}}_r)$$

However, a potential dependence of ξ_z , ξ_r and ξ_x on the refractive index has to be respected, when the wave passes the phase boundary. In particular, a relative change of the three amplitudes ξ_z , ξ_r and ξ_x is responsible for the “change of direction” due to refraction. Especially, the replacement

$$(k_r \hat{\mathbf{z}} + q_i \hat{\mathbf{k}}_r) \rightarrow \left(\frac{\varepsilon_i}{\varepsilon_j} \right)^{1/2} (k_r \hat{\mathbf{z}} + q_j \hat{\mathbf{k}}_r)$$

is necessary in the following calculations, since q_i is dependent on the refractive index n_i of region i . The additional factor $(\varepsilon_i/\varepsilon_j)^{1/2}$ is needed to normalize the two vectors $(k_r \hat{\mathbf{z}} + q_i \hat{\mathbf{k}}_r)$ and $(k_r \hat{\mathbf{z}} + q_j \hat{\mathbf{k}}_r)$ of respective lengths $k_i = \frac{\omega}{c} \sqrt{\varepsilon_i}$ and $k_j = \frac{\omega}{c} \sqrt{\varepsilon_j}$.

For a single phase boundary between two adjacent regions i and $j = i \pm 1$, the reflection and transmission coefficients can be expressed similarly as in [13]. However, the transmission coefficient t^p given there is formulated for the magnetic field, whereas only the electric field is considered here. Including this change results in the following expressions:

$$\begin{aligned} r_{ij}^p(k_r) &= \frac{q_i \varepsilon_j - q_j \varepsilon_i}{q_i \varepsilon_j + q_j \varepsilon_i} & t_{ij}^p(k_r) &= \frac{2q_i \sqrt{\varepsilon_i \varepsilon_j}}{q_i \varepsilon_j + q_j \varepsilon_i} \\ r_{ij}^s(k_r) &= \frac{q_i - q_j}{q_i + q_j} & t_{ij}^s(k_r) &= \frac{2q_i}{q_i + q_j} \end{aligned}$$

More generally, the reflection and transmission coefficients $r_{ij}^{p,s}$ and $t_{ij}^{p,s}$ for arbitrary i and j are defined by the following properties:

1. Plane wave components in regions i and j are connected by the transmission coefficients $t_{ij}^{p,s}$, if and only if their wave vectors have same z -component, same azimuthal angle and satisfy $k_i/k_j = n_i/n_j$, i. e. if they behave according to Snell’s law.
2. Plane wave components in regions i and j are connected by the reflection coefficients $r_{ij}^{p,s}$, if and only if their wave vectors have z -components that only differ in sign, have the same azimuthal angle and satisfy $k_i/k_j = n_i/n_j$, i. e. if they behave according to Snell’s law.
3. The coefficients $r_{ij}^{p,s}$ and $t_{ij}^{p,s}$ absorb the complete evolution of the plane waves between first and last reflection at or transmission through a phase boundary. In particular, they account for all phase factors due to propagation in z -direction between the regions i and j and for summation of different light paths depending on which phase boundaries the plane wave was transmitted through and which phase boundaries it was reflected off.

At this point it has to be noted that irrespective of the particular sequence of reflections and transmissions, all plane waves in region i have the same direction of propagation and are thus proportional to $\xi_{\uparrow\downarrow,i}^\pm(\mathbf{k}_r)$, since according to Snell’s law the only relevant input is

the refractive index in region i . This property is essential to absorb the whole evolution between regions i and j into the transmission and reflection coefficients by splitting each contributing term into the vector quantity $\xi_{\uparrow\downarrow,i}^\pm(\mathbf{k}_r)$ and an amplitude.

Closed expressions for $r_{ij}^{p,s}$ and $t_{ij}^{p,s}$ can be written down easily for one or two phase boundaries only. For a higher number of phases, the multitude of different light paths complicates an analytic solution and a numeric evaluation should be preferred. A possible approach is sketched in appendix B.2. However, due to the cylindrical symmetry of the problem, like their two-phase counterparts these generalized reflection and transmission coefficients are only dependent on k_r but not on γ .

With these definitions of $r_{ij}^{p,s}$ and $t_{ij}^{p,s}$ at hand, it is now possible to write down expressions for the plane wave components $\xi_{\uparrow\downarrow,i}^\pm(\mathbf{k}_r)$ in region i again separated for the three different orientations of the dipole moment μ .

Case 1: $\mu = \mu\hat{\mathbf{p}}$

$$\begin{aligned}\xi_{\uparrow,i}^+ &= A \left[-t_{mi}^p \left(\frac{\varepsilon_m}{\varepsilon_i} \right)^{1/2} \cos \gamma (k_r \hat{\mathbf{z}} - q_i \hat{\mathbf{k}}_r) - t_{mi}^s \sin \gamma \frac{k_m^2}{q_m} (\hat{\mathbf{z}} \times \hat{\mathbf{k}}_r) \right] \cdot \\ &\quad \cdot \exp(iq_m z_{m-1}) \exp(iq_i(z_0 - z_i)) \\ \xi_{\downarrow,i}^+ &= A \left[-r_{mi}^p \cos \gamma (k_r \hat{\mathbf{z}} + q_i \hat{\mathbf{k}}_r) - r_{mi}^s \sin \gamma \frac{k_m^2}{q_m} (\hat{\mathbf{z}} \times \hat{\mathbf{k}}_r) \right] \cdot \\ &\quad \cdot \exp(iq_m z_{m-1}) \exp(-iq_i(z_0 - z_{i-1})) \\ \xi_{\uparrow,i}^- &= A \left[r_{mi}^p \cos \gamma (k_r \hat{\mathbf{z}} - q_i \hat{\mathbf{k}}_r) - r_{mi}^s \sin \gamma \frac{k_m^2}{q_m} (\hat{\mathbf{z}} \times \hat{\mathbf{k}}_r) \right] \cdot \\ &\quad \cdot \exp(-iq_m z_m) \exp(iq_i(z_0 - z_i)) \\ \xi_{\downarrow,i}^- &= A \left[t_{mi}^p \left(\frac{\varepsilon_m}{\varepsilon_i} \right)^{1/2} \cos \gamma (k_r \hat{\mathbf{z}} + q_i \hat{\mathbf{k}}_r) - t_{mi}^s \sin \gamma \frac{k_m^2}{q_m} (\hat{\mathbf{z}} \times \hat{\mathbf{k}}_r) \right] \cdot \\ &\quad \cdot \exp(-iq_m z_m) \exp(-iq_i(z_0 - z_{i-1}))\end{aligned}$$

Case 2: $\mu = \mu\hat{\mathbf{s}}$

$$\begin{aligned}\xi_{\uparrow,i}^+ &= A \left[-t_{mi}^p \left(\frac{\varepsilon_m}{\varepsilon_i} \right)^{1/2} \sin \gamma (k_r \hat{\mathbf{z}} - q_i \hat{\mathbf{k}}_r) + t_{mi}^s \cos \gamma \frac{k_m^2}{q_m} (\hat{\mathbf{z}} \times \hat{\mathbf{k}}_r) \right] \cdot \\ &\quad \cdot \exp(iq_m z_{m-1}) \exp(iq_i(z_0 - z_i)) \\ \xi_{\downarrow,i}^+ &= A \left[-r_{mi}^p \sin \gamma (k_r \hat{\mathbf{z}} + q_i \hat{\mathbf{k}}_r) + r_{mi}^s \cos \gamma \frac{k_m^2}{q_m} (\hat{\mathbf{z}} \times \hat{\mathbf{k}}_r) \right] \cdot \\ &\quad \cdot \exp(iq_m z_{m-1}) \exp(-iq_i(z_0 - z_{i-1})) \\ \xi_{\uparrow,i}^- &= A \left[r_{mi}^p \sin \gamma (k_r \hat{\mathbf{z}} - q_i \hat{\mathbf{k}}_r) + r_{mi}^s \cos \gamma \frac{k_m^2}{q_m} (\hat{\mathbf{z}} \times \hat{\mathbf{k}}_r) \right] \cdot \\ &\quad \cdot \exp(-iq_m z_m) \exp(iq_i(z_0 - z_i))\end{aligned}$$

$$\boldsymbol{\xi}_{\downarrow,i}^- = A \left[t_{mi}^p \left(\frac{\varepsilon_m}{\varepsilon_i} \right)^{1/2} \sin \gamma (k_r \hat{\mathbf{z}} + q_i \hat{\mathbf{k}}_r) + t_{mi}^s \cos \gamma \frac{k_m^2}{q_m} (\hat{\mathbf{z}} \times \hat{\mathbf{k}}_r) \right] \cdot \\ \cdot \exp(-iq_m z_m) \exp(-iq_i(z_0 - z_{i-1}))$$

Case 3: $\mu = \mu \hat{\mathbf{z}}$

$$\boldsymbol{\xi}_{\uparrow,i}^+ = At_{mi}^p \left(\frac{\varepsilon_m}{\varepsilon_i} \right)^{1/2} \frac{k_r}{q_m} (k_r \hat{\mathbf{z}} - q_i \hat{\mathbf{k}}_r) \cdot \exp(iq_m z_{m-1}) \exp(iq_i(z_0 - z_i))$$

$$\boldsymbol{\xi}_{\downarrow,i}^+ = Ar_{mi}^p \frac{k_r}{q_m} (k_r \hat{\mathbf{z}} + q_i \hat{\mathbf{k}}_r) \cdot \exp(iq_m z_{m-1}) \exp(-iq_i(z_0 - z_{i-1}))$$

$$\boldsymbol{\xi}_{\uparrow,i}^- = Ar_{mi}^p \frac{k_r}{q_m} (k_r \hat{\mathbf{z}} - q_i \hat{\mathbf{k}}_r) \cdot \exp(-iq_m z_m) \exp(iq_i(z_0 - z_i))$$

$$\boldsymbol{\xi}_{\downarrow,i}^- = At_{mi}^p \left(\frac{\varepsilon_m}{\varepsilon_i} \right)^{1/2} \frac{k_r}{q_m} (k_r \hat{\mathbf{z}} + q_i \hat{\mathbf{k}}_r) \cdot \exp(-iq_m z_m) \exp(-iq_i(z_0 - z_{i-1}))$$

Some of these results have already been given in [23]. As before the variable $q_i = \sqrt{k_i^2 - k_r^2}$ with $k_i = \omega n_i / c$ such that $\text{Im } q_i \geq 0$ has been used. The factor $A = \mu \exp(i\mathbf{k}_r \cdot \boldsymbol{\rho}_0)$ accounts for the phase shift of the wave traveling in $\hat{\mathbf{k}}_r$ -direction from the dipole at the origin to the observation point $\mathbf{r}_0 = \boldsymbol{\rho}_0 + z_0 \hat{\mathbf{z}}$. The phase shift due to propagation in z -direction within regions i and m is respected by the explicitly given exponential functions, while for all other regions it is absorbed into the reflection and transmission coefficients.

B.1.4. Approximation for a distant observation point

In order to calculate the electric field $\mathbf{E}_i(\mathbf{r}_0)$ at the point of observation as given in eq. (*), the plane wave components $\boldsymbol{\xi}_{\uparrow\downarrow,i}^\pm(\mathbf{k}_r)$ have to be integrated both over $d\gamma$ and over dk_r . The integration over $d\gamma$ is executed first using the additional assumption of a distant observation point. After application of the substitutions

$$\mathbf{k}_r = (k_r \cos \gamma) \hat{\mathbf{p}} + (k_r \sin \gamma) \hat{\mathbf{s}}$$

$$\hat{\mathbf{z}} \times \hat{\mathbf{k}}_r = (-\sin \gamma) \hat{\mathbf{p}} + (\cos \gamma) \hat{\mathbf{s}}$$

to the expressions for $\boldsymbol{\xi}_{\uparrow\downarrow,i}^\pm(\mathbf{k}_r)$ the following integrals and the large-argument limits of the resulting Bessel functions can be used [23]:

$$\int_0^{2\pi} d\gamma \exp(ik_r \rho_0 \cos \gamma) \cos^2 \gamma = \pi [J_0(k_r \rho_0) - J_2(k_r \rho_0)] \rightarrow 2 \left(\frac{2\pi}{k_r \rho_0} \right)^{1/2} \cos(k_r \rho_0 - \frac{\pi}{4})$$

$$\int_0^{2\pi} d\gamma \exp(ik_r \rho_0 \cos \gamma) \sin^2 \gamma = \pi [J_0(k_r \rho_0) + J_2(k_r \rho_0)] \rightarrow 0$$

$$\int_0^{2\pi} d\gamma \exp(ik_r \rho_0 \cos \gamma) \sin \gamma \cos \gamma = 0$$

$$\int_0^{2\pi} d\gamma \exp(ik_r\rho_0 \cos \gamma) \cos \gamma = 2\pi i J_1(k_r\rho_0) \rightarrow 2i \left(\frac{2\pi}{k_r\rho_0}\right)^{1/2} \cos(k_r\rho_0 - \frac{3\pi}{4})$$

$$\int_0^{2\pi} d\gamma \exp(ik_r\rho_0 \cos \gamma) \sin \gamma = 0$$

Here, J_0 , J_1 and J_2 are Bessel functions of the first kind. Considering the large-argument limit $k_r\rho_0 \gg 1$ is equivalent to the assumption $\rho_0 \gg \lambda$. Since the admissible observation points are usually given by the aperture of an objective, ρ_0 is typically in the order of millimeters, so that the assumption of a distant observation point holds true except for a vanishingly small region around the z -axis. Hence, the large-argument limit can be taken, despite the inclusion of $k_r = 0$ in the integration over dk_r , since each integrand also contains a multiplicative factor k_r [23].

The resulting integrals $\Xi_{\uparrow\downarrow,i}^\pm(k_r) = \int_0^{2\pi} d\gamma \boldsymbol{\xi}_{\uparrow\downarrow,i}^\pm(\mathbf{k}_r)$ are again specified for the three different orientations of the dipole moment $\boldsymbol{\mu}$.

Case 1: $\boldsymbol{\mu} = \mu \hat{\mathbf{p}}$

$$\begin{aligned} \Xi_{\uparrow,i}^+ &= 2\mu \left(\frac{2\pi}{k_r\rho_0}\right)^{1/2} t_{mi}^p \left(\frac{\varepsilon_m}{\varepsilon_i}\right)^{1/2} \left[q_i \cos(k_r\rho_0 - \frac{\pi}{4}) \hat{\mathbf{p}} - ik_r \cos(k_r\rho_0 - \frac{3\pi}{4}) \hat{\mathbf{z}} \right] \cdot \\ &\quad \cdot \exp(iq_m z_{m-1}) \exp(iq_i(z_0 - z_i)) \\ \Xi_{\downarrow,i}^+ &= 2\mu \left(\frac{2\pi}{k_r\rho_0}\right)^{1/2} r_{mi}^p \left[-q_i \cos(k_r\rho_0 - \frac{\pi}{4}) \hat{\mathbf{p}} - ik_r \cos(k_r\rho_0 - \frac{3\pi}{4}) \hat{\mathbf{z}} \right] \cdot \\ &\quad \cdot \exp(iq_m z_{m-1}) \exp(-iq_i(z_0 - z_{i-1})) \\ \Xi_{\uparrow,i}^- &= 2\mu \left(\frac{2\pi}{k_r\rho_0}\right)^{1/2} r_{mi}^p \left[-q_i \cos(k_r\rho_0 - \frac{\pi}{4}) \hat{\mathbf{p}} + ik_r \cos(k_r\rho_0 - \frac{3\pi}{4}) \hat{\mathbf{z}} \right] \cdot \\ &\quad \cdot \exp(-iq_m z_m) \exp(iq_i(z_0 - z_i)) \\ \Xi_{\downarrow,i}^- &= 2\mu \left(\frac{2\pi}{k_r\rho_0}\right)^{1/2} t_{mi}^p \left(\frac{\varepsilon_m}{\varepsilon_i}\right)^{1/2} \left[q_i \cos(k_r\rho_0 - \frac{\pi}{4}) \hat{\mathbf{p}} + ik_r \cos(k_r\rho_0 - \frac{3\pi}{4}) \hat{\mathbf{z}} \right] \cdot \\ &\quad \cdot \exp(-iq_m z_m) \exp(-iq_i(z_0 - z_{i-1})) \end{aligned}$$

Case 2: $\boldsymbol{\mu} = \mu \hat{\mathbf{s}}$

$$\begin{aligned} \Xi_{\uparrow,i}^+ &= 2\mu \left(\frac{2\pi}{k_r\rho_0}\right)^{1/2} t_{mi}^s \frac{k_m^2}{q_m} \cos(k_r\rho_0 - \frac{\pi}{4}) \hat{\mathbf{s}} \cdot \exp(iq_m z_{m-1}) \exp(iq_i(z_0 - z_i)) \\ \Xi_{\downarrow,i}^+ &= 2\mu \left(\frac{2\pi}{k_r\rho_0}\right)^{1/2} r_{mi}^s \frac{k_m^2}{q_m} \cos(k_r\rho_0 - \frac{\pi}{4}) \hat{\mathbf{s}} \cdot \exp(iq_m z_{m-1}) \exp(-iq_i(z_0 - z_{i-1})) \\ \Xi_{\uparrow,i}^- &= 2\mu \left(\frac{2\pi}{k_r\rho_0}\right)^{1/2} r_{mi}^s \frac{k_m^2}{q_m} \cos(k_r\rho_0 - \frac{\pi}{4}) \hat{\mathbf{s}} \cdot \exp(-iq_m z_m) \exp(iq_i(z_0 - z_i)) \end{aligned}$$

$$\boldsymbol{\Xi}_{\downarrow,i}^- = 2\mu \left(\frac{2\pi}{k_r\rho_0} \right)^{1/2} t_{mi}^s \frac{k_m^2}{q_m} \cos(k_r\rho_0 - \frac{\pi}{4}) \hat{\mathbf{s}} \cdot \exp(-iq_m z_m) \exp(-iq_i(z_0 - z_{i-1}))$$

Case 3: $\mu = \mu \hat{\mathbf{z}}$

$$\begin{aligned} \boldsymbol{\Xi}_{\uparrow,i}^+ &= 2\mu \left(\frac{2\pi}{k_r\rho_0} \right)^{1/2} t_{mi}^p \left(\frac{\varepsilon_m}{\varepsilon_i} \right)^{1/2} \left[-i \frac{k_r q_i}{q_m} \cos(k_r\rho_0 - \frac{3\pi}{4}) \hat{\mathbf{p}} + \frac{k_r^2}{q_m} \cos(k_r\rho_0 - \frac{\pi}{4}) \hat{\mathbf{z}} \right] \cdot \\ &\quad \cdot \exp(iq_m z_{m-1}) \exp(iq_i(z_0 - z_i)) \\ \boldsymbol{\Xi}_{\downarrow,i}^+ &= 2\mu \left(\frac{2\pi}{k_r\rho_0} \right)^{1/2} r_{mi}^p \left[i \frac{k_r q_i}{q_m} \cos(k_r\rho_0 - \frac{3\pi}{4}) \hat{\mathbf{p}} + \frac{k_r^2}{q_m} \cos(k_r\rho_0 - \frac{\pi}{4}) \hat{\mathbf{z}} \right] \cdot \\ &\quad \cdot \exp(iq_m z_{m-1}) \exp(-iq_i(z_0 - z_{i-1})) \\ \boldsymbol{\Xi}_{\uparrow,i}^- &= 2\mu \left(\frac{2\pi}{k_r\rho_0} \right)^{1/2} r_{mi}^p \left[-i \frac{k_r q_i}{q_m} \cos(k_r\rho_0 - \frac{3\pi}{4}) \hat{\mathbf{p}} + \frac{k_r^2}{q_m} \cos(k_r\rho_0 - \frac{\pi}{4}) \hat{\mathbf{z}} \right] \cdot \\ &\quad \cdot \exp(-iq_m z_m) \exp(iq_i(z_0 - z_i)) \\ \boldsymbol{\Xi}_{\downarrow,i}^- &= 2\mu \left(\frac{2\pi}{k_r\rho_0} \right)^{1/2} t_{mi}^p \left(\frac{\varepsilon_m}{\varepsilon_i} \right)^{1/2} \left[i \frac{k_r q_i}{q_m} \cos(k_r\rho_0 - \frac{3\pi}{4}) \hat{\mathbf{p}} + \frac{k_r^2}{q_m} \cos(k_r\rho_0 - \frac{\pi}{4}) \hat{\mathbf{z}} \right] \cdot \\ &\quad \cdot \exp(-iq_m z_m) \exp(-iq_i(z_0 - z_{i-1})) \end{aligned}$$

Since the radiation emitted by the dipole is usually detected in regions 1 or M only the plane wave components $\boldsymbol{\Xi}_1 = \boldsymbol{\Xi}_{\uparrow,1}^+ + \boldsymbol{\Xi}_{\uparrow,1}^-$ and $\boldsymbol{\Xi}_M = \boldsymbol{\Xi}_{\downarrow,M}^+ + \boldsymbol{\Xi}_{\downarrow,M}^-$ are considered further. Of course, there are no contributions of $\boldsymbol{\Xi}_{\downarrow,1}^\pm$ to $\boldsymbol{\Xi}_1$ or of $\boldsymbol{\Xi}_{\uparrow,M}^\pm$ to $\boldsymbol{\Xi}_M$. The explicit expressions for $\boldsymbol{\Xi}_1$ and $\boldsymbol{\Xi}_M$ are given below.

Case 1: $\mu = \mu \hat{\mathbf{p}}$

$$\begin{aligned} \boldsymbol{\Xi}_1 &= 2\mu \left(\frac{2\pi}{k_r\rho_0} \right)^{1/2} \exp(iq_1(z_0 - z_1)) \cdot \\ &\quad \cdot \left[\left(t_{m1}^p \left(\frac{\varepsilon_m}{\varepsilon_1} \right)^{1/2} \exp(iq_m z_{m-1}) - r_{m1}^p \exp(-iq_m z_m) \right) q_1 \cos(k_r\rho_0 - \frac{\pi}{4}) \hat{\mathbf{p}} + \right. \\ &\quad \left. + \left(-t_{m1}^p \left(\frac{\varepsilon_m}{\varepsilon_1} \right)^{1/2} \exp(iq_m z_{m-1}) + r_{m1}^p \exp(-iq_m z_m) \right) ik_r \cos(k_r\rho_0 - \frac{3\pi}{4}) \hat{\mathbf{z}} \right] \\ \boldsymbol{\Xi}_M &= 2\mu \left(\frac{2\pi}{k_r\rho_0} \right)^{1/2} \exp(-iq_M(z_0 - z_{M-1})) \cdot \\ &\quad \cdot \left[\left(-r_{mM}^p \exp(iq_m z_{m-1}) + t_{mM}^p \left(\frac{\varepsilon_m}{\varepsilon_M} \right)^{1/2} \exp(-iq_m z_m) \right) q_M \cos(k_r\rho_0 - \frac{\pi}{4}) \hat{\mathbf{p}} + \right. \\ &\quad \left. + \left(-r_{mM}^p \exp(iq_m z_{m-1}) + t_{mM}^p \left(\frac{\varepsilon_m}{\varepsilon_M} \right)^{1/2} \exp(-iq_m z_m) \right) ik_r \cos(k_r\rho_0 - \frac{3\pi}{4}) \hat{\mathbf{z}} \right] \end{aligned}$$

Case 2: $\mu = \mu \hat{\mathbf{s}}$

$$\begin{aligned}\boldsymbol{\Xi}_1 &= 2\mu \left(\frac{2\pi}{k_r \rho_0} \right)^{1/2} \exp(iq_1(z_0 - z_1)) \cdot \frac{k_m^2}{q_m} \cos(k_r \rho_0 - \frac{\pi}{4}) \hat{\mathbf{s}} \cdot \\ &\quad \cdot [t_{m1}^s \exp(iq_m z_{m-1}) + r_{m1}^s \exp(-iq_m z_m)] \\ \boldsymbol{\Xi}_M &= 2\mu \left(\frac{2\pi}{k_r \rho_0} \right)^{1/2} \exp(-iq_M(z_0 - z_{M-1})) \cdot \frac{k_m^2}{q_m} \cos(k_r \rho_0 - \frac{\pi}{4}) \hat{\mathbf{s}} \cdot \\ &\quad \cdot [r_{mM}^s \exp(iq_m z_{m-1}) + t_{mM}^s \exp(-iq_m z_m)]\end{aligned}$$

Case 3: $\mu = \mu \hat{\mathbf{z}}$

$$\begin{aligned}\boldsymbol{\Xi}_1 &= 2\mu \left(\frac{2\pi}{k_r \rho_0} \right)^{1/2} \exp(iq_1(z_0 - z_1)) \cdot \\ &\quad \cdot \left[\left(-t_{m1}^p \left(\frac{\varepsilon_m}{\varepsilon_1} \right)^{1/2} \exp(iq_m z_{m-1}) - r_{m1}^p \exp(-iq_m z_m) \right) i \frac{k_r q_1}{q_m} \cos(k_r \rho_0 - \frac{3\pi}{4}) \hat{\mathbf{p}} + \right. \\ &\quad \left. + \left(t_{m1}^p \left(\frac{\varepsilon_m}{\varepsilon_1} \right)^{1/2} \exp(iq_m z_{m-1}) + r_{m1}^p \exp(-iq_m z_m) \right) \frac{k_r^2}{q_m} \cos(k_r \rho_0 - \frac{\pi}{4}) \hat{\mathbf{z}} \right] \\ \boldsymbol{\Xi}_M &= 2\mu \left(\frac{2\pi}{k_r \rho_0} \right)^{1/2} \exp(-iq_M(z_0 - z_{M-1})) \cdot \\ &\quad \cdot \left[\left(r_{mM}^p \exp(iq_m z_{m-1}) + t_{mM}^p \left(\frac{\varepsilon_m}{\varepsilon_M} \right)^{1/2} \exp(-iq_m z_m) \right) i \frac{k_r q_M}{q_m} \cos(k_r \rho_0 - \frac{3\pi}{4}) \hat{\mathbf{p}} + \right. \\ &\quad \left. + \left(r_{mM}^p \exp(iq_m z_{m-1}) + t_{mM}^p \left(\frac{\varepsilon_m}{\varepsilon_M} \right)^{1/2} \exp(-iq_m z_m) \right) \frac{k_r^2}{q_m} \cos(k_r \rho_0 - \frac{\pi}{4}) \hat{\mathbf{z}} \right]\end{aligned}$$

B.1.5. Method of steepest descents

Following [23] the remaining integral over dk_r k_r can be approximated using the method of steepest descents [2, pp. 489–493]. By using

$$\cos(k_r \rho_0 + l) = \frac{1}{2} [\exp(i(k_r \rho_0 + l)) + \exp(-i(k_r \rho_0 + l))]$$

with either $l = -\frac{1}{4}$ or $l = -\frac{3}{4}$ each term in the expressions for $\boldsymbol{\Xi}_1$ any $\boldsymbol{\Xi}_M$ can be written as

$$F(k_r) \exp(\kappa iq_m z_n) \exp(\mu iq_j(z_0 - z_k)) \exp(\nu ik_r \rho_0) \exp(\nu il)$$

with signs $\kappa, \mu, \nu = \pm 1$, indices j, k and n and a function $F(k_r)$ that only depends on k_r and in particular absorbs all constants and transmission or reflection coefficients. Transforming into spherical coordinates by introducing $z_0 = r_0 \cos \theta_0$ and $\rho_0 = r_0 \sin \theta_0$ this takes the form

$$F(k_r) \exp(\kappa iq_m z_n) \exp(-\mu iq_j z_k) \exp(\mu iq_j r_0 \cos \theta_0) \exp(\nu ik_r r_0 \sin \theta_0) \exp(\nu il)$$

where $\theta_0 < 90^\circ$ in region 1 and $\theta_0 > 90^\circ$ in region M . Hence the integral $\mathbf{E}_i = \int_0^\infty dk_r k_r \mathbf{\Xi}_i$ can be written as

$$\int_0^\infty dk_r g(k_r) \cdot \exp(ir_0 f(k_r))$$

like in [2, p. 492], where $f(k_r)$ and $g(k_r)$ are defined as:

$$\begin{aligned} f(k_r) &= \mu q_j \cos \theta_0 + \nu k_r \sin \theta_0 \\ g(k_r) &= k_r F(k_r) \exp(\kappa i q_m z_n) \exp(-\mu i q_j z_k) \exp(\nu i l) \end{aligned}$$

For large r_0 , i.e. again for a distant observation point, $\exp(ir_0 f(k_r))$ oscillates rapidly compared to changes of $g(k_r)$. Hence, the main contribution to the integral expression for \mathbf{E}_i comes from a small region around the saddle point of $f(k_r)$ as illustrated in figs. B.2 (a) and B.2 (b). Formalizing this idea results in the method of steepest descents as described in [2, pp. 489–493].

The saddle point $k_{r,0}$ of $f(k_r)$ can be found by simple differentiation. However, the sign of the saddle point depends on μ and ν as well as the region:

$$f'(k_r) = 0 \quad \Rightarrow \quad k_{r,0} = \begin{cases} \mu \nu k_1 \sin \theta_0 & \text{for region 1} \\ -\mu \nu k_M \sin \theta_0 & \text{for region } M \end{cases}$$

For negative $k_{r,0}$ there is no saddle point of $f(k_r)$ on the positive real axis. Hence, $\exp(ir_0 f(k_r))$ oscillates strongly for $k_r < k_j$ and decays exponentially for $k_r > k_j$, where q_j is imaginary. Therefore, the contribution of terms with a positive real saddle point $k_{r,0} > 0$ is dominant, while those with negative $k_{r,0} < 0$ can be neglected (cf. fig. B.2 (c)).

Since $\mathbf{\Xi}_1$ contains only exponential functions with $\mu = +1$, in region 1 only terms with $\nu = +1$ contribute, while terms with $\nu = -1$ can be neglected. Similarly, $\mu = -1$ for region M and again only terms with $\nu = +1$ contribute. In any case, one obtains

$$k_{r,0} = k_j \sin \theta_0.$$

Using these values for μ and ν as well as the result from [2, p. 493] the following approximative value for the desired integral can be calculated:

$$\begin{aligned} \int_0^\infty dk_r g(k_r) \cdot \exp(ir_0 f(k_r)) &\approx \frac{\sqrt{2\pi} g(k_{r,0}) \exp(ir_0 f(k_{r,0})) \exp(i\frac{\pi}{4})}{|ir_0 f''(k_{r,0})|^{1/2}} = \\ &= \sqrt{\frac{2\pi k_j}{r_0}} g(k_{r,0}) \exp(ir_0 f(k_{r,0})) \exp(i\frac{\pi}{4}) |\cos \theta_0| \end{aligned}$$

Numerical evaluation of this integral suggests an excellent agreement of exact and approximate solution. One interesting consequence of the obtained result is that due to $q_j(k_{r,0}) = k_j \cos \theta_0$ the two-phase reflection and transmission coefficients $r_{ij}(k_{r,0})$ and $t_{ij}(k_{r,0})$ are only evaluated at the angles corresponding to the light paths of geometrical optics.

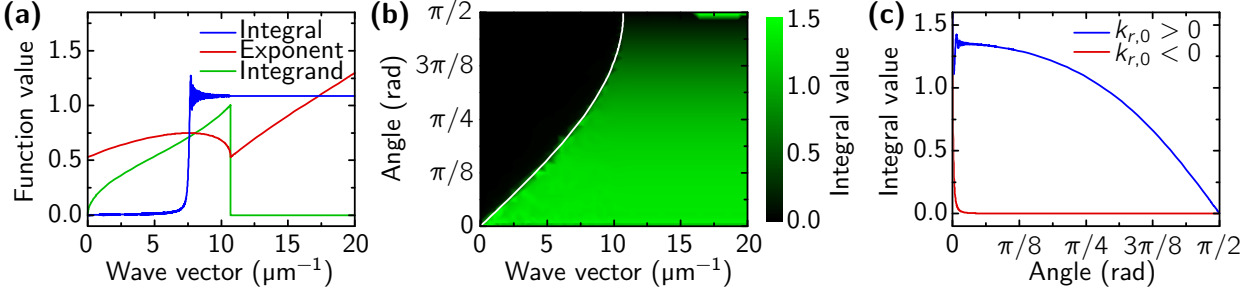


Figure B.2.: Comparison of numerical results and method of steepest descents. **(a)** Integrand $g(k_r)$, exponent $i r_0 f(k_r)$ and numerically evaluated integral $\int_0^{k_r} ds g(s) \cdot \exp(i r_0 f(s))$ as function of wave vector k_r . The greatest change of the integral does not occur at the largest value of the integrand $g(k_r)$ but at the saddle point of the exponent $f(k_r)$ as predicted by the method of steepest descents. **(b)** Numerically evaluated integral $\int_0^{k_r} ds g(s) \cdot \exp(i r_0 f(s))$ as function of wave vector k_r and angle θ_0 . The white line shows the saddle point of the exponent $i r_0 f(k_r)$ at which the method of steepest descents predicts the largest change of the integral value. **(c)** Comparison of numerical integrals $\int_0^\infty dk_r g(k_r) \cdot \exp(i r_0 f(k_r))$ for positive (blue line) and negative (red line) saddle point of the exponent $i r_0 f(k_r)$. As predicted by the method of steepest descents the contribution of terms with negative saddle point can be neglected.

A subtlety that has not been mentioned so far is hidden in the term $g(k_r)$. For application of the method of steepest descents a slow variation of $g(k_r)$ compared to the oscillating term $\exp(i r_0 f(k_r))$ was assumed. For $\boldsymbol{\mu} = \mu \hat{\mathbf{s}}$ and $\boldsymbol{\mu} = \mu \hat{\mathbf{z}}$, however, $g(k_r)$ contains $q_m(k_r)$ in the denominator and thus a pole at k_m , so that this assumption is not necessarily valid.

The first important observation is that the integral of $1/q_m(k_r)$ over a finite interval around its pole is also finite. For $k_m > k_j$, i. e. $n_m > n_j$ the exponent $i r_0 f(k_m)$ has a non-zero real part since $q_j(k_m)$ is imaginary. Hence, the contribution from the term $1/q_m(k_r)$ is damped exponentially and does not need to be considered. The case $k_m < k_j$, however, is more complicated.

In order to treat this case, the real part of the exponent $i r_0 f(k_r)$ is only considered at k_m , while the imaginary part is expanded to first order:

$$\begin{aligned} ir_0 f(k_r) &\approx \underbrace{\text{Re}(ir_0 f(k_m))}_{\text{Approximation of real part}} + \underbrace{i \text{Im}(ir_0 f(k_m)) + i(k_r - k_m) \text{Im}(ir_0 f'(k_m))}_{\text{Approximation of imaginary part}} = \\ &= ir_0 f(k_m) + ir_0(k_r - k_m) \text{Re } f'(k_m) \end{aligned}$$

Writing $g(k_r) = \hat{g}(k_r) \cdot 1/q_m$ the contribution of the pole at k_m can be estimated by the following integral:

$$\begin{aligned} \int_0^\infty dk_r \hat{g}(k_m) \cdot \frac{1}{q_m(k_r)} \cdot \exp[i r_0 f(k_m) + ir_0(k_r - k_m) \text{Re } f'(k_m)] &= \\ &= \hat{g}(k_m) \exp[i r_0 f(k_m) - ir_0 k_m \text{Re } f'(k_m)] \int_0^\infty dk_r \frac{\exp(ir_0 k_r \text{Re } f'(k_m))}{\sqrt{k_m^2 - k_r^2}} \end{aligned}$$

Since the imaginary part of the exponent is only considered up to first order, there is no saddle point, to which the method of steepest descents could be applied. Hence, the above integration is expected to yield zero except for a small interval around the pole, where $g(k_r)$ is rapidly changing. Numerical integration indeed suggests that the chosen approximation of the behavior around the pole results in negligible errors. The remaining integral has been solved analytically using Mathematica:

$$\int_0^\infty dk_r \frac{\exp(ia k_r)}{\sqrt{k_m^2 - k_r^2}} = \frac{1}{2} i \pi [Y_0(ak_m) + H_0(ak_m)] + \pi J_0(ak_m)$$

For this result to hold true the condition $a \in \mathbb{R}$ is crucial. On the right-hand side, J_0 is the Bessel function of the first kind, Y_0 is the Bessel function of the second kind and H_0 is the Struve function. Again it is instructive to consider the large-argument limit of this expression:

$$\int_0^\infty dk_r \frac{\exp(ia k_r)}{\sqrt{k_m^2 - k_r^2}} \rightarrow \frac{i}{ak_m} + \Theta(a) \sqrt{\frac{2\pi}{ak_m}} \exp(i(ak_m - \frac{\pi}{4})),$$

where $\Theta(a)$ is the Heaviside step function. Application of this result to the above expression finally results in:

$$\begin{aligned} \int_0^\infty dk_r \hat{g}(k_m) \cdot \frac{1}{q_m(k_r)} \cdot \exp[i r_0 f(k_m) + ir_0(k_r - k_m) \operatorname{Re} f'(k_m)] &\rightarrow \\ &\rightarrow \hat{g}(k_m) \exp[i r_0 f(k_m) - ir_0 k_m \operatorname{Re} f'(k_m)] \cdot \left[\frac{i}{r_0 k_m \operatorname{Re} f'(k_m)} + \right. \\ &\quad \left. + \Theta(\operatorname{Re} f'(k_m)) \sqrt{\frac{2\pi}{r_0 k_m \operatorname{Re} f'(k_m)}} \exp[i(r_0 k_m \operatorname{Re} f'(k_m) - \frac{\pi}{4})] \right] \end{aligned}$$

When $k_m < k_j$, the condition $\operatorname{Re} f'(k_m) > 0$ is equivalent to $\sin \theta_0 > k_m/k_j$. This means, however, that θ_0 is larger than the angle of total internal reflection when considering the two phases with refractive indices n_m and n_j . Since the radiation emitted by the dipole is normally detected in the far-field limit, no light at all is expected for such angles. Hence, from a physical point of view, only the case $\operatorname{Re} f'(k_m) < 0$ needs to be considered, which simplifies the above result:

$$\begin{aligned} \int_0^\infty dk_r \hat{g}(k_m) \cdot \frac{1}{q_m(k_r)} \cdot \exp[i r_0 f(k_m) + ir_0(k_r - k_m) \operatorname{Re} f'(k_m)] &\rightarrow \\ &\rightarrow \hat{g}(k_m) \exp[i r_0(f(k_m) - k_m \operatorname{Re} f'(k_m))] \cdot \frac{i}{r_0 k_m \operatorname{Re} f'(k_m)} \end{aligned}$$

This term is of order r^{-1} , while the result obtained using the method of steepest descents is of order $r^{-1/2}$. Thus, in the limit of large r , this additional term only contributes small corrections and can be neglected, as was already indicated by numerical integration. For higher accuracy, however, it may easily be incorporated in the following discussion. The electric fields in regions 1 and M using the results from the method of steepest descents only are as follows.

Case 1: $\mu = \mu \hat{\mathbf{p}}$

$$\begin{aligned} \mathbf{E}_1^p(\mathbf{r}_0) &= B k_1 \exp(i q_1(r_0 \cos \theta_0 - z_1)) \exp(ir_0 k_1 \sin^2 \theta_0) \cdot \\ &\quad \cdot \left[\left(t_{m1}^p \left(\frac{\varepsilon_m}{\varepsilon_1} \right)^{1/2} \exp(i q_m z_{m-1}) - r_{m1}^p \exp(-i q_m z_m) \right) q_1 \hat{\mathbf{p}} + \right. \\ &\quad \left. + \left(-t_{m1}^p \left(\frac{\varepsilon_m}{\varepsilon_1} \right)^{1/2} \exp(i q_m z_{m-1}) + r_{m1}^p \exp(-i q_m z_m) \right) k_1 \sin \theta_0 \hat{\mathbf{z}} \right] \end{aligned}$$

$$\begin{aligned} \mathbf{E}_M^p(\mathbf{r}_0) &= B k_M \exp(-i q_M(r_0 \cos \theta_0 - z_{M-1})) \exp(ir_0 k_M \sin^2 \theta_0) \cdot \\ &\quad \cdot \left[\left(-r_{mM}^p \exp(i q_m z_{m-1}) + t_{mM}^p \left(\frac{\varepsilon_m}{\varepsilon_M} \right)^{1/2} \exp(-i q_m z_m) \right) q_M \hat{\mathbf{p}} + \right. \\ &\quad \left. + \left(-r_{mM}^p \exp(i q_m z_{m-1}) + t_{mM}^p \left(\frac{\varepsilon_m}{\varepsilon_M} \right)^{1/2} \exp(-i q_m z_m) \right) k_M \sin \theta_0 \hat{\mathbf{z}} \right] \end{aligned}$$

Case 2: $\mu = \mu \hat{\mathbf{s}}$

$$\begin{aligned} \mathbf{E}_1^s(\mathbf{r}_0) &= B k_1 \exp(i q_1(r_0 \cos \theta_0 - z_1)) \exp(ir_0 k_1 \sin^2 \theta_0) \cdot \frac{k_m^2}{q_m} \hat{\mathbf{s}} \cdot \\ &\quad \cdot [t_{m1}^s \exp(i q_m z_{m-1}) + r_{m1}^s \exp(-i q_m z_m)] \\ \mathbf{E}_M^s(\mathbf{r}_0) &= B k_M \exp(-i q_M(r_0 \cos \theta_0 - z_{M-1})) \exp(ir_0 k_M \sin^2 \theta_0) \cdot \frac{k_m^2}{q_m} \hat{\mathbf{s}} \cdot \\ &\quad \cdot [r_{mM}^s \exp(i q_m z_{m-1}) + t_{mM}^s \exp(-i q_m z_m)] \end{aligned}$$

Case 3: $\mu = \mu \hat{\mathbf{z}}$

$$\begin{aligned} \mathbf{E}_1^z(\mathbf{r}_0) &= B k_1 \exp(i q_1(r_0 \cos \theta_0 - z_1)) \exp(ir_0 k_1 \sin^2 \theta_0) \cdot \\ &\quad \cdot \left[\left(-t_{m1}^p \left(\frac{\varepsilon_m}{\varepsilon_i} \right)^{1/2} \exp(i q_m z_{m-1}) - r_{m1}^p \exp(-i q_m z_m) \right) \frac{k_1 q_1 \sin \theta_0}{q_m} \hat{\mathbf{p}} + \right. \\ &\quad \left. + \left(t_{m1}^p \left(\frac{\varepsilon_m}{\varepsilon_i} \right)^{1/2} \exp(i q_m z_{m-1}) + r_{m1}^p \exp(-i q_m z_m) \right) \frac{k_1^2 \sin^2 \theta_0}{q_m} \hat{\mathbf{z}} \right] \end{aligned}$$

$$\begin{aligned} \mathbf{E}_M^z(\mathbf{r}_0) &= B k_M \exp(-i q_M(r_0 \cos \theta_0 - z_{M-1})) \exp(ir_0 k_M \sin^2 \theta_0) \cdot \\ &\quad \cdot \left[\left(r_{mM}^p \exp(i q_m z_{m-1}) + t_{mM}^p \left(\frac{\varepsilon_m}{\varepsilon_i} \right)^{1/2} \exp(-i q_m z_m) \right) \frac{k_M q_M \sin \theta_0}{q_m} \hat{\mathbf{p}} + \right. \\ &\quad \left. + \left(r_{mM}^p \exp(i q_m z_{m-1}) + t_{mM}^p \left(\frac{\varepsilon_m}{\varepsilon_i} \right)^{1/2} \exp(-i q_m z_m) \right) \frac{k_M^2 \sin^2 \theta_0}{q_m} \hat{\mathbf{z}} \right] \end{aligned}$$

Here, the abbreviation $B = 2\pi\mu \cos \theta_0 / r_0$ has been used. In the above expressions, all q_i , all transmission and all reflection coefficients need to be evaluated at $k_1 \sin \theta_0$ and $k_M \sin \theta_0$ for \mathbf{E}_1 and \mathbf{E}_M , respectively. At this point the only missing information is how to calculate the transmission and reflection coefficients, which is addressed in the following section.

B.2. Numerical calculation of transmission and reflection coefficients

An exact calculation of the reflection and transmission coefficients is only possible in the most simple cases with two or three different phases. For two phases, the coefficients have already been given above, while for three phases they can be calculated by a geometric sum:

$$r_{13}^{p,s}(k_r) = \frac{r_{12}^{p,s}(k_r) + r_{23}^{p,s}(k_r) \exp[2iq_2(k_r)(z_1 - z_2)]}{1 + r_{12}^{p,s}(k_r)r_{23}^{p,s}(k_r) \exp[2iq_2(k_r)(z_1 - z_2)]}$$

$$r_{31}^{p,s}(k_r) = \frac{r_{32}^{p,s}(k_r) + r_{21}^{p,s}(k_r) \exp[2iq_2(k_r)(z_1 - z_2)]}{1 + r_{12}^{p,s}(k_r)r_{23}^{p,s}(k_r) \exp[2iq_2(k_r)(z_1 - z_2)]}$$

$$t_{13}^{p,s}(k_r) = \frac{t_{12}^{p,s}(k_r)t_{23}^{p,s}(k_r) \exp[iq_2(k_r)(z_1 - z_2)]}{1 + r_{12}^{p,s}(k_r)r_{23}^{p,s}(k_r) \exp[2iq_2(k_r)(z_1 - z_2)]}$$

$$t_{31}^{p,s}(k_r) = \frac{t_{32}^{p,s}(k_r)t_{21}^{p,s}(k_r) \exp[iq_2(k_r)(z_1 - z_2)]}{1 + r_{12}^{p,s}(k_r)r_{23}^{p,s}(k_r) \exp[2iq_2(k_r)(z_1 - z_2)]}$$

In the general case with an arbitrary number of different phases a numerical calculation of the transmission and reflection coefficients is necessary. To this end, an algorithm for the calculation of $t_{m1}^{p,s}$, $t_{mM}^{p,s}$, $r_{m1}^{p,s}$ and $r_{mM}^{p,s}$ is sketched in the following.

The main idea is a stepwise increase of the number of interfaces (i. e. plane phase boundaries between the different regions) with which a plane wave of specific wave vector \mathbf{k} interacts

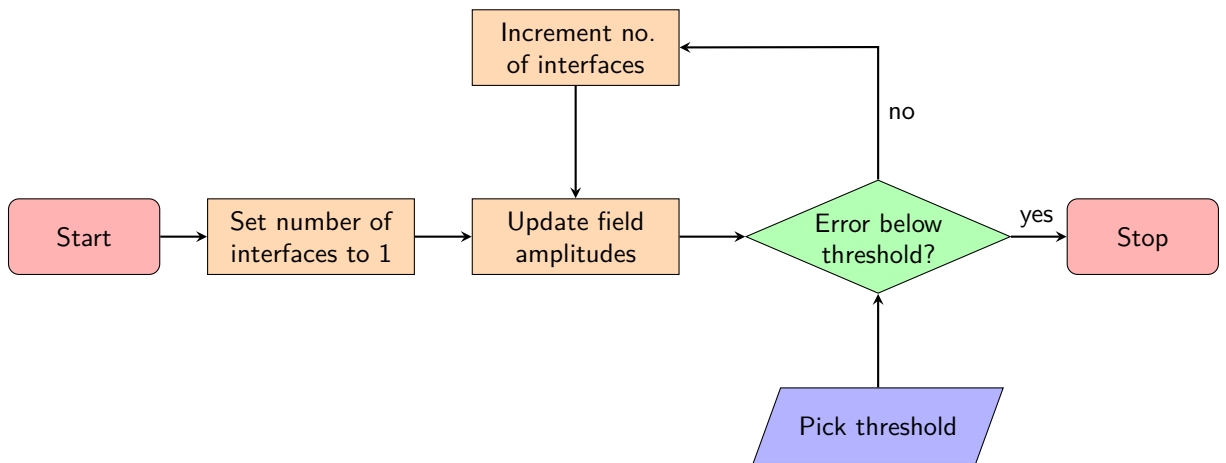


Figure B.3.: Flowchart illustration of an algorithm to calculate transmission and reflection coefficients for an arbitrary number of phases.

Input: Threshold ε
Data: List of refractive indices \mathbf{n}
Data: List of phase boundary coordinates \mathbf{z}

```

1  $\mathbf{U} := \text{Zeros}(M);$ 
2  $\mathbf{D} := \text{Zeros}(M);$ 
3  $\mathbf{U}[m] := 1;$ 
4  $I = \text{Intensity}(\mathbf{U}[m], \mathbf{D}[m]);$ 

5 while  $\text{Abs}(\text{Intensity}(\mathbf{U}[1], \mathbf{D}[1]) + \text{Intensity}(\mathbf{U}[M], \mathbf{D}[M]) - I) > \varepsilon$  do
6   for  $i := 2$  to  $M - 1$  do
7      $\tilde{\mathbf{U}}[i] := (t_{i+1,i}\mathbf{U}[i+1] + r_{i,i+1}\mathbf{D}[i]) * \text{PhaseFactor}(z_{i-1} - z_i);$ 
8      $\tilde{\mathbf{D}}[i] := (t_{i-1,i}\mathbf{D}[i-1] + r_{i,i-1}\mathbf{U}[i]) * \text{PhaseFactor}(z_{i-1} - z_i);$ 
9   end
10   $\tilde{\mathbf{U}}[1] := \mathbf{U}[1] + t_{21}\mathbf{U}[2];$ 
11   $\tilde{\mathbf{D}}[M] := \mathbf{D}[M] + t_{M-1,M}\mathbf{D}[M-1];$ 
12   $\mathbf{U} := \tilde{\mathbf{U}};$ 
13   $\mathbf{D} := \tilde{\mathbf{D}};$ 
14 end

15  $t_{m1} := \mathbf{U}[1];$ 
16  $r_{mM} := \mathbf{D}[M];$ 

17  $\mathbf{U} := \text{Zeros}(M);$ 
18  $\mathbf{D} := \text{Zeros}(M);$ 
19  $\mathbf{D}[m] := 1;$ 
20  $I = \text{Intensity}(\mathbf{U}[m], \mathbf{D}[m]);$ 

21 while  $\text{Abs}(\text{Intensity}(\mathbf{U}[1], \mathbf{D}[1]) + \text{Intensity}(\mathbf{U}[M], \mathbf{D}[M]) - I) > \varepsilon$  do
22   for  $i := 2$  to  $M - 1$  do
23      $\tilde{\mathbf{U}}[i] := (t_{i+1,i}\mathbf{U}[i+1] + r_{i,i+1}\mathbf{D}[i]) * \text{PhaseFactor}(z_{i-1} - z_i);$ 
24      $\tilde{\mathbf{D}}[i] := (t_{i-1,i}\mathbf{D}[i-1] + r_{i,i-1}\mathbf{U}[i]) * \text{PhaseFactor}(z_{i-1} - z_i);$ 
25   end
26    $\tilde{\mathbf{U}}[1] := \mathbf{U}[1] + t_{21}\mathbf{U}[2];$ 
27    $\tilde{\mathbf{D}}[M] := \mathbf{D}[M] + t_{M-1,M}\mathbf{D}[M-1];$ 
28    $\mathbf{U} := \tilde{\mathbf{U}};$ 
29    $\mathbf{D} := \tilde{\mathbf{D}};$ 
30 end

31  $r_{m1} := \mathbf{U}[1];$ 
32  $t_{mM} := \mathbf{D}[M];$ 
33 return  $[t_{m1}, r_{m1}, t_{mM}, r_{mM}];$ 
```

Algorithm B.1: Pseudocode implementation of an algorithm to calculate transmission and reflection coefficients for an arbitrary number of phases.

as illustrated in fig. B.3. A pseudocode implementation of a possible algorithm is given in algorithm B.1.

Two arrays \mathbf{U} and \mathbf{D} are used to store the amplitudes of plane waves traveling upward and downward, respectively, and initialized with only an upward moving field of amplitude 1 in region m . The intensity of this field is calculated and saved for later use as termination condition.

Due to conservation of energy, the intensity of the initial plane wave in region m and the sum of the intensities of the final outgoing plane waves in regions 1 and M have to be the same. Hence, the difference of these two values can be used as an estimate for the accuracy of the numerical calculation. Accordingly, the while loop calculating the reflected and transmitted field amplitudes terminates when this difference drops below a predefined threshold value.

In the body of the while loop the components 2 to $M - 1$ of the arrays \mathbf{U} and \mathbf{D} are updated according to Snell's law including phase factors due to propagation in z -direction, where for each iteration one more transmission or reflection is considered. It has to be noted, that $\mathbf{U}[i]$ is the amplitude *an the top end* of region i , while $\mathbf{D}[i]$ is the amplitude *at the bottom end* of region i of upward and downward propagating waves, respectively.

Only $\mathbf{U}[1]$ and $\mathbf{D}[M]$ differ from this convention and contain the amplitudes at the bottom end of region 1 and at the top end of region M , respectively. Furthermore, $\mathbf{U}[1]$ and $\mathbf{D}[M]$ are not overwritten like the other components of \mathbf{U} and \mathbf{D} but “collect” the values of each iteration round. This ensures that the plane wave eventually “leaks” into regions 1 and M and the loop terminates.

The desired transmission and reflection coefficients are finally equal to $\mathbf{U}[1]$ and $\mathbf{D}[M]$, since the initial amplitude was chosen to be 1. In the second half of the code, the same procedure is repeated for a downward traveling initial plane wave. The obtained result, of course, only holds true for one specific value of k_r , which is used to calculate the two-phase reflection and transmission coefficients required throughout the algorithm. Hence, this procedure has to be called for each needed value of k_r , which may result in high computational costs.

B.3. Dipole radiating with a fixed power

Reintroducing an arbitrary dipole orientation, the dipole moment $\boldsymbol{\mu}$ can be expressed in the basis given by $\hat{\mathbf{p}}$, $\hat{\mathbf{s}}$, $\hat{\mathbf{z}}$ by

$$\boldsymbol{\mu} = \mu_p \hat{\mathbf{p}} + \mu_s \hat{\mathbf{s}} + \mu_z \hat{\mathbf{z}}$$

where

$$\begin{aligned}\mu_p &= \mu \sin \theta \cos(\varphi - \varphi_0) \\ \mu_s &= \mu \sin \theta \sin(\varphi - \varphi_0) \\ \mu_z &= \mu \cos \theta\end{aligned}$$

By application of the superposition principle the electric field in regions 1 and M can thus be written as follows:

$$\mathbf{E}(\mathbf{r}_0, \theta, \varphi) = \sin \theta \cos(\varphi - \varphi_0) \mathbf{E}^p + \sin \theta \sin(\varphi - \varphi_0) \mathbf{E}^s + \cos \theta \mathbf{E}^z$$

Since an optically excited dipole is expected to radiate at constant power [23], this field needs to be normalized by the total dissipated power P_T , i. e. both radiative and nonradiative contributions have to be considered. This quantity is obtained by calculating the work done by the oscillating dipole moment in the field present at the position of the dipole. The result given in [23] cannot be used here, since it assumes a simplified geometry.

The field strength at the position of the dipole is obtained by considering repeated reflection of an emitted outgoing wave within region m , in which the dipole resides. This reflection can be described by the effective reflection coefficients $\tilde{r}_{m1}^{p,s}$ and $\tilde{r}_{mM}^{p,s}$ of regions 1 to m and m to M , respectively. These coefficients are *not* identical to the previously calculated coefficients $r_{m1}^{p,s}$ and $r_{mM}^{p,s}$, since the latter respect *all* regions 1 to M , while $\tilde{r}_{m1}^{p,s}$ and $\tilde{r}_{mM}^{p,s}$ only respect regions 1 to m and m to M , respectively. Also $\tilde{r}_{m1}^{p,s}$ and $\tilde{r}_{mM}^{p,s}$, however, can be calculated with the algorithm given in appendix B.2.

Neglecting any nonradiative decay channels (but not nonradiative power dissipation) an expression for the total dissipated power can be obtained by calculating another geometric sum. The result is given in [13] and can be rewritten using a dimensionless integration variable similar to the result from [23]:

$$\begin{aligned} P_T(\theta) = & \frac{ck_m^4}{2\varepsilon_m^{3/2}} \operatorname{Re} \left[\int_0^\infty dv \frac{v}{\sqrt{1-v^2}} \cdot \right. \\ & \cdot \left(\mu_\perp^2 v^2 \frac{\left[1 + \tilde{r}_{mM}^p \exp(-2ik_m z_m \sqrt{1-v^2}) \right] \left[1 + \tilde{r}_{m1}^p \exp(2ik_m z_{m-1} \sqrt{1-v^2}) \right]}{1 - \tilde{r}_{m1}^p \tilde{r}_{mM}^p \exp[2ik_m(z_{m-1} - z_m)\sqrt{1-v^2}]} + \right. \\ & + \frac{1}{2}\mu_\parallel^2 \frac{\left[1 + \tilde{r}_{mM}^s \exp(-2ik_m z_m \sqrt{1-v^2}) \right] \left[1 + \tilde{r}_{m1}^s \exp(2ik_m z_{m-1} \sqrt{1-v^2}) \right]}{1 - \tilde{r}_{m1}^s \tilde{r}_{mM}^s \exp[2ik_m(z_{m-1} - z_m)\sqrt{1-v^2}]} + \\ & \left. \left. + \frac{1}{2}\mu_\parallel^2(1-v^2) \frac{\left[1 - \tilde{r}_{mM}^p \exp(-2ik_m z_m \sqrt{1-v^2}) \right] \left[1 - \tilde{r}_{m1}^p \exp(2ik_m z_{m-1} \sqrt{1-v^2}) \right]}{1 - \tilde{r}_{m1}^p \tilde{r}_{mM}^p \exp[2ik_m(z_{m-1} - z_m)\sqrt{1-v^2}]} \right) \right] \end{aligned}$$

Here, the abbreviations $\mu_\perp = \mu \cos \theta$ and $\mu_\parallel = \mu \sin \theta$ have been used. Of course, also the reflection coefficients $\tilde{r}_{m1}^{p,s}$ and $\tilde{r}_{mM}^{p,s}$ are dependent on v , which is given by $k_r = vk_m$. The integration over dv has to be done numerically, which can result in high computational costs due to the evaluation of the reflection coefficients for different values of v .

The normalized radiation intensity in regions $j = 1$ and $j = M$ can now be written in the following way [23]:

$$\hat{S}(\mathbf{r}_0, \theta, \varphi) = \frac{c\varepsilon_j^{1/2}}{8\pi} \cdot \frac{|\mathbf{E}(\mathbf{r}_0, \theta, \varphi)|^2}{P_T(\theta)}$$

Typically, the emitting dipoles are oriented in a random fashion, which is accounted for by an averaging of \hat{S} over all possible orientations of the dipole. First, the average over all azimuthal angles can be obtained by

$$\langle \hat{S} \rangle_\varphi(\mathbf{r}_0, \theta) = \frac{1}{2\pi} \int_0^{2\pi} d\varphi \hat{S}(\mathbf{r}_0, \theta, \varphi).$$

Due to the cylindrical symmetry of the problem, $\langle \hat{S} \rangle_\varphi$ does not depend on φ_0 , which permits the simplification

$$\langle \hat{S} \rangle_\varphi(\mathbf{r}_0, \theta) = \frac{\langle \hat{S} \rangle_\varphi^\perp(\mathbf{r}_0)}{1 + \eta \tan^2 \theta} + \frac{\langle \hat{S} \rangle_\varphi^\parallel(\mathbf{r}_0)}{1 + (\eta \tan^2 \theta)^{-1}}$$

from [23], where

$$\langle \hat{S} \rangle_\varphi^\perp(\mathbf{r}_0) = \frac{c\varepsilon_j^{1/2}}{8\pi} \cdot \frac{|\mathbf{E}^z|^2}{P_T^\perp}$$

and

$$\langle \hat{S} \rangle_\varphi^\parallel(\mathbf{r}_0) = \frac{c\varepsilon_j^{1/2}}{16\pi} \cdot \frac{|\mathbf{E}^p|^2 + |\mathbf{E}^s|^2}{P_T^\parallel}$$

as well as the definition $\eta = P_T^\perp/P_T^\parallel$ with $P_T^\perp = P_T(0)$ and $P_T^\parallel = P_T(\frac{\pi}{2})$ has been used. Here, $\langle \hat{S} \rangle_\varphi$ cannot be written by the intuitively simpler form

$$\cos^2 \theta \langle \hat{S} \rangle_\varphi^\perp + \sin^2 \theta \langle \hat{S} \rangle_\varphi^\parallel$$

except for $\eta = 1$ due to the different power normalization for parallel and perpendicular orientation of the dipole [23]. The simplified expression for $\langle \hat{S} \rangle_\varphi$ can then be integrated (numerically) over θ to obtain the averaged normalized intensity $\langle \hat{S} \rangle_\Omega(\mathbf{r}_0)$, which is the starting point for further calculations.

B.4. Application to a three-phase system

For illustration of the theoretical results from the previous sections a computer simulation with Mathematica was performed to analyze a geometry similar to experiments reported in [52]. To this end the PL radiation profile of MoS₂ flakes deposited on the flat surface of a hemispherical SIL made from zirconia (ZrO₂), a material with exceptionally high refractive index, is investigated. In particular it is found that the addition of a thin layer of poly(methyl methacrylate) (PMMA), a typical polymer used for coating, covering the MoS₂ flakes exhibits a rich behavior.

At a PL wavelength of 667 nm literature values for the refractive indices of zirconia and PMMA are $n_{\text{ZrO}_2} = 2.1473$ [67] and $n_{\text{PMMA}} = 1.4878$ [62], respectively. The MoS₂ flake is modeled by a dipole emitter located 1 nm below the zirconia surface. Hence, a PMMA layer of thickness $d > 1$ nm translates to the description of appendix B.1 by setting $n_1 = 2.1473$,

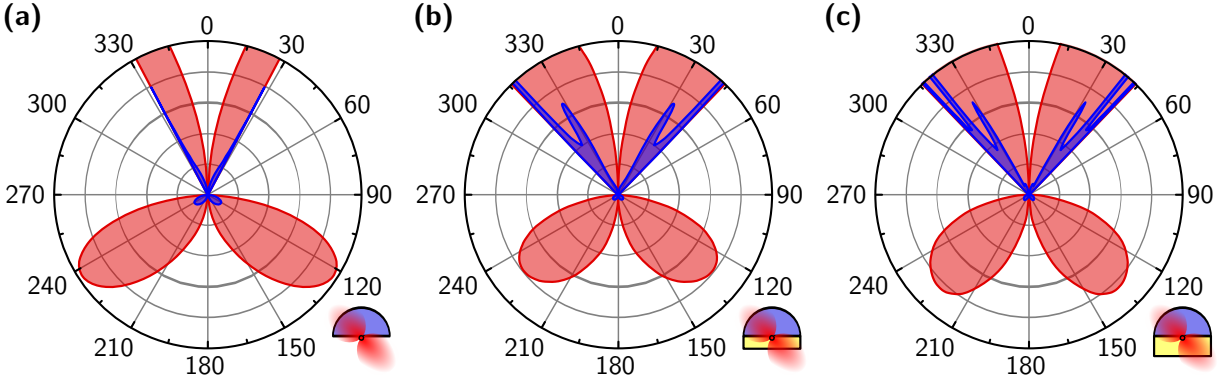


Figure B.4.: Radiation profiles at $\lambda = 667$ nm wavelength of a dipole located 1 nm from the flat surface of a hemispherical zirconia SIL for different thickness d of an additional PMMA layer. Each profile is presented at two different scales to make both small features (red) and the general behavior (blue) visible. **(a)** No PMMA layer, i.e. the dipole resides in air at 1 nm distance from the SIL. Red curve is enlarged by a factor of 20. **(b)** PMMA layer thickness $d = \frac{3}{4}\lambda = 500$ nm. Red curve is enlarged by a factor of 25. **(c)** PMMA layer thickness $d = \frac{5}{4}\lambda = 834$ nm. Red curve is enlarged by a factor of 20.

$n_2 = 1.4878$ and $n_3 = 1$ as well as $z_1 = 1$ nm and $z_2 = z_1 - d$. Of course, for $d < 1$ nm this description needs to be adapted accordingly.

Fig. B.4 shows simulations of radiation profiles given by $\sin \theta \langle \hat{S} \rangle_{\Omega}(\theta_0, r_0)$ for $r_0 = 1$ mm and different values of d . Each profile is presented at two different scales to make both small features (red) and the general behavior (blue) visible. Like in fig. B.1 the z -axis points upward, i.e. emission toward the SIL is depicted in the top half of the figure. The factor $\sin \theta$ is included to account for the volume element in spherical coordinates.

The case $d = 0$ is illustrated in fig. B.4 (a), for which the differing definitions $n_1 = 2.1473$, $n_2 = 1$ and $z_1 = 1$ nm have been used. While emission to the lower half-plane resembles that of a dipole emitter weighted with the factor $\sin \theta$, emission in the upper half-plane occurs predominantly close to the critical angle of the zirconia-air interface that is equal to 27.76° . This general feature has already been found in [23].

Figs. B.4 (b) and B.4 (c) show similar radiation profiles for an additional PMMA layer with thickness $d = \frac{3}{4}\lambda = 500$ nm and $d = \frac{5}{4}\lambda = 834$ nm, respectively. Here, as well, emission to the lower half-plane resembles that of a dipole, while emission to the upper half-plane is concentrated close to the critical angle of 43.86° . However, the radiation profile in upward direction shows a complex structure with several minima and maxima, which is also highly dependent on the thickness of the PMMA layer.

This dependency on the PMMA layer thickness is shown more clearly in fig. B.5, which shows the collection efficiency of objectives with different NAs centered above the zirconia SIL. Fig. B.5 (a) shows the ratio of collected light to total emission of the dipole as function of the PMMA layer thickness for NAs 0.82 and 0.65, which have been used for PL measurements in this work.

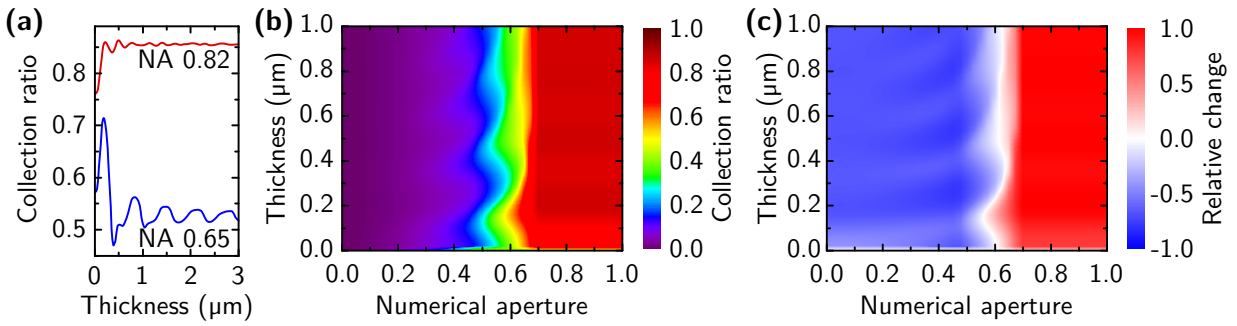


Figure B.5.: Dependence of light collection efficiency of an objective centered above the zirconia SIL on NA and PMMA layer thickness. **(a)** Ratio of collected light to total emitted light as function of PMMA layer thickness for NAs 0.82 and 0.65. **(b)** Ratio of collected light to total emitted light as function of NA and PMMA layer thickness. **(c)** Relative change of light collection ratio as compared to collection ratio for same NA at $d = 0$ as function of NA and PMMA layer thickness.

For both objectives this ratio is equal to 43 % for $d = 0$, since they collect light from an angle that is wider than the critical angle of the zirconia-air interface. A dependence of the collection ratio can thus only be observed for NAs below 0.46, where the critical angle is larger than the light collection angle.

For $d > 0$ a substantial increase of the collection ratio can be observed for both objectives. This is due to total internal reflection at the PMMA-air interface, which suppresses “leakage” of the dipole radiation into the lower half-plane. However, the critical angle of the PMMA-zirconia interface is now larger than the light collection angle of the objective with NA 0.65 but smaller than that of the objective with NA 0.82. This causes a drastic difference in their behavior.

The collection ratio for NA 0.82 is almost independent of the PMMA layer thickness apart from a steep increase below 200 nm, which can be attributed to a change in the total dissipated power of the dipole. This independence is intuitively clear, since the NA 0.82 objective collects all of the light emitted toward the upper half plane and this fraction should not depend strongly on the PMMA layer thickness.

For NA 0.65, however, the complex structure of the radiation profile illustrated in figs. B.4 (b) and B.4 (c) cause a more complicated behavior. The changing number and position of the angular maxima lead to a strong oscillation of the collection ratio upon changing the PMMA layer thickness. The most pronounced maximum occurs at about 180 nm with a ratio of 71 %.

A more general image of this observation is given by fig. B.5 (b), where the collection ratio is plotted as a function of NA and PMMA layer thickness. As expected, strong oscillations are only observed for NAs below 0.69, which corresponds to a light collection angle below the critical angle of the PMMA-zirconia interface. A pronounced maximum of the collection efficiency between 100 nm and 200 nm is present for a broad range of NAs between 0.3 and 0.69.

At the very bottom of fig. B.5 (b) the collection ratio for $d = 0$ is visible, which exhibits an important transition near NA 0.62. For emphasis fig. B.5 (c) shows the *relative* change of the collection efficiency as compared to the collection efficiency for the same NA at $d = 0$. Using this picture the separation into two regimes is apparent.

For small NAs a general reduction of the collection efficiency is observed upon introduction of an additional PMMA layer. This behavior is due to the increased critical angle for the PMMA-zirconia interface as compared to air and zirconia alone. Hence, more light passes by the objective for light collection angles smaller than the critical angle, when introducing an additional PMMA layer.

For larger NAs, however, all light emitted toward the upper half-plane is collected irrespective of the presence or absence of the PMMA layer. In this case the suppression of radiation “leakage” into the lower half-plane by total internal reflection at the PMMA-air interface is responsible for an increased collection efficiency. In the intermediate regime around NA 0.62 each effect can outweigh the other and the collection efficiency may increase or decrease depending on the actual thickness of the PMMA layer.

Due to nested numeric integration all results presented here produced high computational costs. Specifically, the generation of each of the plots from fig. B.5 using a straightforward implementation without sophisticated optimization mechanisms has required several hundred hours of processor time on different 2.83 GHz machines and would not have been possible without caching of intermediate results and massive parallelization on up to 130 CPUs. However, according to reports from the Mathematica community, more intelligent approaches like reformulation of numeric integrals in terms of differential equations are promising for a reduction of computation time.

List of Abbreviations

Term	Description	Page List
2DEG	Two-dimensional electron gas	22
2DHG	Two-dimensional hole gas	22
AFM	Atomic force microscope	10, 31, 32
AZ MiR 701	MicroChemicals AZ® MiR™ 701 positive photoresist	48
CAD	Computer-aided design	24, 25, 27, 28, 30
CCD	Charge-coupled device	16, 18
CVD	Chemical vapor deposition	10
cw	Continuous wave	16, 17
DMSO	Dimethyl sulfoxide	31
FET	Field-effect transistor	7, 8, 22, 33, 44
FETT	Field-effect tunneling transistor	8
FWHM	Full width at half maximum	19
hcp	Hexagonal close-packed	9, 10
HWP	Half-wave plate	16, 17
LOR 3B	MicroChem LOR 3B lift-off resist	27, 29, 30, 47, 48
MIS	Metal-insulator-semiconductor junction	22
MoS ₂	Molybdenum disulfide	7–14, 18–21, 24–28, 30–33, 36–41, 43–45, 49, 70
MOSFET	Metal-oxide-semiconductor field-effect transistor	7
NA	Numerical aperture	16, 17, 51, 71–73
NAIL	Numerical aperture increasing lens	51
PL	Photoluminescence	8, 10, 14, 16–21, 40, 41, 43, 44, 51, 70, 71
PMMA	Poly(methyl methacrylate)	70–73
QWP	Quarter-wave plate	16, 17
S1813	MicroChem (Dow) Microposit® S1813® positive photoresist	27, 47, 48

Term	Description	Page List
SEM	Scanning electron microscope	29, 31, 48
SIL	Solid immersion lens	8, 44, 51, 70–72
SOC	Spin-orbit coupling	12–14
TMDC	Transition metal dichalcogenide	7–9, 14, 18, 21–23
UHV	Ultra high vacuum, usually featuring a pressure between 10^{-7} mbar and 10^{-12} mbar	23, 31, 44

References

- [1] D'ANGELO, P.: *Hugin – Panorama photo stitcher*. URL: <http://hugin.sourceforge.net/>. Retrieved on August 23, 2014 20:52:23 UTC.
- [2] ARFKEN, G. B., WEBER, H. J. and HARRIS, F. E.: *Mathematical Methods for Physicists*. Elsevier Academic Press, Burlington, San Diego, London 2005. Pages 489–493.
- [3] BERKELBACH, T. C., HYBERTSEN, M. S. and REICHMAN, D. R.: *Theory of neutral and charged excitons in monolayer transition metal dichalcogenides*. Phys. Rev. B **88**, 045318 (2013). DOI: 10.1103/PhysRevB.88.045318.
- [4] BETZIG, E., PATTERSON, G. H., SOUGRAT, R. et al.: *Imaging Intracellular Fluorescent Proteins at Nanometer Resolution*. Science **313**, 1642–1645 (2006). DOI: 10.1126/science.1127344.
- [5] BLAKE, P., HILL, E. W., CASTRO NETO, A. H. et al.: *Making graphene visible*. Appl. Phys. Lett. **91**, 063124 (2007). DOI: 10.1063/1.2768624.
- [6] BRENNAN, K. F.: *The Physics of Semiconductors: With Applications to Optoelectronic Devices*. Cambridge University Press, Cambridge 1999.
- [7] BRITNELL, L., GORBACHEV, R. V., JALIL, R. et al.: *Field-Effect Tunneling Transistor Based on Vertical Graphene Heterostructures*. Science **335**, 947–950 (2012). DOI: 10.1126/science.1218461.
- [8] CAO, T., WANG, G., HAN, W. et al.: *Valley-selective circular dichroism of monolayer molybdenum disulphide*. Nat. Commun. **3**, 887 (2012). DOI: 10.1038/ncomms1882.
- [9] CASTRO NETO, A. H., GUINEA, F., PERES, N. M. R. et al.: *The electronic properties of graphene*. Rev. Mod. Phys. **81**, 109–162 (2009). DOI: 10.1103/RevModPhys.81.109.
- [10] CHERNIKOV, A., BERKELBACH, T. C., HILL, H. M. et al.: *Exciton Binding Energy and Nonhydrogenic Rydberg Series in Monolayer WS₂*. Phys. Rev. Lett. **113**, 076802 (2014). DOI: 10.1103/PhysRevLett.113.076802.
- [11] CONLEY, H. J., WANG, B., ZIEGLER, J. I. et al.: *Bandgap Engineering of Strained Monolayer and Bilayer MoS₂*. Nano Lett. **13**, 3626–3630 (2013). DOI: 10.1021/nl4014748.

- [12] ELIAS, D. C., GORBACHEV, R. V., MAYOROV, A. S. et al.: *Dirac cones reshaped by interaction effects in suspended graphene*. Nature Phys. **7**, 701–704 (2011). DOI: 10.1038/nphys2049.
- [13] FORD, G. W. and WEBER, W. H.: *Electromagnetic interactions of molecules with metal surfaces*. Phys. Rep. **113**, 195–287 (1984). DOI: 10.1016/0370-1573(84)90098-X.
- [14] GEIM, A. K. and GRIGORIEVA, I. V.: *Van der Waals heterostructures*. Nature **499**, 419–425 (2013). DOI: 10.1038/nature12385.
- [15] GEORGIOU, T., JALIL, R., BELLE, B. D. et al.: *Vertical field-effect transistor based on graphene-WS₂ heterostructures for flexible and transparent electronics*. Nat. Nanotechnol. **8**, 100–103 (2013). DOI: 10.1038/nnano.2012.224.
- [16] GOLDBERG, B. B., IPPOLITO, S. B., NOVOTNY, L. et al.: *Immersion lens microscopy of photonic nanostructures and quantum dots*. IEEE J. Sel. Top. Quantum Electron. **8**, 1051–1059 (2002). DOI: 10.1109/JSTQE.2002.804232.
- [17] GOLDEN, J., MILLER, H., NAWROCKI, D. et al.: *Optimization of Bi-layer Lift-Off Resist Process*. MicroChem Corp., February 2009. URL: <http://www.microchem.com/pdf/LOR-Extended-Abstract-Final.pdf>.
- [18] HANWELL, M. D., CURTIS, D. E., LONIE, D. C. et al.: *Avogadro: an advanced semantic chemical editor, visualization, and analysis platform*. J. Cheminform. **4**, 17 (2012). DOI: 10.1186/1758-2946-4-17.
- [19] HARRINGTON, B., ENGELEN, J., BAH, T. et al.: *Inkscape. Draw Freely*. URL: <http://www.inkscape.org>. Retrieved on August 23, 2014 20:55:22 UTC.
- [20] HE, K., POOLE, C., MAK, K. F. et al.: *Experimental Demonstration of Continuous Electronic Structure Tuning via Strain in Atomically Thin MoS₂*. Nano Lett. **13**, 2931–2936 (2013). DOI: 10.1021/nl4013166.
- [21] HEINZEL, T.: *Mesoscopic electronics in solid state nanostructures*. Wiley-VCH, Weinheim 2003.
- [22] HELL, S. W. and WICHMANN, J.: *Breaking the diffraction resolution limit by stimulated emission: stimulated-emission-depletion fluorescence microscopy*. Opt. Lett. **19**, 780–782 (1994). DOI: 10.1364/OL.19.000780.
- [23] HELLEN, E. H. and AXELROD, D.: *Fluorescence emission at dielectric and metal-film interfaces*. J. Opt. Soc. Am. B **4**, 337–350 (1987). DOI: 10.1364/JOSAB.4.000337.
- [24] HILLERINGMANN, U.: *Silizium-Halbleitertechnologie*. Teubner, Stuttgart 2002. 3rd edition.
- [25] HÖGELE, A., SEIDL, S., KRONER, M. et al.: *Fiber-based confocal microscope for cryogenic spectroscopy*. Rev. Sci. Instrum. **79**, 023709 (2008). DOI: 10.1063/1.2885681.

- [26] HUARD, V., COX, R. T., SAMINADAYAR, K. et al.: *Bound States in Optical Absorption of Semiconductor Quantum Wells Containing a Two-Dimensional Electron Gas*. Phys. Rev. Lett. **84**, 187–190 (2000). DOI: 10.1103/PhysRevLett.84.187.
- [27] ISHIGAMI, M., CHEN, J. H., CULLEN, W. G. et al.: *Atomic Structure of Graphene on SiO₂*. Nano Lett. **7**, 1643–1648 (2007). DOI: 10.1021/nl070613a.
- [28] JERIČ, A.: *LPKF ProtoLaser LDI. A106-A1-01M User manual*. LPKF Laser & Elektronika, September 2013.
- [29] JONES, A. M., YU, H., GHIMIRE, N. J. et al.: *Optical generation of excitonic valley coherence in monolayer WSe₂*. Nat. Nanotechnol. **8**, 634–638 (2013). DOI: 10.1038/nnano.2013.151.
- [30] KLAR, T. A. and HELL, S. W.: *Subdiffraction resolution in far-field fluorescence microscopy*. Opt. Lett. **24**, 954–956 (1999). DOI: 10.1364/OL.24.000954.
- [31] KORN, T., HEYDRICH, S., HIRMER, M. et al.: *Low-temperature photocarrier dynamics in monolayer MoS₂*. Appl. Phys. Lett. **99**, 102109 (2011). DOI: 10.1063/1.3636402.
- [32] LIDE, D. R. (Ed.): *CRC Handbook of Chemistry and Physics*. CRC Press, Boca Raton 2001. 82nd edition. URL: <http://www.crcpress.com/product/isbn/9780849304828>.
- [33] LIN, Y., VALDES-GARCIA, A., HAN, S. et al.: *Wafer-Scale Graphene Integrated Circuit*. Science **332**, 1294–1297 (2011). DOI: 10.1126/science.1204428.
- [34] LIU, Z., GOLDBERG, B. B., IPPOLITO, S. B. et al.: *High resolution, high collection efficiency in numerical aperture increasing lens microscopy of individual quantum dots*. Appl. Phys. Lett. **87**, 071905 (2005). DOI: 10.1063/1.2012532.
- [35] LUAN, L., SIEVERT, P. R., WATKINS, B. et al.: *Angular radiation pattern of electric dipoles embedded in a thin film in the vicinity of a dielectric half space*. Appl. Phys. Lett. **89**, 031119 (2006). DOI: 10.1063/1.2234299.
- [36] MADOU, M. J.: *Fundamentals of Microfabrication*. CRC Press, 1996.
- [37] MAK, K. F., HE, K., LEE, C. et al.: *Tightly bound trions in monolayer MoS₂*. Nat. Mater. **12**, 207–211 (2013). DOI: 10.1038/nmat3505.
- [38] MAK, K. F., HE, K., SHAN, J. et al.: *Control of valley polarization in monolayer MoS₂ by optical helicity*. Nat. Nanotechnol. **7**, 494–498 (2012). DOI: 10.1038/nnano.2012.96.
- [39] MAK, K. F., JU, L., WANG, F. et al.: *Optical spectroscopy of graphene: From the far infrared to the ultraviolet*. Solid State Commun. **152**, 1341–1349 (2012). DOI: 10.1016/j.ssc.2012.04.064.

- [40] MICROCHEMICALS GMBH: *AZ® MiR™ 701 Photoresist*. 2001. URL: <http://www.microchemicals.com/micro/mir7011.pdf>. Retrieved on October 21, 2014 14:30:19 UTC.
- [41] MOERNER, W. E. and KADOR, L.: *Optical detection and spectroscopy of single molecules in a solid*. Phys. Rev. Lett. **62**, 2535–2538 (1989). DOI: 10.1103/PhysRevLett.62.2535.
- [42] NAJMAEI, S., LIU, Z., ZHOU, W. et al.: *Vapour phase growth and grain boundary structure of molybdenum disulphide atomic layers*. Nat. Mater. **12**, 754–759 (2013). DOI: 10.1038/nmat3673.
- [43] NEWPORT CORP.: *Broadband Beam Samplers*. In *The Newport Resource*, p. 738. 2011. URL: <http://www.nxtbook.com/nxtbooks/newportcorp/resource2011/#/768>. Retrieved on September 30, 2014 10:09:04 UTC.
- [44] NIEDRIG, H. (Ed.): *Optik: Wellen- und Teilchenoptik*, vol. 3 in *Bergmann Schaefer: Lehrbuch der Experimentalphysik*. De Gruyter, Berlin 2004. 10th edition.
- [45] NOVOSELOV, K. S., FAL'KO, V. I., COLOMBO, L. et al.: *A roadmap for graphene*. Nature **490**, 192–200 (2012). DOI: 10.1038/nature11458.
- [46] NOVOSELOV, K. S., GEIM, A. K., MOROZOV, S. V. et al.: *Electric Field Effect in Atomically Thin Carbon Films*. Science **306**, 666–669 (2004). DOI: 10.1126/science.1102896.
- [47] PAWLEY, J.: *Handbook of Biological Confocal Microscopy*. Springer Science & Business Media, New York 2006. 3rd edition.
- [48] PREIBISCH, S., SAALFELD, S. and TOMANCAK, P.: *Globally optimal stitching of tiled 3D microscopic image acquisitions*. Bioinformatics **25**, 1463–1465 (2009). DOI: 10.1093/bioinformatics/btp184.
- [49] RADISAVLJEVIC, B., RADENOVIC, A., BRIVIO, J. et al.: *Single-layer MoS₂ transistors*. Nat. Nanotechnol. **6**, 147–150 (2011). DOI: 10.1038/nnano.2010.279.
- [50] RAI-CHOUDHURY, P.: *Handbook of Microlithography, Micromachining and Micro-fabrication*. SPIE Press, Bellingham 1997.
- [51] RAYLEIGH, F. R. S.: *XXXI. Investigations in optics, with special reference to the spectroscope*. Philos. Mag. Series 5 **8**, 261–274 (1879). DOI: 10.1080/14786447908639684.
- [52] RIEDEL, D., ROHNER, D., GANZHORN, M. et al.: *A low-loss, broadband antenna for efficient photon collection from a coherent spin in diamond*. arXiv:1408.4117 [cond-mat, physics:physics] (2014). URL: <http://arxiv.org/abs/1408.4117>.
- [53] RYCKERZ, A., TWORZYDŁO, J. and BEENAKKER, C. W. J.: *Valley filter and valley valve in graphene*. Nature Phys. **3**, 172–175 (2007). DOI: 10.1038/nphys547.

- [54] SALEHZADEH, O., TRAN, N. H., LIU, X. et al.: *Exciton Kinetics, Quantum Efficiency, and Efficiency Droop of Monolayer MoS₂ Light-Emitting Devices*. Nano Lett. **14**, 4125–4130 (2014). DOI: 10.1021/nl5017283.
- [55] SALLEN, G., BOUET, L., MARIE, X. et al.: *Robust optical emission polarization in MoS₂ monolayers through selective valley excitation*. Phys. Rev. B **86**, 081301 (2012). DOI: 10.1103/PhysRevB.86.081301.
- [56] SCHINDELIN, J., RUEDEN, C., TINEVEZ, J. et al.: *Fiji Is Just ImageJ*. URL: <http://fiji.sc/Fiji>. Retrieved on August 23, 2014 20:57:34 UTC.
- [57] SCHOTTKY, W.: *Halbleitertheorie der Sperrschiicht*. Naturwissenschaften **26**, 843–843 (1938). DOI: 10.1007/BF01774216.
- [58] SCHOTTKY, W.: *Zur Halbleitertheorie der Sperrschiicht- und Spitzengleichrichter*. Z. Physik **113**, 367–414 (1939). DOI: 10.1007/BF01340116.
- [59] SHIPLEY COMPANY, LLC: *Microposit® S1800® Series Photo Resists*. URL: http://www.microchem.com/PDFs_Dow/S1800.pdf. Retrieved on August 27, 2014 9:51:45 UTC.
- [60] SPLENDIANI, A., SUN, L., ZHANG, Y. et al.: *Emerging Photoluminescence in Monolayer MoS₂*. Nano Lett. **10**, 1271–1275 (2010). DOI: 10.1021/nl903868w.
- [61] STÉBÉ, B. and AINANE, A.: *Ground state energy and optical absorption of excitonic trions in two dimensional semiconductors*. Superlattices Microstruct. **5**, 545–548 (1989). DOI: 10.1016/0749-6036(89)90382-0.
- [62] SULTANOVA, N., KASAROVA, S. and NIKOLOV, I.: *Dispersion Properties of Optical Polymers*. Acta. Phys. Pol. A **116**, 585–587 (2009). URL: <http://przyrbwn.icm.edu.pl/APP/ABSTR/116/a116-4-42.html>.
- [63] TANIGUCHI, K., MATSUMOTO, A., SHIMOTANI, H. et al.: *Electric-field-induced superconductivity at 9.4 K in a layered transition metal disulphide MoS₂*. Appl. Phys. Lett. **101**, 042603 (2012). DOI: 10.1063/1.4740268.
- [64] THILAGAM, A.: *Two-dimensional charged-exciton complexes*. Phys. Rev. B **55**, 7804–7808 (1997). DOI: 10.1103/PhysRevB.55.7804.
- [65] VARSHNI, Y. P.: *Temperature dependence of the energy gap in semiconductors*. Physica **34**, 149–154 (1967). DOI: 10.1016/0031-8914(67)90062-6.
- [66] WANG, Q. H., KALANTAR-ZADEH, K., KIS, A. et al.: *Electronics and optoelectronics of two-dimensional transition metal dichalcogenides*. Nat. Nanotechnol. **7**, 699–712 (2012). DOI: 10.1038/nnano.2012.193.
- [67] WOOD, D. L. and NASSAU, K.: *Refractive index of cubic zirconia stabilized with yttria*. Appl. Opt. **21**, 2978–2981 (1982). DOI: 10.1364/AO.21.002978.

- [68] WU, Y., JENKINS, K. A., VALDES-GARCIA, A. et al.: *State-of-the-Art Graphene High-Frequency Electronics*. Nano Lett. **12**, 3062–3067 (2012). DOI: 10.1021/nl300904k.
- [69] WU, Y., LIN, Y.-m., BOL, A. A. et al.: *High-frequency, scaled graphene transistors on diamond-like carbon*. Nature **472**, 74–78 (2011). DOI: 10.1038/nature09979.
- [70] XIA, F., FARMER, D. B., LIN, Y.-m. et al.: *Graphene Field-Effect Transistors with High On/Off Current Ratio and Large Transport Band Gap at Room Temperature*. Nano Lett. **10**, 715–718 (2010). DOI: 10.1021/nl9039636.
- [71] XIAO, D., LIU, G., FENG, W. et al.: *Coupled Spin and Valley Physics in Monolayers of MoS and Other Group-VI Dichalcogenides*. Phys. Rev. Lett. **108**, 196802 (2012). DOI: 10.1103/PhysRevLett.108.196802.
- [72] XIAO, D., YAO, W. and NIU, Q.: *Valley-Contrasting Physics in Graphene: Magnetic Moment and Topological Transport*. Phys. Rev. Lett. **99**, 236809 (2007). DOI: 10.1103/PhysRevLett.99.236809.
- [73] XU, M., LIANG, T., SHI, M. et al.: *Graphene-Like Two-Dimensional Materials*. Chem. Rev. **113**, 3766–3798 (2013). DOI: 10.1021/cr300263a.
- [74] YAO, W., XIAO, D. and NIU, Q.: *Valley-dependent optoelectronics from inversion symmetry breaking*. Phys. Rev. B **77**, 235406 (2008). DOI: 10.1103/PhysRevB.77.235406.
- [75] YE, J. T., ZHANG, Y. J., AKASHI, R. et al.: *Superconducting Dome in a Gate-Tuned Band Insulator*. Science **338**, 1193–1196 (2012). DOI: 10.1126/science.1228006.
- [76] YUN, W. S., HAN, S. W., HONG, S. C. et al.: *Thickness and strain effects on electronic structures of transition metal dichalcogenides: 2H-MX₂ semiconductors (M = Mo, W; X = S, Se, Te)*. Phys. Rev. B **85**, 033305 (2012). DOI: 10.1103/PhysRevB.85.033305.
- [77] ZENG, H., DAI, J., YAO, W. et al.: *Valley polarization in MoS₂ monolayers by optical pumping*. Nat. Nanotechnol. **7**, 490–493 (2012). DOI: 10.1038/nnano.2012.95.
- [78] ZHU, C. R., WANG, G., LIU, B. L. et al.: *Strain tuning of optical emission energy and polarization in monolayer and bilayer MoS₂*. Phys. Rev. B **88**, 121301 (2013). DOI: 10.1103/PhysRevB.88.121301.
- [79] ZINTH, W. and ZINTH, U.: *Optik: Lichtstrahlen – Wellen – Photonen*. Oldenbourg, München 2009. 2nd edition.

Danksagung

Abschließend möchte ich all denen danken, die zu einem erfolgreichen Gelingen dieser Arbeit beigetragen und mich auf diesem Weg begleitet haben.

Zunächst geht mein Dank an Prof. Alexander Högele, der mir das Arbeiten in seiner Forschungsgruppe und die Anfertigung meiner Masterarbeit ermöglicht hat. Ich habe die familiäre Atmosphäre sowie den unkomplizierten Umgang miteinander sehr genossen und daraus immer wieder neue Motivation auch in anstrengenden Phasen gezogen. Auch für fachliche Fragen fand man stets offene Ohren und konnte sich auf konstruktive Diskussionen und Lösungsvorschläge verlassen.

Prof. Jörg Kotthaus danke ich für den Aufbau eines Lehrstuhls, an dem das Forschen viel Freude bereitet und an dem fachliches Know-how sowie das freundschaftliche Arbeitsklima einmalig sind. Weiterhin danke ich Dr. Heribert Lorenz für die Organisation am Lehrstuhl, für Hilfe bei organisatorischen Fragen aller Art und natürlich für den Drucker.

Besonderer Dank gebührt meinem Betreuer Andre Neumann, der sich viel Zeit genommen hat, mir die experimentelle Umsetzung der konfokalen Mikroskopie zu erklären und mir Antworten auf meine zahlreichen Fragen zu geben. Ich habe während des letzten Jahres sehr viel von Dir gelernt und konnte mit allen Problemen und Unklarheiten zu Dir kommen. Vielen Dank auch dafür, dass Du zum Ende meiner Arbeit die Zeit gefunden hast, diese gründlich zu lesen und konstruktiv zu kritisieren. Большое спасибо!

Ebenso möchte ich mich bei allen weiteren Mitgliedern des Lehrstuhls bedanken, die mir bei meinem Projekt geholfen haben. Dies gilt ganz besonders für Philipp Altpeter, der mir viel von seinem umfangreichen Wissen über Prozesstechniken im Reinraum vermittelt hat und ohne den meine Arbeit undenkbar gewesen wäre. Danke, dass Du dir so oft die Zeit genommen hast, mir Fragen zu beantworten und Verfahren zu erklären.

Dies gilt weiter für Matthias Hauck, der mir geholfen hat, meine Probe optisch zu untersuchen und mir dabei die Gewichtsverlagerung im Rumba-Grundschritt auf dem „und“ des ersten Schlages näher zu bringen. Danke auch dafür, dass du mich immer mit einem Scherz aufgeheizt und dich um Computerprobleme, dumme Fragen aller Art und natürlich um die Heliumversorgung gekümmert hast.

Thanks also go to Sarah Wittig who was a great help while building the new microscope head. I really appreciated your expertise in all optics-related topics and your input during adjustment of the setup. It is a pity that you decided to leave Munich and I really hope you are happy at your new position and enjoy your time in the Netherlands.

Außerdem danken möchte ich Florian Forster und Sergey Platonov für ihre Hilfe mit den Transportmessungen zur Charakterisierung der elektrischen Eigenschaften meiner Probe und den zur Verfügung gestellten Platz in ihrem Labor.

Darüber hinaus geht Dank an die Doktoranden Matthias Hofmann, Jessica Lindlau, Jonathan Noé, Jens Repp und Enrico Schubert sowie die Mitarbeiter des Lehrstuhls Anton Heindl, Reinhold Rath und Stephan Manus für bereitwillige Beratung und Unterstützung bei Fragen und Problemen. Danke auch unsrer Sekretärin Martina Jüttner für ihre offene und freundliche Art und unkomplizierter Hilfe bei organisatorischen Dingen.

Das Diplmandenzimmer, das auch nach der Abschaffung des Diploms beharrlich an seinem Namen festhält, ist aus meiner Zeit am Lehrstuhl nicht wegzudenken. Für die hervorragende Stimmung, die sich kaum besser als mit „was sich liebt, das neckt sich“ beschreiben lässt, danke ich meinen Mitstreitern Max Mühlbacher, Bernd Waschneck, Alexander Kneer, Sebastian Müller, speziell Katja Puschkarsky für gemeinsame Gespräche und Kaffeepausen sowie Lorenz Mayr für Diskussionen über allerlei kurioses und zu guter Letzt Jodok Hapacher. Selbstverständlich auch danken möchte ich unsrem unfreiwilligen Gast Alexandra Fink, die im Laufe des Studiums zu einer hervorragenden Freundin geworden ist.

Special thanks go to Hisato Yamaguchi from LANL as well as to his colleagues Sina Najmaei, Sidong Lei, Prof. Pulickel M. Ajayan and Prof. Jun Lou from Rice University for preparation of the MoS₂ samples, without which this work would not have been possible.

Zuletzt und ganz besonders möchte ich mich bei den Leuten in meinem Umfeld bedanken, ohne die ich dieses Studium nicht geschafft hätte. Das gilt zum einen für meinen Freundeskreis, der immer für mich da war und mir auch in anstrengenden Zeiten immer Rückhalt gegeben hat, und alle anderen, die dazu beigetragen haben, dass ich mich immer mit Freude an meine Studienzeit erinnern werde. Zum anderen möchte ich mich für die große Unterstützung durch meine Familie und insbesondere meine Eltern bedanken, die mir dieses Studium ermöglicht und in allen Lebenslagen zu mir gehalten haben.

Selbstständigkeitserklärung

Hiermit erkläre ich, die vorliegende Arbeit selbstständig verfasst zu haben und keine anderen als die in der Arbeit angegebenen Quellen und Hilfsmittel benutzt zu haben.

....., den

Ort

Datum

.....

Unterschrift